
Topological transport properties of ferromagnetic and antiferromagnetic materials

Zur Erlangung des Grades eines Doktors der Naturwissenschaften (Dr. rer. nat.)
Genehmigte Dissertation von Ilias Samathrakis aus Thessaloniki, Griechenland
Tag der Einreichung: 29. Juli 2022, Tag der Prüfung: 04. November 2022

1. Gutachten: Prof. Hongbin Zhang
 2. Gutachten: Prof. Yuriy Mokrousov
- Darmstadt, Technische Universität Darmstadt



TECHNISCHE
UNIVERSITÄT
DARMSTADT

Materials and Earth
Sciences Department
Institute of Materials
Science
Theory of Magnetic
Materials

Topological transport properties of ferromagnetic and antiferromagnetic materials

Accepted doctoral thesis by Ilias Samathrakis

Date of submission: 29. Juli 2022

Date of thesis defense: 04. November 2022

Darmstadt, Technische Universität Darmstadt

Bitte zitieren Sie dieses Dokument als:

URN: urn:nbn:de:tuda-tuprints-229142

URL: <https://tuprints.ulb.tu-darmstadt.de/22914>

Jahr der Veröffentlichung auf TUprints: 2022

Dieses Dokument wird bereitgestellt von tuprints,

E-Publishing-Service der TU Darmstadt

<https://tuprints.ulb.tu-darmstadt.de>

tuprints@ulb.tu-darmstadt.de

Die Veröffentlichung steht unter folgender Creative Commons Lizenz:

Namensnennung – Weitergabe unter gleichen Bedingungen 4.0 International

<https://creativecommons.org/licenses/by-sa/4.0/>

This work is licensed under a Creative Commons License:

Attribution–ShareAlike 4.0 International

<https://creativecommons.org/licenses/by-sa/4.0/>

*"I think nature's imagination is so much greater than man's, she's
never going to let us relax"*
- Richard Feynman

Erklärungen laut Promotionsordnung

§ 8 Abs. 1 lit. c PromO

Ich versichere hiermit, dass die elektronische Version meiner Dissertation mit der schriftlichen Version übereinstimmt.

§ 8 Abs. 1 lit. d PromO

Ich versichere hiermit, dass zu einem vorherigen Zeitpunkt noch keine Promotion versucht wurde. In diesem Fall sind nähere Angaben über Zeitpunkt, Hochschule, Dissertationsthema und Ergebnis dieses Versuchs mitzuteilen.

§ 9 Abs. 1 PromO

Ich versichere hiermit, dass die vorliegende Dissertation selbstständig und nur unter Verwendung der angegebenen Quellen verfasst wurde.

§ 9 Abs. 2 PromO

Die Arbeit hat bisher noch nicht zu Prüfungszwecken gedient.

Darmstadt, 29. Juli 2022

I. Samathrakis

Contents

Acknowledgments	ix
Abstract	xi
Zusammenfassung	1
1. Introduction	3
2. Density Functional Theory	7
2.1. Many-body problem	7
2.2. Hartree approximation	8
2.3. Hartree-Fock approximation	9
2.4. Density functional theory	11
2.4.1. Hohenberg-Kohn theorems	11
2.4.2. Kohn-Sham ansatz	13
2.4.3. Kohn-Sham equations	15
2.4.4. Exchange-correlation functionals	16
2.5. Spin-polarized density functional theory	21
2.6. Relativistic effects	23
2.7. Limitations of DFT	27
3. Topological properties	29
3.1. Adiabatic evolution	29
3.2. Berry phase	32
3.3. Berry curvature	34
3.4. Bloch's theorem	36
3.5. Wannier functions	38
3.6. Weyl points and nodal lines	40
3.6.1. Topological protection	43
3.6.2. Types of Weyl nodes	45
3.6.3. Connection to Berry curvature	46

3.6.4. Chern number	46
3.7. Charge and spin currents	47
3.8. Anomalous Hall effect	49
3.9. Anomalous Nernst effect	51
3.10. Computational techniques	52
3.11. Symmetry analysis	55
3.12. Materials	58
3.13. Applications	60
4. Topological properties of non-collinear antiferromagnets	63
4.1. Magnetic configurations	64
4.2. Symmetry analysis	65
4.3. Magnetization induced anomalous Hall/Nernst conductivities	67
4.4. Strain induced anomalous Hall conductivities	69
4.5. Origin of anomalous Hall conductivity	70
5. Topological properties of ferromagnets	75
5.1. Workflow	75
5.2. Notable anomalous Hall/Nernst values	77
5.3. Symmetry analysis	80
5.4. Origin of anomalous Hall/Nernst conductivities	84
5.5. Magnetization induced anomalous Hall/Nernst conductivities	92
5.6. Tunable anomalous Hall/Nernst conductivities	95
5.6.1. Strain induced anomalous Hall conductivity	95
5.6.2. Doping induced anomalous Hall/Nernst conductivities	95
6. Conclusion and Outlook	99
Appendices	101
A. Numerical details	103
B. High throughput results	105

Acknowledgments

First of all, I would like to thank Prof. Hongbin Zhang for accepting me in his group and supervising me throughout my PhD studies. I am grateful for his ambition and his attitude that guided me, encouraged me and made me improve my scientific skills.

Special thanks to Prof. Yuriy Mokrousov for his willingness to serve as a Co-Referee and to provide valuable comments and corrections to the present dissertation. Also to Prof. Wolfgang Donner and Prof. Markus Meinert for their willingness to serve as examination members in my committee.

I would like to thank the administrator of our group, Mrs Maria Walker, for the fast and accurate implementation of everyday life matters.

I would like to thank my colleagues: Marie Joëlle Charrier, Harish Kumar Singh, Chen Shen, Dr. Qiang Gao, Dr. Teng Long, Nuno Miguel dos Santos Fortunato, Dr. Ruiwen Xie, Hamid Nouri, Dr. Tingting Lin, Dr. Xinru Li, Niloofar Hadaeghi, Yixuan Zhang, Mian Dai for their continuous support, our meaningful scientific discussions and collaboration.

The author acknowledges the “Deutsche Physikalische Gesellschaft e. V” (DPG) for the financial support through the priority programme SPP1666 and the “Hochschulrechenzentrum” (HRZ) for the granted computational time, without which the scientific goals of the current dissertation would not have been implemented.

Last but not least, I would like to sincerely thank my parents, my grandfather, my aunts and uncles, my cousins and my dear friends Eleonora Nyström Gialama, Dimitra Skoulidou, Anastasia Terzidou, Erisa Sherbi, Andria Georgiou, Marsi Kiriazi, Eleni Stamboultzi, Sofia Wallgren, Maria Zafeiriadou, Emma Minarelli, Meng Liu, Marialena Kadoglou, Nathalie Piraban, Eleni Zimianiti, Reena Sen, Tasos Leontiou, Thanos Karagevrekis, Nikos Papaevanggelou, Sarantis Stamboultzis, Sakis Fafkas, Evangelos Gryllakis, Evangelos Tzifas, Evangelos Eklemes, Christos Gannakidis, Petros Zimianitis, Patrick van Dieten, Francisco Fabian Gonzalez, Konstantinos Manolis, Andreas Juleshaug, Muhammad Sufyan Ramzan, Matteo Gemignani for the countless memorable experiences we shared and their continuous support, especially during the difficult pandemic period, that motivated me to achieve my scientific goals.

Abstract

Magnetic materials are of fundamental importance to the welfare of our society since they find use, among others, in energy harvesting applications. The rapid technological development requires the generation of new environment friendly methods to power up novel devices, therefore, thermoelectric materials become vital for future applications. A particular class of magnetic materials that can be used in thermoelectric devices is those with nontrivial band topology, such as Weyl and nodal line semimetals, that have recently attracted intensive attention due to their interesting properties.

The anomalous Hall (Nernst) effect, being the generation of a transverse spin polarized charge current as a response to a longitudinal charge current (thermal gradient), was initially associated to ferromagnets. Recently however, it was demonstrated that collinear and non-collinear antiferromagnets can induce finite values, making them interesting for novel applications. These findings though, not only challenged the current understanding of the theoretical background but also the conditions of their existence, being till nowadays pending problems.

In this work, a computational framework to construct maximally localized Wannier functions in an automatic way is provided and subsequently used to calculate the anomalous Hall and Nernst conductivities of ferromagnetic and non-collinear antiferromagnetic intermetallic compounds, with a high success rate of 92%. Detailed symmetry analysis is performed in order to reveal the vanishing anomalous Hall and Nernst conditions in certain ferromagnetic and antiferromagnetic compounds. It is demonstrated that the large values of anomalous Hall and Nernst conductivities are due to the presence of Weyl nodes, nodal lines and small gap areas and that they can further be tuned by means of external stimuli, leading to further enhancement of the anomalous Hall and Nernst conductivities.

In the future, the automated Wannier function workflow can be used to construct the maximally localized Wannier functions of any 3d transition-metal based system, with or without the inclusion of spin-orbit interaction with minimum human intervention and external stimuli can be used to further enhance the topological transport properties of a compound.

Zusammenfassung

Magnetische Materialien sind wichtige Pfeiler für den Wohlstand unserer Gesellschaft, da sie unter anderem Anwendung in der Energiegewinnung finden. Schneller technologischer Fortschritt wird begünstigt durch die Entwicklung neuer umweltfreundlicher Methoden zum Betrieb neuartiger Bauteile. Thermoelektrische Materialien sind so gesehen unersetzlich für die Anwendungen der Zukunft. Eine bestimmte Klasse magnetischer Materialien, welche in thermoelektrischen Komponenten verwendet werden kann, zeichnet sich durch komplexe Bandstrukturen aus: Weyl- und Knotenlinien-Halbmatalle, welche aufgrund ihrer interessanten Eigenschaften große Aufmerksamkeit erregt haben.

Der anomale Hall (Nernst) Effekt, sprich die Erzeugung eines transversal spin-polarisierten Ladungsflusses als Reaktion auf einen longitudinalen Ladungsfluss (thermischer Gradient), wurde ursprünglich mit Ferromagneten in Verbindung gebracht. Kürzlich konnte jedoch gezeigt werden, dass kollineare und nichtkollineare Antiferromagneten endliche Werte induzieren können, was eine Perspektive für neue Anwendungen eröffnet. Jedoch hinterfragen diese Ergebnisse nicht nur gegenwärtige Theorie, sondern auch die Existenzbedingungen des anomalen Hall/Nernst Effekts, und stellen damit bis heute ungelöste Probleme dar.

In der vorliegenden Dissertation wird ein numerisches Gerüst zur automatisierten Konstruktion maximal lokalisierter Wannier-Funktionen geliefert und mit einer Erfolgsquote von 92% auf die Berechnung der anomalen Hall- und Nernst-Leitfähigkeiten ferromagnetischer und nichtkollinearer antiferromagnetischer, intermetallischer Verbindungen angewandt. Eine detaillierte Analyse der Symmetrie wird genutzt, um das Verschwinden anomaler Hall- und Nernst-Zustände in bestimmten ferro- und antiferromagnetischen Verbindungen aufzuzeigen. Es wird gezeigt, dass große anomale Hall- und Nernst-Leitfähigkeiten aufgrund von Weyl-Knoten, Knotenlinien und kleinen Bandbereichen auftreten und dass diese darüber hinaus extern gesteuert werden können, um die anomalen Hall- und Nernst-Leitfähigkeiten noch zu verstärken.

Zukünftig kann die automatisierte Routine zur Erzeugung maximal lokalisierter Wannier-Funktionen auf jedes System angewandt werden, welches auf einem 3d Übergangsmetall basiert, unter optionalem Einbezug der Spin-Bahn-Wechselwirkung, minimaler Nutzerinteraktion und dem Einsatz möglicher externer Steuerung zur Verstärkung der strukturellen



Transporteigenschaften einer Verbindung.

1. Introduction

Topology is the branch of mathematics that describes the properties of geometric objects that are preserved under continuous (smooth) deformations. In general two objects have identical topological properties if there exists a continuous deformation from the one to the other called homotopy. Taking as an example the geometrical objects of Fig. 1.1, we note that the key ingredient of topological characterization is the number of “holes” existing in each object. For this reason, the sphere and the muffin (part (a) and (b), with zero “holes”) belong to the $g = 0$ topological equivalence class, having the same topological properties, whereas the coffee mug and the doughnut (part (c) and (d), with one “hole”), belong to the $g = 1$ topological class.

From the historical point of view, the topological field started in early 70s when Thouless and Kosterlitz, working on a 2D Ising model [94, 95], found a new type of phase transition, in which the topological defects played an important role, the so called BKT transition. The existing, at that time, knowledge signified that all ordered phases could be understood as low temperature “symmetry-breaking” of high temperature disordered phases, according to the theory of Grinzburg-Landau (GL) [44]. The basis of the successful GL theory was the presence of a local order parameter that determined the phases of the system and the transitions among them. However, the new finding posed new challenges to the theory since it evaded the traditional GL theory due to the fact that there was no spontaneous symmetry breaking. A decade later, the discoveries of integer and fractional quantum Hall effects [88, 208] verified phases of matter that cannot be identified by symmetry breaking patterns. It was later that integer and fractional quantum Hall effects were described by a topological invariant known as Chern number (or Thouless-Kohmoto-Nightingale-Nijs number) [205], which is a global parameter that depends on the topological structure of the enclosing manifold. The key concept lies in the Berry phase that describes a geometric phase acquired by the electron wavefunction when adiabatically evolving in parameter space. Since then, many topological phases and states, either with or without time reversal symmetry have been discovered including quantum spin Hall states [83], quantum anomalous Hall states [58], topological insulators [42, 132], topological crystalline insulators [41], topological Kondo insulators [32], topological semimetals [218], high order topological states [10, 192, 179] and Skyrmions [134] among others. A timeline with the most

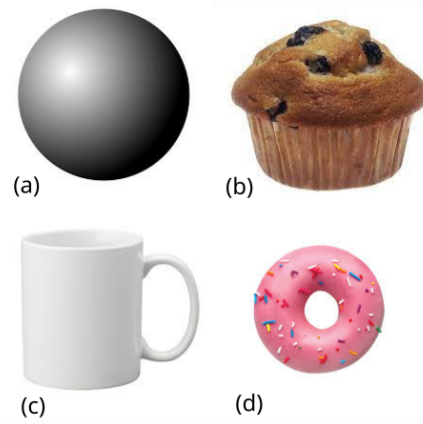


Figure 1.1.: Topology of objects (a) Sphere (b) Muffin (c) Coffee mug (d) Doughnut

important breakthroughs of the field of topological materials is illustrated in Fig. 1.2.

Focusing on semimetals, it is known that a small density of states around the Fermi energy is expected. This special feature is associated to the presence of band touching nodes, the dimensionality of the touching surface of which and its degeneracy determine the type of the semimetal. Specifically, for non degenerate points touching (0D of touching surface) Weyl semimetals emerge while for degenerate band touching Dirac semimetals. Additionally, for touching nodes forming lines or closed loops (1D touching surface) nodal line semimetals emerge. By breaking time reversal symmetry, we further restrict ourselves to magnetic topological materials, in which we observe that the touching nodes act as sources or sinks of Berry curvature. In a current carrying conductor, the Berry curvature acts as an internal fictitious magnetic field that generates a transverse current, the so-called anomalous Hall effect [136]. Replacing the initial longitudinal charge current with a thermal gradient results in the thermal counterpart of the anomalous Hall effect, the anomalous Nernst effect. Even though the anomalous Hall and Nernst effects were initially associated with ferromagnetic materials, further research proved that non collinear antiferromagnets [27] can also induce anomalous Hall/Nernst currents under certain symmetry conditions [180, 198] and recently the collinear antiferromagnet RuO_2 was suggested to exhibit non vanishing values [36].

Climate change combined with the increasing needs to power devices make the development of methods using renewable sources of energy imperative. The idea of converting waste heat to useful electric current is called thermoelectric conversion. Thermoelectric generators are nowadays the key ingredient for versatile energy harvesting being used

to power Internet of Thing (IoT) devices [45, 62] and manufacture wearable devices as well as heat flow sensors, being used in thermal management applications [121, 246]. Conventional devices make use of the Seebeck effect for the thermoelectric generation, however materials with high anomalous Hall/Nernst conductivities can be promising compounds for novel thermoelectric applications since the transverse geometry of the underlying effects has some advantages compared to the conventional longitudinal [247, 131]. The goal of the current dissertation is to implement an automated Wannier function construction workflow in order to compute the anomalous Hall and Nernst conductivities in ferromagnetic and non-collinear antiferromagnetic transition-metal based compounds with the inclusion of spin orbit coupling and investigate their origin and their tunability under external stimuli such as doping, biaxial strain and magnetization direction changes.

The present dissertation is organized as follows. In Chapter 2 a brief overview of the Density functional theory is given followed by a brief discussion of different approximations used such as the local density approximation and the generalized gradient approximation. Additionally, some existing exchange correlation functionals are briefly summarized. Subsequently, in Chapter 3 the notions of Berry phase, Berry connection and Berry curvature are introduced and the rest of the chapter is dedicated to the anomalous Hall and Nernst effects alongside some basic symmetry rules that govern their existence. Next, in Chapter 4 and Chapter 5 the anomalous Hall and Nernst conductivity results in several noncollinear antiferromagnets and ferromagnets are discussed and further detailed analysis of the workflow used is provided. Finally, in Chapter 6 an overview and the outlook of my work is provided.

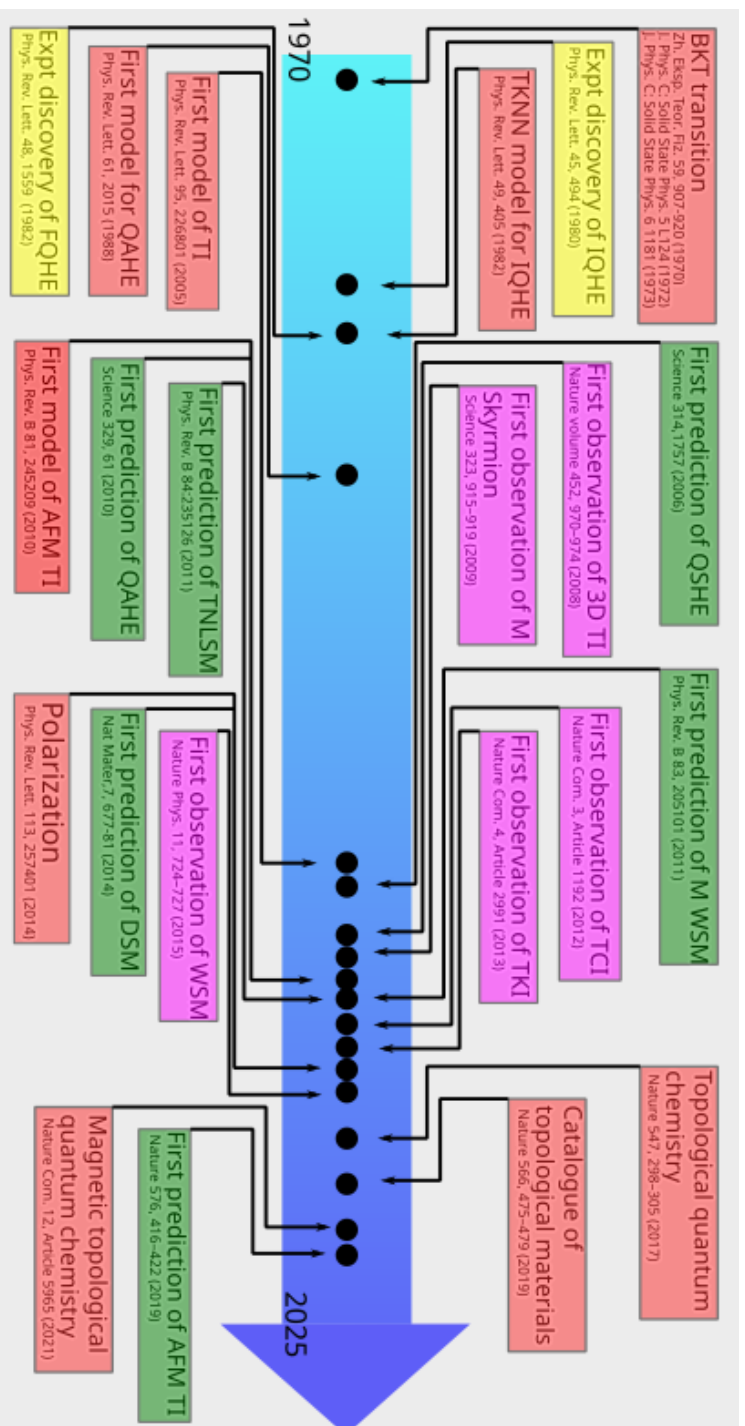


Figure 1.2.: Timeline of progress in topological materials

2. Density Functional Theory

2.1. Many-body problem

The non-relativistic many-body Hamiltonian of a quantum system that describes interactions between electrons and nuclei reads:

$$H = - \sum_i \frac{\hbar^2}{2m} \nabla_i^2 - \sum_I \frac{\hbar^2}{2M_I} \nabla_I^2 - \sum_i \sum_I \frac{Z_I e^2}{|\mathbf{r}_i - \mathbf{R}_I|} + \frac{1}{2} \sum_i \sum_{j \neq i} \frac{e^2}{|\mathbf{r}_i - \mathbf{r}_j|} + \sum_I \sum_J \frac{Z_I Z_J e^2}{|\mathbf{R}_I - \mathbf{R}_J|}, \quad (2.1)$$

with m , \mathbf{r} and e being the mass, the position vector and the charge of electrons, M and \mathbf{R} that of the nuclei respectively and Z the atomic number. From now on, the lower case letters in summation will refer to the electrons whereas the capital letters to the nuclei, unless specified differently. The Hamiltonian of Eq. 2.1 consists of five terms, the first two of which describe the kinetic energy of the electrons and the nuclei respectively. The third term is the attractive interactions between electrons and nuclei. Finally, the last two terms denote the repulsive interactions between electrons, excluding self interaction, and the repulsive interactions between nuclei.

In principle, the ground state of the system can be found by solving the Schrödinger equation using this interacting Hamiltonian:

$$H\Psi = E\Psi. \quad (2.2)$$

Even though this task might sound straightforward and easy, in reality though, it is extremely challenging. The problem arises from the fact that the Hamiltonian of Eq. 2.1 describes a quantum system of $3(N_{elec} + N_{nuc})$ degrees of freedom (3 degrees of freedom for each of the electrons and nuclei), giving rise to an extremely large number of degrees of freedom for real materials, making it intractable even by using the most powerful

supercomputers. Given this complexity, it is obvious that certain approximations have to be considered in order to proceed.

The first approximation used is the so-called Born-Oppenheimer approximation [16]. Motivated by the fact that the mass of a nucleus is much larger than that of an electron ($M_{nuc} \gg m_e$), it is possible to separate the motion of an electron from that of the nuclei. As a consequence, the kinetic energy of the nuclei (second term in Eq. 2.1) is neglected and the nuclear-nuclear repulsion (fifth term in Eq. 2.1) is a constant and therefore neglected. Hence, the remaining three terms constitute the electronic part of the Hamiltonian, according to:

$$H_{el} = - \sum_i \frac{\hbar^2}{2m} \nabla_i^2 - \sum_i \sum_I \frac{Z_I e^2}{|\mathbf{r}_i - \mathbf{R}_I|} + \frac{1}{2} \sum_i \sum_{j \neq i} \frac{e^2}{|\mathbf{r}_i - \mathbf{r}_j|}. \quad (2.3)$$

Under the current approximation, the Schrödinger equation of the electronic part of the Hamiltonian is:

$$H_{el}(\mathbf{r}, \mathbf{R}) \psi_i(\mathbf{r}, \mathbf{R}) = U(\mathbf{R}) \psi_i(\mathbf{r}, \mathbf{R}). \quad (2.4)$$

with U being the electronic eigenvalues for the fixed nuclei. Solving Eq. 2.4 for different fixed values of nuclei positions, we get the form of the effective mean field potential for the electronic states, also called adiabatic potential energy surface.

The potential energy surface describes the electronic states on which the nuclei move and it is important for the nuclear degree of freedom, where the Hamiltonian reads:

$$H_{nuc} = - \sum_I \frac{\hbar^2}{2M_I} \nabla_I^2 + U(\mathbf{R}). \quad (2.5)$$

It is noted that the potential energy surface can be expanded according to:

$$U(\mathbf{R}) = U(\mathbf{R}_0) + \frac{\partial^2 U}{\partial \delta_1 \partial \delta_2}, \quad (2.6)$$

with δ being a small displacement giving rise to the interatomic force constant and hence phonons.

2.2. Hartree approximation

One of the simplest approximations to solve the many problem is the Hartree approximation [63]. Within this framework we consider that the electrons are independent (they

do not interact), which allows us to write the total wavefunction as a product of electron wavefunctions according to:

$$\psi(\mathbf{r}_1\sigma_1, \dots, \mathbf{r}_N\sigma_N) = \prod_{i=1}^N \psi_i(\mathbf{r}_i\sigma_i), \quad (2.7)$$

where it is noted that the antisymmetry of the wavefunction is neglected. Then, the variational principle is applied according to:

$$\langle H \rangle_{\Psi} = \langle \Psi | H | \Psi \rangle. \quad (2.8)$$

Therefore, we have to find Ψ minimizing the average Hamiltonian that reads:

$$\begin{aligned} \langle H \rangle_{\Psi} = & \sum_{\sigma} \sum_i \int d\mathbf{r} \psi_i^*(\mathbf{r}, \sigma) \left(-\frac{1}{2} \nabla^2 + u_{ion}(\mathbf{r}) \right) \psi_i^*(\mathbf{r}, \sigma) + \\ & + \frac{1}{2} \sum_{(j,\sigma') \neq (i,\sigma)} \int d\mathbf{r} d\mathbf{r}' \frac{1}{|\mathbf{r} - \mathbf{r}'|} |\psi_i(\mathbf{r}, \sigma)|^2 |\psi_j(\mathbf{r}', \sigma')|^2, \end{aligned} \quad (2.9)$$

with $u_{ion} = \sum_I \frac{Z_I}{|\mathbf{r}_i - \mathbf{R}_I|}$. Using the Lagrange multipliers method to the wavefunction:

$$F[\{\psi(\mathbf{r}, \sigma)\}, \lambda_i] = \langle H \rangle_{\Psi} - \sum_i \lambda_i \left(\sum_{\sigma} \int d\mathbf{r} |\psi(\mathbf{r}, \sigma)|^2 - 1 \right), \quad (2.10)$$

and after applying the functional derivative minimization condition $\frac{\delta F}{\delta \psi_i^*} = 0$, we end up to the Hartree equations:

$$-\frac{1}{2} \nabla^2 \psi_i(\mathbf{r}, \sigma) + u_{ion}(\mathbf{r}) \psi_i(\mathbf{r}, \sigma) + \sum_{(j,\sigma') \neq (i,\sigma)} \int d\mathbf{r}' \frac{|\psi_j(\mathbf{r}', \sigma')|^2}{|\mathbf{r} - \mathbf{r}'|} \psi_i(\mathbf{r}, \sigma) = \epsilon_i \psi_i(\mathbf{r}, \sigma). \quad (2.11)$$

The three terms of the Hartree equations correspond to the kinetic energy of the electrons, the ionic contribution and the potential energy that an electron can see due to the presence of the others, also known as Hartree term respectively.

2.3. Hartree-Fock approximation

In Hartree approximation one neglects the antisymmetric nature of the wavefunction under the exchange of two electrons. Another approximation that takes into account this

property is the Hartree-Fock approximation [188, 39]. In this picture, the electrons are still independent therefore the total wavefunction is written by the slater determinant:

$$\psi(\mathbf{r}_1\sigma_1, \mathbf{r}_2\sigma_2, \dots, \mathbf{r}_N\sigma_N) = \frac{1}{\sqrt{N!}} \begin{vmatrix} \psi_1(\mathbf{r}_1\sigma_1) & \psi_1(\mathbf{r}_2\sigma_2) & \dots & \psi_1(\mathbf{r}_N\sigma_N) \\ \psi_2(\mathbf{r}_1\sigma_1) & \psi_2(\mathbf{r}_2\sigma_2) & \dots & \psi_2(\mathbf{r}_N\sigma_N) \\ \vdots & \vdots & \ddots & \vdots \\ \psi_N(\mathbf{r}_1\sigma_1) & \psi_N(\mathbf{r}_2\sigma_2) & \dots & \psi_N(\mathbf{r}_N\sigma_N) \end{vmatrix} \quad (2.12)$$

In this case the average Hamiltonian is:

$$\begin{aligned} \langle H \rangle_\Psi &= \sum_\sigma \sum_i \int d\mathbf{r} \psi_i^*(\mathbf{r}, \sigma) \left(-\frac{1}{2} \nabla^2 + u_{ion}(\mathbf{r}) \right) \psi_i(\mathbf{r}, \sigma) + \\ &+ \frac{1}{2} \sum_{\sigma, \sigma'} \sum_{i, j} \int d\mathbf{r} d\mathbf{r}' \psi_i^*(\mathbf{r}, \sigma) \psi_j^*(\mathbf{r}', \sigma') \frac{1}{|\mathbf{r} - \mathbf{r}'|} \psi_i(\mathbf{r}, \sigma) \psi_j(\mathbf{r}', \sigma') - \\ &- \frac{1}{2} \sum_\sigma \sum_{i, j} \int d\mathbf{r} d\mathbf{r}' \psi_i^*(\mathbf{r}, \sigma) \psi_j^*(\mathbf{r}', \sigma) \frac{1}{|\mathbf{r} - \mathbf{r}'|} \psi_j(\mathbf{r}, \sigma) \psi_i(\mathbf{r}', \sigma). \end{aligned} \quad (2.13)$$

Eq. 2.13 consists of three terms being the single body expectation values, the Hartree (direct) and the Fock (exchange) respectively. The direct term involves the Coulomb interaction between electrons while the exchange includes the Pauli exclusion principle. An immediate observation in both direct and exchange terms is the absence of the $i = j$ restriction, allowing electrons to interact with themselves, giving rise to the so called self interaction. This issue is bypassed though due to the sign difference, leading to the complete cancellation of the respective self interaction terms. Similarly to the Hartree case, the variational condition $\frac{\delta F}{\delta \psi_i^*} = 0$ applied to Eq. 2.10 with $\langle H \rangle_\Psi$ from Eq. 2.13 leads to the Hartree-Fock equations:

$$\begin{aligned} &\left[-\frac{1}{2} \nabla^2 + u_{ion}(\mathbf{r}) + \sum_j \sum_{\sigma'} \int d\mathbf{r}' \psi_j^*(\mathbf{r}', \sigma') \psi_j(\mathbf{r}', \sigma') \frac{1}{|\mathbf{r} - \mathbf{r}'|} \right] \psi_i(\mathbf{r}, \sigma) - \\ &- \sum_j \int d\mathbf{r}' \psi_j^*(\mathbf{r}', \sigma) \psi_i^*(\mathbf{r}', \sigma) \frac{1}{|\mathbf{r} - \mathbf{r}'|} \psi_j(\mathbf{r}, \sigma) = \epsilon_i \psi_i(\mathbf{r}, \sigma). \end{aligned} \quad (2.14)$$

The presence of the exchange term makes the equations nonlinear integro-differential and hence their solution intractable. Since the electron density is given by $n(\mathbf{r}) =$

$\sum_{\sigma} \sum_i |\psi_i(\mathbf{r}, \sigma)|^2$, the Hartree-Fock equations can be written as a function of density. Self-consistent methods are used to solve these types of equations. This is achieved by guessing an initial density, $n(\mathbf{r})$, constructing a potential, solving the Hartree-Fock equations and obtaining the new density. If the new density is not consistent with the initial, it is inserted in the equations again. The process is repeated until the initial and the new densities are consistent with each other. From the final density, the wavefunction is obtained.

2.4. Density functional theory

The techniques based on wavefunctions discussed so far are complicated and hence intractable for large systems, therefore the need to switch to a different fundamental variable becomes of vital importance. In density functional theory, the electron density is used as the main variable which leads to a reduction of the degrees of freedom from $3N$ to just 3. The first attempt to apply density functional theory in practice for quantum systems was performed in 1927 by Thomas [204] and Fermi [37]. Although the approach is not accurate enough, it illustrates the simplest example of density functional theory. The idea is to approximate the kinetic energy of the system of electrons with the functional of density of non interacting electrons in a homogeneous gas with density equal to the local density at any given point. The main core of the density functional theory is the two Hohenberg-Kohn theorems. [70]

2.4.1. Hohenberg-Kohn theorems

Theorem 1:

There exists an one to one correspondence between the ground state energy density and the external potential.

Proof of theorem 1:

Suppose that there are two different external potentials $V_{ext}^{(1)}$ and $V_{ext}^{(2)}$ that lead to the same ground state density $n_0(\mathbf{r})$. As a consequence, the Hamiltonians $H^{(1)}$ and $H^{(2)}$ containing these external potentials will also be different as well as the ground state wave functions $\psi^{(1)}$ and $\psi^{(2)}$ being the solutions of them.

Since $\psi^{(1)} \neq \psi^{(2)}$, $\psi^{(2)}$ is not the ground state wave function of $H^{(1)}$, therefore it obeys [5, 106, 105, 31]

$$E^{(1)} = \langle \psi^{(1)} | H^{(1)} | \psi^{(1)} \rangle < \langle \psi^{(2)} | H^{(1)} | \psi^{(2)} \rangle, \quad (2.15)$$

using $H^{(1)} = H^{(2)} + H^{(1)} - H^{(2)}$, we can rewrite the right part of the inequality of Eq. 2.15 as follows:

$$\begin{aligned}\langle \psi^{(2)} | H^{(1)} | \psi^{(2)} \rangle &= \langle \psi^{(2)} | H^{(2)} | \psi^{(2)} \rangle + \langle \psi^{(2)} | H^{(1)} - H^{(2)} | \psi^{(2)} \rangle \\ &= E^{(2)} + \int d\mathbf{r} \left(V_{ext}^{(1)}(\mathbf{r}) - V_{ext}^{(2)}(\mathbf{r}) \right) n_0(\mathbf{r}).\end{aligned}\quad (2.16)$$

So, combining 2.15 and 2.16, we get:

$$E^{(1)} < E^{(2)} + \int d\mathbf{r} \left(V_{ext}^{(1)}(\mathbf{r}) - V_{ext}^{(2)}(\mathbf{r}) \right) n_0(\mathbf{r}).\quad (2.17)$$

Similarly, for $E^{(2)}$, we have

$$E^{(2)} < E^{(1)} + \int d\mathbf{r} \left(V_{ext}^{(2)}(\mathbf{r}) - V_{ext}^{(1)}(\mathbf{r}) \right) n_0(\mathbf{r}).\quad (2.18)$$

Adding the inequalities 2.17 and 2.18, we get:

$$E^{(1)} + E^{(2)} < E^{(1)} + E^{(2)},\quad (2.19)$$

which is not valid, therefore the initial assumption cannot be met and different external potentials lead to different densities.

Theorem 2: *A universal functional for the energy $E[n]$ in terms of the density $n(r)$ can be defined, for any V_{ext} . The exact ground state energy of the system is the global minimum, and the density that minimizes this functional is the exact ground state.*

Proof of theorem 2:

We consider a system with ground state density $n^{(1)}(r)$ corresponding to $V_{ext}^{(1)}$. The energy is then given by:

$$E^{(1)} = E[n^{(1)}] = \langle \psi^{(1)} | H^{(1)} | \psi^{(1)} \rangle.\quad (2.20)$$

Now we consider a different density $n^{(2)}(r)$, which necessarily corresponds to a different

wavefunction $\psi^{(2)}$. It follows that the energy of the state $E^{(2)}$ is greater than $E^{(1)}$, according to:

$$E^{(1)} = \langle \psi^{(1)} | H^{(1)} | \psi^{(1)} \rangle < \langle \psi^{(2)} | H^{(1)} | \psi^{(2)} \rangle. \quad (2.21)$$

Thus, the energy $E[n^{(1)}]$ is lower than the value of the expression of 2.21 for any other density. Minimizing the energy functional in respect to the electronic density will give us the ground state density.

As a corollary, the outcome of the Hohenberg-Kohn theorems is that the ground state electron density completely determines all the properties of the system. Additionally, an energy functional $E[n(\mathbf{r})]$ that determines the ground state energy and density of the form:

$$\begin{aligned} E_{HK}[n] &= T[n] + E_{int}[n] + \int d\mathbf{r} V_{ext}(\mathbf{r}) n(\mathbf{r}) = \\ &= F_{HK}[n] + \int d\mathbf{r} V_{ext}(\mathbf{r}) n(\mathbf{r}), \end{aligned} \quad (2.22)$$

can be constructed. It is noted that Hohenberg and Kohn themselves named their paper "inhomogeneous electron gas" in their attempt to build on the top of the already existing "homogeneous electron gas" approach. Additionally, their original theorems are valid at $T = 0$. Later, Mermin extended the theorems to finite temperature [129].

2.4.2. Kohn-Sham ansatz

Even though the two Hohenberg-Kohn theorems simplify the many-body problem by proving that all the properties of a system are uniquely described by the energy functional, they do not give any recipe on how this functional should be constructed. In their attempt to deal with this problem, Kohn and Sham came with the idea of replacing the difficult interacting problem with a new different fictitious, non interacting system that could be solved easier. In this approach, the electrons do not interact with each other but instead with an effective potential originating from the nuclei and the other electrons. Kohn-Sham ansatz assumes that the ground state of the two systems is equal to each other and all difficult terms are included in a single term, the so-called exchange-correlation functional. [92] A visual representation of the Kohn-Sham ansatz is illustrated in Fig. 2.1.

The Hamiltonian of the fictitious non interacting system is given by:

$$H_{fic} = -\frac{1}{2}\nabla^2 + V(\mathbf{r}). \quad (2.23)$$

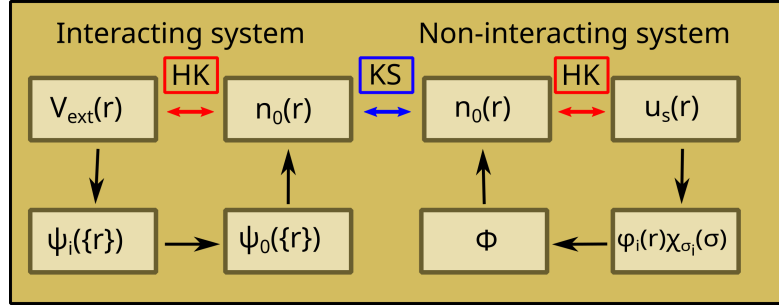


Figure 2.1.: Schematic representation of the Kohn-Sham ansatz

The first term on the right hand side of Eq. 2.23 is the usual kinetic operator whereas the second one is the effective local potential that includes the external potential, the Hartree term and the exchange correlation functional according to:

$$V(\mathbf{r}) = V_{ext}(\mathbf{r}) + V_{Hartree}(\mathbf{r}) + V_{XC}(\mathbf{r}). \quad (2.24)$$

It is noted that using the one-electron Hamiltonian for the fictitious system is sufficient since all electrons are equivalent. Considering a quantum system of N non interacting electrons, the density obeys:

$$n(\mathbf{r}) = \sum_i |\psi_i(\mathbf{r})|^2, \quad (2.25)$$

and the energy functional of the Kohn-Sham approach, using the Hamiltonian of the fictitious system of Eq. 2.23, is given by:

$$\begin{aligned} E_{KS}[n] &= T_s[n] + \int d\mathbf{r} V(\mathbf{r}) n(\mathbf{r}) = \\ &= T_s[n] + \int d\mathbf{r} V_{ext}(\mathbf{r}) n(\mathbf{r}) + E_{Hartree}[n] + E_{XC}[n] = \\ &= \frac{1}{2} \sum_i \int d\mathbf{r} |\nabla \psi_i^\sigma(\mathbf{r})|^2 + \int d\mathbf{r} V_{ext}(\mathbf{r}) n(\mathbf{r}) + \frac{1}{2} \int d\mathbf{r} d\mathbf{r}' \frac{n(\mathbf{r}) n(\mathbf{r}')}{|\mathbf{r} - \mathbf{r}'|} + E_{XC}[n], \end{aligned} \quad (2.26)$$

where the Hartree term includes the classical Coulomb interaction of the electron density with itself and V_{ext} the external potential due to nuclei and other electrons.

2.4.3. Kohn-Sham equations

The solution of Kohn-Sham system is obtained using the variational principle to the Lagrangian, that respect the conservation of particles, as expressed by:

$$L = E_{KS} - \sum_i \lambda_i \left(\int d\mathbf{r} \psi_i^*(\mathbf{r}) \psi_i(\mathbf{r}) - 1 \right). \quad (2.27)$$

Minimizing with respect to the wavefunction $\psi_i(\mathbf{r})$, we get:

$$\frac{\delta L}{\delta \psi_i^*(\mathbf{r})} = 0. \quad (2.28)$$

Since the kinetic term is only a function of the wavefunction, we only have to apply the chain rule to the rest in order to obtain:

$$\begin{aligned} \frac{\delta T_s}{\delta \psi_i^*(\mathbf{r})} + \frac{\delta E_{ext}}{\delta \psi_i^*(\mathbf{r})} + \frac{\delta E_{Hartree}}{\delta \psi_i^*(\mathbf{r})} + \frac{\delta E_{XC}}{\delta \psi_i^*(\mathbf{r})} &= 0 \Leftrightarrow \\ \frac{\delta T_s}{\delta \psi_i^*(\mathbf{r})} + \frac{\delta E_{ext}}{\delta n(\mathbf{r})} \frac{\delta n(\mathbf{r})}{\delta \psi_i^*(\mathbf{r})} + \frac{\delta E_{Hartree}}{\delta n(\mathbf{r})} \frac{\delta n(\mathbf{r})}{\delta \psi_i^*(\mathbf{r})} + \frac{\delta E_{XC}}{\delta n(\mathbf{r})} \frac{\delta n(\mathbf{r})}{\delta \psi_i^*(\mathbf{r})} &= 0. \end{aligned} \quad (2.29)$$

The functional derivatives of T_s and density $n(\mathbf{r})$ in respect to the wavefunction, are given by:

$$\begin{aligned} \frac{\delta T_s}{\delta \psi_i^*(\mathbf{r})} &= -\frac{1}{2} \nabla^2 \psi_i(\mathbf{r}) \\ \frac{\delta n(\mathbf{r})}{\delta \psi_i^*(\mathbf{r})} &= \psi_i^*(\mathbf{r}). \end{aligned} \quad (2.30)$$

Using the Lagrange multiplier method and the above functional derivatives, we lead to the Kohn-Sham Schrödinger like equation that is written as follows:

$$(H_{KS}(\mathbf{r}) - \epsilon_i) \psi_i(\mathbf{r}) = 0, \quad (2.31)$$

where ϵ_i , H_{KS} denote the energy eigenvalues and the effective Kohn-Sham Hamiltonian respectively. The latter is given by:

$$\begin{aligned}
H_{KS}(\mathbf{r}) &= -\frac{1}{2}\nabla^2 + V_{KS}(\mathbf{r}) = \\
&= -\frac{1}{2}\nabla^2 + V_{ext}(\mathbf{r}) + \frac{\delta E_{Hartree}}{\delta n(\mathbf{r})} + \frac{\delta E_{XC}}{\delta n(\mathbf{r})} = \\
&= -\frac{1}{2}\nabla^2 + V_{ext}(\mathbf{r}) + V_{Hartree}(\mathbf{r}) + V_{XC}(\mathbf{r}).
\end{aligned} \tag{2.32}$$

Eq. 2.31 and Eq. 2.32 are the so-called Kohn-Sham equations.

The Kohn-Sham equations can be solved self-consistently. In short, an initial guess of the electron density is provided and the calculation of the effective potential follows. Subsequently, the Kohn-Sham equations are solved and a new electron density is found. The process is repeated until the desired convergence criteria regarding the initial and the new densities are reached. Finally, the ground state and density that leads to the physical properties is obtained. As becomes clear, Kohn-Sham method results to the exact ground state and energy of the interacting system provided that the exact exchange correlation functional is known. In other words the accuracy of the method depends on the choice of the exchange correlation functional.

2.4.4. Exchange-correlation functionals

As previously discussed, the choice of the correct exchange correlation functional is of great importance and determines the accuracy of the results obtained from the Kohn-Sham method. In an attempt to probe the exchange correlation term, we look closer to Eq. 2.26 that reveals the presence of self interaction terms within the Hartree potential. Obviously these terms have to be excluded, therefore one compensates for them in the exchange correlation functional. Additionally, the differences between the kinetic energies of the non interacting and the interacting systems are included too. In general, the exchange correlation functional includes all the unknown terms, can be decomposed in two terms *i.e.* the exchange term and the correlation term based on:

$$E_{XC}[n] = E_X[n] + E_C[n], \tag{2.33}$$

and can be further approximated as a local, semi-local or nonlocal functional of the density. A schematic representation of the accuracy of the exchange correlation functional is the Jacob's ladder illustrated in Fig. 2.2. The bottom of the ladder represents the absence of the exchange correlation functional, whereas the top the exact exchange correlation functional that gives the exact energy density of the Kohn-Sham equations. Starting from the bottom, each step in between corresponds to different exchange correlation functionals that are

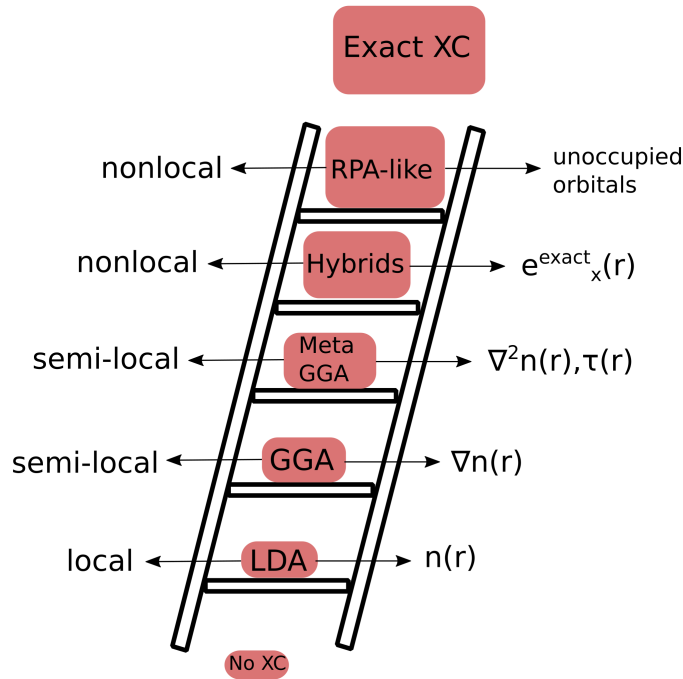


Figure 2.2.: Jacob's ladder of exchange correlation functionals and their building blocks

used for calculations and their building blocks depend on different functions of the density functional. It is noted that the complexity, the accuracy as well as the computational cost increase as we move higher in the ladder. Below we briefly introduce the local density approximation (LDA) and the generalized gradient approximation (GGA). The interested reader can find more information regarding the exchange correlation functionals in the following textbooks [124, 183].

Local density approximation

In this approximation, the exchange correlation energy of an inhomogeneous gas with density n is assumed to be equal to the exchange correlation energy of the homogeneous electron gas with the same density n [70], as given by:

$$E_{XC}^{LDA}[n] = \int d\mathbf{r} n(\mathbf{r}) \epsilon_{XC}^{hom}(n(\mathbf{r})), \quad (2.34)$$

where ϵ_{XC}^{hom} denotes the exchange correlation energy density of the homogeneous gas.

Since the exchange term is given by:

$$E_X[n] = -\frac{1}{2} \int d\mathbf{r}d\mathbf{r}' \frac{n^2}{|\mathbf{r} - \mathbf{r}'|}, \quad (2.35)$$

following Ref. [159], we obtain the expression of the homogeneous gas:

$$\epsilon_X^{hom}[n] = -\frac{3}{4} \left(\frac{3}{\pi}\right)^{\frac{1}{3}} n^{\frac{1}{3}}. \quad (2.36)$$

Unfortunately, there is no analytical expression to describe the correlation term, similar to the exchange. Therefore, if one calculates the total energies of the homogeneous gas, then it will be possible to obtain the correlation energies simply by subtracting the exchange energies from the total energies. Quantum Monte Carlo simulations have been performed in order to compute the total energy of the fully interacting homogeneous electron gases for several densities [24, 3], which were subsequently used to design local functionals of the density by fitting the obtained results.

The local density approximation gives good results in systems that adopt covalent, ionic or metal bonds but it underestimates the exchange energy and overestimates the binding energy. Despite these deficiencies, several LDA exchange correlation functionals such as VWN [217], PZ81 [160], CP [29], PW92 [159] are used in modern day density functional theory calculations.

Generalized gradient approximation

The next step to construct an exchange correlation functional beyond the local density approximation is to start from the homogeneous gas, introduce a weak external potential and expand the exchange correlation energy in terms of the density, according to the general formula:

$$\epsilon_{XC}(\mathbf{r}) = \epsilon_{XC}^{(0)}(\mathbf{r}) + \epsilon_{XC}^{(1)}(\mathbf{r}) + \epsilon_{XC}^{(2)}(\mathbf{r}) \cdots +, \quad (2.37)$$

where the index in the parenthesis corresponds to the gradient order. Even though this expansion, known as gradient expansion approximation (GEA) [187], contains higher order density correction terms, it does not have the desired results. It was later found that the reason of this failure was the violation of the so-called sum rule of the correlation density ($\int n_C(\mathbf{r}, \mathbf{r}') d\mathbf{r} = 0$) and the non-positivity constraint of the exchange density ($n_X(\mathbf{r}, \mathbf{r}') \leq 0$). Detailed explanation is provided in Ref. [170]. The problem was later solved by Perdew in Ref. [156] by introducing delta functions cutoffs that terminated the GEA exchange correlation hole in real space and hence restoring the summation rule and the non-positivity constraint. This technique provided the basis of the generalized

gradient approximation (GGA). As a result the exchange correlation functional within the GGA is written as:

$$E_{XC}^{GGA}[n] = \int d\mathbf{r} n(\mathbf{r}) \epsilon_{XC}^{hom}[n(\mathbf{r})] F_{XC}[n(\mathbf{r}), \nabla n(\mathbf{r})]. \quad (2.38)$$

with $F_{XC}[n(\mathbf{r}), \nabla n(\mathbf{r})]$ being known as the enhancement factor that modifies the LDA exchange correlation potentials.

Since the enhancement factor is not a unique function of the density, different approaches to the GGA exchange correlation functionals exist. On the one hand, the functionals with empirical parameters that are found by fitting with experimental results, such as B88 [8], FT98 [38] and on the other hand the functionals without empirical parameters, directly obtained from first principles calculations, such as B86 [7], PBE [157].

One of the most widespread exchange correlation functionals is the Perdew-Burke-Ernzerhof (PBE) [157], where the exchange and the correlation terms are given by:

$$\begin{aligned} E_X^{GGA} &= \int d\mathbf{r} n(\mathbf{r}) \epsilon_x^{hom}(n) F_X^{PBE}(s) \\ F_X^{PBE}(s) &= \left[1 + \kappa - \frac{\kappa}{1 + \beta \pi^2 s(\mathbf{r})^2 / 3\kappa} \right] \\ s(\mathbf{r}) &= \frac{|\nabla n(\mathbf{r})|}{2n(\mathbf{r}) k_F(\mathbf{r})} \\ \kappa &= 0.804 \\ \beta &= 0.066725 \end{aligned} \quad (2.39)$$

and

$$\begin{aligned}
E_C^{GGA} &= \int d\mathbf{r} n(\mathbf{r}) \left[\epsilon_C^{hom}(\mathbf{r}) + H^{PBE}(r_s, t) \right] \\
H^{PBE}(r_s, t) &= \frac{\beta^2}{2\alpha} \ln \left(1 + \frac{2\alpha}{\beta} \frac{t^2 + At^4}{1 + At^2 + A^2t^4} \right) \\
A &= \frac{2\alpha}{\beta e^{\frac{-2\alpha\epsilon_C^{hom}(n)}{\beta^2}} - 1} \\
t &= \frac{|\nabla n(\mathbf{r})|}{2k_s n} \\
k_s &= \sqrt{4k_F/\pi} \\
\alpha &= 0.0716 \\
\beta &= 0.066725
\end{aligned} \tag{2.40}$$

Local density approximation vs generalized gradient approximation

A natural question that needs to be addressed is which of these two aforementioned exchange-correlation functionals has better agreement with the experiment. Despite the fact that there is no functional to perfectly describe all properties of all materials, a few comparisons of them are possible.

Starting from the LDA, an underestimation of the order of 10% is observed for the exchange functional and an overestimation of the order of 100% for the correlation functional. Since the exchange term is much larger than the correlation, LDA's underestimation/overestimation is compensated, giving rise to accurate results. Despite the error cancellation of LDA, GGA has a much better performance by underestimating both exchange and correlation terms by approximately 1% and 5% respectively [102], giving rise to more accurate results.

Considering the crystal structure, LDA and GGA have comparable performance, with the first one underestimating the bond lengths and the second one overestimating them [55]. The lattice constants of alkali metals are 4% smaller in LDA but right in GGA [161]. Similar behaviour is observed in the third-row elements (K, Ca, V, Fe, Cu) presented in Ref. [4] and in transition metals [150].

Another the quantity in which GGA has a better performance over LDA is the total energy. Studies have shown that LDA predicts that the non magnetic bcc Fe state is energetically more favorable than the ferromagnetic fcc when LDA is used. The experimental result is attained by employing the GGA [4].

Regarding the cohesive [162, 151, 128], atomization [157] and binding energies [243, 154, 155], GGA has once again better performance.

In general, despite being computationally more expensive, GGA exchange correlation functionals has a better performance over LDA [89]. Some examples are illustrated in Tab. 2.1.

Table 2.1.: LDA and GGA

Property	LDA	GGA
Exchange energy	10% underestimation	1% underestimation
Correlation energy	100% overestimation	5% underestimation
Cohesive energy	15% overestimation	4% overestimation
Bond length	2% underestimation	2% overestimation
Activation energy	100% underestimation	30% underestimation

2.5. Spin-polarized density functional theory

The density functional theory discussed so far provides the framework to perform calculations on non magnetic systems. The existence of magnetism in nature however requires slight modifications to the current theory, therefore in early 70s the spin polarized extension of the theory was introduced [216, 153, 50]. In this framework, the functionals were formulated in terms of the spin density matrix ρ , given by:

$$\rho_{\alpha\beta}(\mathbf{r}) = n(\mathbf{r})\delta_{\alpha\beta} + \mathbf{m}(\mathbf{r}) \cdot \sigma_{\alpha\beta}, \quad (2.41)$$

where $n(\mathbf{r})$ is the electronic density, $m(\mathbf{r})$ the magnetization density originating from the spin polarization and σ the Pauli matrices. Expanding the spin density formula by using $\mathbf{m}(\mathbf{r}) \cdot \sigma = m_x\sigma_x + m_y\sigma_y + m_z\sigma_z$, we can write it in a matrix form as:

$$\rho(\mathbf{r}) = \begin{bmatrix} n(\mathbf{r}) + m_z(\mathbf{r}) & m_x(\mathbf{r}) - im_y(\mathbf{r}) \\ m_x(\mathbf{r}) + im_y(\mathbf{r}) & n(\mathbf{r}) - m_z(\mathbf{r}) \end{bmatrix}. \quad (2.42)$$

In spin-polarized framework, the orbitals are spinors given by:

$$\Psi_i(\mathbf{r}) = \begin{bmatrix} \psi_{i\alpha}(\mathbf{r}) \\ \psi_{i\beta}(\mathbf{r}) \end{bmatrix}, \quad (2.43)$$

with α and β corresponding to the spin directions. The spin density in terms of the spinors is given by:

$$\rho(\mathbf{r}) = \sum_i \begin{bmatrix} \psi_{i\alpha}(\mathbf{r})\psi_{i\alpha}^*(\mathbf{r}) & \psi_{i\alpha}(\mathbf{r})\psi_{i\beta}^*(\mathbf{r}) \\ \psi_{i\beta}(\mathbf{r})\psi_{i\alpha}^*(\mathbf{r}) & \psi_{i\beta}(\mathbf{r})\psi_{i\beta}^*(\mathbf{r}) \end{bmatrix}. \quad (2.44)$$

While in the spin density functional theory framework, only the Zeeman term is taken into account, there exist another generalization of density functional theory, namely the current density functional theory, that deals with the coupling of the magnetic field to the orbitals allowing treatment of systems in strong magnetic fields [213, 212, 214, 167]. An exact connection of these two frameworks has been established by Capelle and Gross in Ref. [22].

The orientation of the spin quantization axis in a magnetic material determines the type of the material. Specifically, in case there is a common spin quantization axis, the material exhibits a collinear nature, whereas in the absence of it, a non-collinear. Next, we briefly discuss the differences in the formulation of the Kohn-Sham equations in these two types of magnetic materials.

Collinear magnetism

For collinear magnetic materials, it is noted that the non diagonal terms of the spin density matrix of Eq. 2.42 vanish, therefore the spin and magnetization density read:

$$\begin{aligned} n(\mathbf{r}) &= \sum_i \Psi_i^\dagger(\mathbf{r}) \mathbf{I} \Psi_i(\mathbf{r}) \\ \mathbf{m}(\mathbf{r}) &= \mu_B \sum_i \Psi_i^\dagger(\mathbf{r}) \boldsymbol{\sigma} \Psi_i(\mathbf{r}), \end{aligned} \quad (2.45)$$

with \mathbf{I} and $\boldsymbol{\sigma}$ being the identity matrix and the Pauli matrices respectively. Following the same procedure as in the non spin polarized case, we obtain the energy functional for the spin polarized case:

$$\begin{aligned} E_{KS}[\rho] &= T[\rho] + E_H[n] + E_{ext}[\rho] + E_{XC}[\rho] = \\ &= T[\rho] + \int d\mathbf{r} d\mathbf{r}' \frac{n(\mathbf{r}) n(\mathbf{r}')}{|\mathbf{r} - \mathbf{r}'|} + \sum_{\alpha\beta} \int d\mathbf{r} V_{ext}^{\alpha\beta}(\mathbf{r}) \rho_{\alpha\beta}(\mathbf{r}) + E_{XC}[\rho], \end{aligned} \quad (2.46)$$

and also the spin-dependent Kohn-Sham equations:

$$\sum_{\beta} \left[-\delta_{\alpha\beta} \frac{1}{2} \nabla^2 + V_{ext}^{\alpha\beta}(\mathbf{r}) + \delta_{\alpha\beta} \int \frac{n(\mathbf{r}')}{|\mathbf{r} - \mathbf{r}'|} d\mathbf{r}' + V_{XC}^{\alpha\beta}(\mathbf{r}) \right] \psi_{i\beta}(\mathbf{r}) = \delta_{\alpha\beta} \epsilon_i \psi_{i,\beta}(\mathbf{r}), \quad (2.47)$$

with:

$$V_{XC}^{\alpha\beta}(\mathbf{r}) = \frac{\delta E_{XC}[\rho]}{\delta \rho_{\alpha\beta}(\mathbf{r})}. \quad (2.48)$$

Non-collinear magnetism

For non-collinear magnetic materials, each electron must be treated as a two-component spinor, such as in Eq. 2.43. Its quantization axis is given by the spin-1/2 rotation matrix:

$$U(\theta, \phi) = \begin{bmatrix} \cos(\theta/2) e^{i\phi/2} & \sin(\theta/2) e^{-i\phi/2} \\ -\sin(\theta/2) e^{i\phi/2} & \cos(\theta/2) e^{-i\phi/2} \end{bmatrix}, \quad (2.49)$$

where θ and ϕ are the polar and the azimuthal angles of the spherical coordinates respectively that determine the direction of each spin. As a result, the form of the spinor obeys:

$$\begin{bmatrix} \psi_\alpha(\mathbf{r}) \\ \psi_\beta(\mathbf{r}) \end{bmatrix} = U(\theta(\mathbf{r}), \phi(\mathbf{r})) \begin{bmatrix} 1 \\ 0 \end{bmatrix}, \quad (2.50)$$

and the non diagonal spin density matrix is given by:

$$\rho(\mathbf{r}) = \begin{bmatrix} \rho_{\alpha\alpha}(\mathbf{r}) & \rho_{\alpha\beta}(\mathbf{r}) \\ \rho_{\beta\alpha}(\mathbf{r}) & \rho_{\beta\beta}(\mathbf{r}) \end{bmatrix}. \quad (2.51)$$

Comparing with the collinear case we observe that the off-diagonal terms are responsible for the non-collinearity of the magnetic structure. Additionally, since the Kohn-Sham equations of Eq. 2.47 do not include any magnetization direction constraints, the two cases share the same Kohn-Sham equations.

2.6. Relativistic effects

Since the origin of electron's spin and several other phenomena is of relativistic nature, a generalization of the density functional theory is substantial. The goal of the full relativistic treat of a quantum system is to efficiently describe molecules and solids by solving the many body Dirac equation (instead of the non relativistic Schrödinger equation):

$$H_D \psi_i = E_i \psi_i, \quad (2.52)$$

with

$$\begin{aligned}
H_D &= c\boldsymbol{\alpha} \cdot \mathbf{p} + \beta c^2 + V(\mathbf{r}) \\
\mathbf{p} &= -i\nabla \\
i &= (x, y, z) \\
\alpha_i &= \begin{bmatrix} 0 & \sigma_i \\ \sigma_i & 0_2 \end{bmatrix} \\
\beta &= \begin{bmatrix} \mathbf{I}_2 & 0_2 \\ 0_2 & -\mathbf{I}_2 \end{bmatrix},
\end{aligned} \tag{2.53}$$

with σ_i being the Pauli matrices and \mathbf{I}_2 the 2×2 identity matrix.

The notion of the density as a key variable as well as the existence of the Hohenberg-Kohn theorems form the basis of the density functional theory, as has already been discussed. In complete analogy, the one-to-one correspondence between the ground states $|\Psi_0\rangle$ (differ only by gauge transformation) and the associated four-current j_0^μ , given by:

$$j_0^\mu(\mathbf{r}) = \sum_k \Theta_k \psi_k^\dagger(\mathbf{r}) \alpha^\mu \psi_k(\mathbf{r}), \tag{2.54}$$

with

$$\Theta_k = \begin{cases} 0 & \text{for } \epsilon_k - 2mc^2 \\ 1 & \text{for } -2mc^2 < \epsilon_k \leq \epsilon_F \\ 0 & \text{for } \epsilon_F < \epsilon_k \end{cases} \tag{2.55}$$

render the latter as the key variable [165, 164, 119, 34] and combined with the generalization of the Hohenberg-Kohn theorems by Rajagopal and Callaway [165]:

$$E[j_0] < E[j], \tag{2.56}$$

with:

$$E[j] = \langle \Psi_0[j] | H | \Psi_0[j] \rangle, \tag{2.57}$$

form the basis of the relativistic counterpart. It is noted that the radiative corrections are ignored, a gauge ambiguity and nontrivial UV divergences exist, making the relativistic approach more challenging. Detailed analysis and explanation are outside of the scopes of this work, however, the interested reader can find more information in relevant sources [47, 33].

Plugging in the Dirac Hamiltonian in Eq. 2.57, we are able to decompose the energy functional of the current density to the kinetic, the external, the Hartree and the exchange-correlation parts according to:

$$E = T_s + E_{ext} + E_H + E_{XC}, \quad (2.58)$$

with:

$$\begin{aligned} T_s &= \sum_k \Theta_k \int d\mathbf{r} \psi_k^\dagger(\mathbf{r}) [-ic\boldsymbol{\alpha} \cdot \nabla + \beta c^2] \psi_k(\mathbf{r}) \\ E_{ext} &= \int d\mathbf{r} j_\mu(\mathbf{r}) V^\mu(\mathbf{r}) \\ E_H &= \frac{1}{2} \int d\mathbf{r} d\mathbf{r}' \frac{j_\mu(\mathbf{r}) j^\mu(\mathbf{r}')}{|\mathbf{r} - \mathbf{r}'|}. \end{aligned} \quad (2.59)$$

The minimization of the total energy functional, similarly to the non-relativistic case, leads to the relativistic Kohn-Sham equations [164, 119]:

$$[-ic\boldsymbol{\alpha} \cdot \nabla + \beta c^2 + \alpha_\mu u_s^\mu(\mathbf{r})] \psi_k(\mathbf{r}) = \epsilon_k \psi_k(\mathbf{r}), \quad (2.60)$$

with:

$$\begin{aligned} u_s^\mu(\mathbf{r}) &= V^\mu(\mathbf{r}) + u_H^\mu(\mathbf{r}) + u_{XC}^\mu(\mathbf{r}) \\ u_H^\mu(\mathbf{r}) &= e^2 \int d\mathbf{r}' \frac{j^\mu(\mathbf{r}')}{|\mathbf{r} - \mathbf{r}'|} \\ u_{XC}^\mu(\mathbf{r}) &= \frac{\delta E_{XC}[j]}{\delta j_\mu(\mathbf{r})}. \end{aligned} \quad (2.61)$$

In practice, relativistic effects are treated as perturbations from DFT codes [90]. For instance, VASP package performs fully relativistic calculations (solving relativistic Kohn-Sham equations) on the core electrons and treats the valence electrons in a scalar relativistic approximation [201], in which the relativistic contribution terms are included in the given pseudopotential [75, 203] and the spin orbit coupling [56] by using the second variation method.

Spin orbit coupling

The spin orbit coupling (SOC), as its name indicates, is a quantum mechanical interaction relating the spin of an electron with its motion inside a potential. Despite its weak magnitude, it is directly related to several interesting spintronics effects such as the magnetocrystalline anisotropy and the spin Hall effect. A simple way to explain this interaction follows.

Imagine an electron of nonzero orbital angular momentum ($l \neq 0$), orbiting around a nucleus. From the electrons perspective, the positively charged nucleus is rotating around itself, generating a positive current loop. As known from electromagnetism, any circular current induces a magnetic field, the direction of which is normal to the plane of the trajectory of the moving particle, pointing towards the direction determined by the right hand rule, given by:

$$\mathbf{B} = \frac{\mu_0 Z_e \mathbf{L}}{4\pi m_e r^3}. \quad (2.62)$$

The electron includes a fundamental and inseparable quantum mechanical property called spin that in turns create the spin angular momentum and the spin magnetic dipole moment, being anti-parallel to the spin angular momentum. The simultaneous presence of the spin magnetic dipole moment and the magnetic field, creates a torque that tends to rotate the spin magnetic dipole moment and hence altering its energy by:

$$\Delta E = -\xi \mathbf{S} \cdot \mathbf{L}. \quad (2.63)$$

Therefore, the interaction between the orbital angular momentum L of the nucleus and the electron spin angular momentum S is called spin orbit coupling with strength:

$$\xi = \frac{Z_e e^2}{8\pi\epsilon_0 m_e c^2 r^2}. \quad (2.64)$$

Since the strength of the spin orbit coupling is proportional to the atomic number, it becomes clear that the spin orbit interaction is stronger in larger atoms. Below we extract the spin orbit coupling formula starting from the Dirac equation.

The Dirac equation of Eq. 2.53 with the time independent scalar potential $-eV(\mathbf{r})$ and the vector potential $\mathbf{A}(\mathbf{r})$ can be written in matrix form as:

$$\begin{bmatrix} -eV(\mathbf{r}) + mc^2 & \boldsymbol{\sigma} \cdot (c\mathbf{p} + e\mathbf{A}(\mathbf{r})) \\ \boldsymbol{\sigma} \cdot (c\mathbf{p} + e\mathbf{A}(\mathbf{r})) & -eV(\mathbf{r}) - mc^2 \end{bmatrix} \begin{bmatrix} \phi \\ \chi \end{bmatrix} = E \begin{bmatrix} \phi \\ \chi \end{bmatrix}, \quad (2.65)$$

considering the definitions of α and β of Eq. 2.53. Performing the mathematical calculations, we obtain the following system of coupled equations:

$$\begin{aligned}(E' - mc^2 + eV(\mathbf{r}))\phi &= \boldsymbol{\sigma} \cdot (c\mathbf{p} + e\mathbf{A}(\mathbf{r}))\chi \\ (E' + mc^2 + eV(\mathbf{r}))\chi &= \boldsymbol{\sigma} \cdot (c\mathbf{p} + e\mathbf{A}(\mathbf{r}))\phi.\end{aligned}\quad (2.66)$$

The second equation can be solved for χ to give:

$$\chi = \frac{\boldsymbol{\sigma} \cdot (c\mathbf{p} + e\mathbf{A}(\mathbf{r}))}{E' + mc^2 + eV(\mathbf{r})}\phi \approx \frac{\boldsymbol{\sigma} \cdot (c\mathbf{p} + e\mathbf{A}(\mathbf{r}))}{2mc^2}\phi.\quad (2.67)$$

where we have used $eV(\mathbf{r}) \ll E' + mc^2 \approx 2mc^2$. Substituting Eq. 2.67 to the first equation of 2.66 leads to:

$$\left[E + eV(\mathbf{r}) - \frac{1}{2m} \left(\mathbf{p} + \frac{e}{c}\mathbf{A}(\mathbf{r}) \right)^2 \right] \phi = 0.\quad (2.68)$$

Following similar procedure but retaining terms up to order $(\frac{u}{c})^2$, we obtain the Pauli equation:

$$\begin{aligned}\left[E + eV(\mathbf{r}) - \frac{1}{2m} \left(\mathbf{p} + \frac{e}{c}\mathbf{A}(\mathbf{r}) \right)^2 + \frac{1}{2mc^2} (E + eV(\mathbf{r}))^2 + \right. \\ \left. + i \frac{e\hbar}{(2mc)^2} \mathbf{E}(\mathbf{r}) \cdot \mathbf{p} - \frac{e\hbar}{(2mc)^2} \boldsymbol{\sigma} \cdot (\mathbf{E}(\mathbf{r}) \times \mathbf{p}) - \frac{e\hbar}{2mc} \boldsymbol{\sigma} \cdot \mathbf{B}(\mathbf{r}) \right] \phi = 0,\end{aligned}\quad (2.69)$$

where the sixth term is the spin orbit coupling term:

$$\begin{aligned}\boldsymbol{\sigma} \cdot (\mathbf{E}(\mathbf{r}) \times \mathbf{p}) &= \boldsymbol{\sigma} \cdot (\nabla V(r) \times \mathbf{p}) = \frac{1}{r} \frac{dV(r)}{dr} \boldsymbol{\sigma} \cdot (\mathbf{r} \times \mathbf{p}) \\ &= \frac{1}{r} \frac{dV(r)}{dr} (\boldsymbol{\sigma} \cdot \mathbf{L}) = \xi \boldsymbol{\sigma} \cdot \mathbf{L}.\end{aligned}\quad (2.70)$$

2.7. Limitations of DFT

Despite the continuous improvement of the exchange-correlation functionals used, DFT remains an approximation, meaning that there are known cases with limited accuracy [77, 250, 28, 79], some of which are briefly discussed below.

As already analyzed, the core of DFT is the two Hohenberg-Kohn theorems which link the electron wavefunctions with the energy density, providing the basis to construct the

theory. The subtlety arises from the fact that the Hohenberg-Kohn theorems are only valid for the ground state of a quantum system and therefore excited states cannot be calculated in this framework. It is important to note that there are a methodologies to deal with excited states. A popular one is the so-called time-dependent density functional theory, which makes an one-to-one link between the time dependent density and the external potential, based on the Runge-Gross theorem [169]. An alternative approach is the so called GW approximation which is based on the expansion of the self energy in terms of the screened interaction quasiparticle [67, 68].

One of the most known DFT failures is the accurate description of the van der Waals interactions. The source of the error directly comes from the perturbation theory arguments [114] that demand an attractive part of the energy decaying as $\frac{1}{R^6}$ for the limit $R \rightarrow \infty$ for the accurate description. However, this condition cannot be fulfilled by any of the already existing LDA or GGA exchange-correlation functionals due to their local behaviour. As a result, the van der Waals interaction still remain a challenge for modern DFT [73].

Even though one electron systems are straightforward by solving the Schrödinger equation, the DFT technique still remains unchanged, using the density instead. This definition though includes interactions of the electron with itself, known as self-interactions, which are not physical and therefore have to be excluded. A successful exchange correlation functional must include terms to exactly cancel out the self interaction. Despite the improvement of the exchange-correlation functionals, there exist such delocalization and static correlation errors in simple systems, leading to wrong band gaps calculations [78, 23, 194, 17].

Standard DFT techniques have limited accuracy in describing strongly correlated systems. The Kohn-Sham ansatz relying on replacing the real interacting system with a fictitious non interacting one with the same density. This technique however includes a very cruel approximation that the net electron density of a single Slater determinant is a good approximation of the total electron density. In systems with partially filled f-orbitals however, the wavefunctions have contributions from multiple Slater determinants, making the theory less accurate [6, 158]. Since correlated systems can host interesting phenomena including superconductivity [19] and Mott transition [96], an accurate methodology is desirable. The nature of strongly correlated materials is nowadays treated using the dynamical mean field theory (DMFT) which maps a lattice problem to an impurity problem [18].

3. Topological properties

Let us consider a quantum system described by the Hamiltonian $H(\mathbf{r}, \boldsymbol{\lambda})$, where $\boldsymbol{\lambda}$ are parameters. The eigenvalues of the system are given by solving Schrödinger's equation:

$$H(\mathbf{r}, \boldsymbol{\lambda}) |n(\mathbf{r}, \boldsymbol{\lambda})\rangle = E_n(\boldsymbol{\lambda}) |n(\mathbf{r}, \boldsymbol{\lambda})\rangle. \quad (3.1)$$

An interesting question is how are the eigenfunctions of the system modified if the parameters $\boldsymbol{\lambda}$ are slowly changed in time.

3.1. Adiabatic evolution

The answer to the previous question leads to the adiabatic theorem of the quantum system [15].

A physical system remains in its instantaneous eigenstate if a perturbation is acting on it slowly enough and if there is a gap between the eigenvalue and the rest of the Hamiltonian spectrum.

We consider a Hamiltonian H and its eigenstate $|\psi_n\rangle$. By evolving in time, the state of the system at time t picks up a phase factor given by:

$$|\Psi_n(t)\rangle = e^{-iE_n t/\hbar} |\psi_n\rangle. \quad (3.2)$$

Therefore, the Schrödinger equation becomes:

$$H(t) |\psi_n(t)\rangle = E_n(t) |\psi_n(t)\rangle, \quad (3.3)$$

with a general solution of the form:

$$|\Psi(t)\rangle = \sum_n c_n(t) e^{i\theta_n(t)} |\psi_n(t)\rangle, \quad (3.4)$$

where θ is the dynamic phase factor, given by:

$$\theta_n(t) = -\frac{1}{\hbar} \int_0^t E_n(t') dt'. \quad (3.5)$$

Substituting Eq. 3.4 to Schrödinger equation, one obtains:

$$\begin{aligned} i\hbar \sum_n [\dot{c}_n |\psi_n\rangle + c_n |\dot{\psi}_n\rangle + i c_n |\psi_n\rangle \dot{\theta}_n] e^{i\theta_n} &= \sum_n c_n (H |\psi_n\rangle) e^{i\theta_n} \Leftrightarrow \\ i\hbar \sum_n [\dot{c}_n |\psi_n\rangle + c_n |\dot{\psi}_n\rangle - \frac{i}{\hbar} c_n E_n |\psi_n\rangle] e^{i\theta_n} &= \sum_n c_n E_n |\psi_n\rangle e^{i\theta_n} \Leftrightarrow \\ i\hbar \sum_n \dot{c}_n |\psi_n\rangle &= - \sum_n c_n |\dot{\psi}_n\rangle. \end{aligned} \quad (3.6)$$

Acting with $\langle \psi_m |$ where $m \neq n$ from the left, we get:

$$\begin{aligned} \sum_n \dot{c}_n \delta_{mn} e^{i\theta_n} &= - \sum_n c_n \langle \psi_m | \dot{\psi}_n \rangle e^{i\theta_n} \Leftrightarrow \\ \dot{c}_m &= - \sum_n c_n \langle \psi_m | \dot{\psi}_n \rangle e^{i(\theta_n - \theta_m)}. \end{aligned} \quad (3.7)$$

In order to compute the bra-ket term on the right hand side of Eq. 3.7, we consider the time derivative of the Schrödinger equation

$$\begin{aligned} \dot{H} |\psi_n\rangle + H |\dot{\psi}_n\rangle &= \dot{E}_n |\psi_n\rangle + E_n |\dot{\psi}_n\rangle \Leftrightarrow \\ \langle \psi_m | \dot{H} |\psi_n\rangle + \langle \psi_m | H |\dot{\psi}_n\rangle &= \dot{E}_n \langle \psi_m | \psi_n \rangle + E_n \langle \psi_m | \dot{\psi}_n \rangle \Leftrightarrow \\ (E_n - E_m) \langle \psi_m | \dot{\psi}_n \rangle &= \langle \psi_m | \dot{H} |\psi_n\rangle \Leftrightarrow \\ \langle \psi_m | \dot{\psi}_n \rangle &= \frac{\langle \psi_m | \dot{H} |\psi_n\rangle}{E_n - E_m}. \end{aligned} \quad (3.8)$$

Hence Eq. 3.7 becomes:

$$\dot{c}_m = -c_m \langle \psi_m | \dot{\psi}_m \rangle - \sum_{n \neq m} c_n \frac{\langle \psi_m | \dot{H} |\psi_n\rangle}{E_n - E_m} e^{-\frac{i}{\hbar} \int_0^t [E_n(t') - E_m(t')] dt'}. \quad (3.9)$$

In the adiabatic approximation \dot{H} is by definition small therefore the second term is dropped, leading to:

$$\dot{c}_m = -c_m \langle \psi_m | \dot{\psi}_m \rangle. \quad (3.10)$$

Eq. 3.10 can be written as:

$$\frac{dc_m}{c_m} = - \langle \psi_m | \dot{\psi}_m \rangle dt \rightarrow \ln c_m = - \int_0^t \langle \psi_m(t') | \frac{\partial}{\partial t'} \psi_m(t') \rangle dt' + C, \quad (3.11)$$

leading to:

$$c_m(t) = c_m(0) e^{i\gamma_m(t)}, \quad (3.12)$$

where

$$\gamma_m(t) = i \int_t^t \langle \psi_m(t') | \frac{\partial}{\partial t'} \psi_m(t') \rangle dt'. \quad (3.13)$$

The full time solution is thus:

$$|\Psi(t)\rangle = e^{i\theta_m(t)} e^{i\gamma_m(t)} |\psi_m(t)\rangle, \quad (3.14)$$

with γ_m being the geometric phase factor. If we consider a parameter $\lambda(t)$ in the Hamiltonian that varies very slowly with time, then using the chain rule $\frac{\partial |\psi_n\rangle}{\partial t} = \frac{\partial |\psi_n\rangle}{\partial \lambda} \frac{d\lambda}{dt}$ we can rewrite the geometric phase as:

$$\gamma_m(t) = i \int_0^t \langle \psi_n | \frac{\partial \psi_n}{\partial \lambda} \rangle \frac{d\lambda}{dt'} dt' = i \int_{\lambda_i}^{\lambda_f} \langle \psi_n | \frac{\partial \psi_n}{\partial \lambda} \rangle \quad (3.15)$$

which is zero if $\lambda_i = \lambda_f$. For multiple parameters $\boldsymbol{\lambda} = (\lambda_1, \dots, \lambda_N)$, using the chain rule $\frac{\partial \psi_n}{\partial t} = \frac{\partial \psi_n}{\partial \lambda_1} \frac{d\lambda_1}{dt} + \dots + \frac{\partial \psi_n}{\partial \lambda_N} \frac{d\lambda_N}{dt}$, we can define the geometric phase as:

$$\gamma_n(t) = i \int_{\lambda_i}^{\lambda_f} \langle \psi_n | \nabla_{\boldsymbol{\lambda}} \psi_n \rangle \cdot d\boldsymbol{\lambda}. \quad (3.16)$$

If $\lambda_i = \lambda_f$, the geometric phase becomes:

$$\phi = i \oint \langle \psi_n | \nabla_{\boldsymbol{\lambda}} \psi_n \rangle \cdot d\boldsymbol{\lambda} = i \oint \mathbf{A}(\boldsymbol{\lambda}) \cdot d\boldsymbol{\lambda}. \quad (3.17)$$

The quantities ϕ and A are called Berry phase and Berry connection respectively and their importance will become clear later. Some articles discussing the adiabatic theorem, the geometric phase and the Berry phase include [227, 12, 199].

3.2. Berry phase

A Berry phase describes the global phase acquired by a complex vector when it is carried around a path in a complex vector space [12]. In order to explain this definition we consider two simple quantum systems, a discrete one and a continuous one.

Discrete system

Let us first consider a closed loop, illustrated in Fig 3.1, where $|u_i\rangle$ correspond to the states at each position along the path with $|u_{12}\rangle = |u_0\rangle$. This condition implies that the initial and final positions are identical and therefore the Berry phase is defined in a path (loop), the importance of which will become clear later. Since a complex number z can be written as $z = |r|e^{i\phi}$, with r and ϕ representing its magnitude and its phase respectively, solving for the phase ϕ , we get $\phi = \text{Im} \ln(z)$. This formula is particularly useful since it helps us express the phase as a function of the states $|u_i\rangle$ of the quantum system, giving

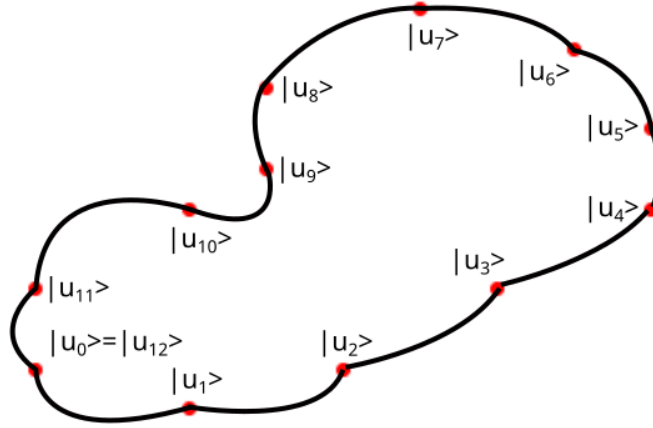


Figure 3.1.: Evolution of a quantum system along a closed trajectory in parameter space

$$\phi = -\text{Im} \ln[\langle u_0|u_1\rangle \langle u_1|u_2\rangle \dots \langle u_{N-1}|u_0\rangle], \quad (3.18)$$

or in a more compact form as:

$$\phi = -\sum_{j=0}^{N-1} \text{Im}[\ln \langle u_j|u_{j+1}\rangle]. \quad (3.19)$$

Since the states $|u_i\rangle$ for a quantum system are not uniquely defined, multiple choices are possible. However, in order for the Berry phase to be a meaningful observable quantity,

it has to be independent of the equivalent selected states. To verify it, we introduce the new states $|\tilde{u}_j\rangle = e^{-i\beta_j} |u_j\rangle$, with β being the gauge transformation. Indeed the Berry phase of Eq. 3.19 remains unchanged because each state appears twice, once in its ket form and once in its bra form, consequently, the exponential parts from the ket and the bra cancel out each other. As a result, the Berry phase is a gauge invariant quantity and hence can be related to physically observable phenomena when it is defined on a closed loop, whereas it is gauge dependent for any open path in the parameter space.

Continuous system

Let us consider a real variable $\lambda \in [0, 1]$ such that $|u_{\lambda=0}\rangle = |u_{\lambda=1}\rangle$ and further that $|u_\lambda\rangle$ is a differentiable function of λ . Under these conditions, the right hand side of Eq. 3.19 reads:

$$\begin{aligned} \ln \langle u_\lambda | u_{\lambda+\delta\lambda} \rangle &= \ln \langle u_\lambda | (|u_\lambda\rangle + d\lambda \partial_\lambda |u_\lambda\rangle + \dots) = \\ &= \ln (1 + d\lambda \langle u_\lambda | \partial_\lambda u_\lambda \rangle + \dots) = \\ &= d\lambda \langle u_\lambda | \partial_\lambda u_\lambda \rangle + \dots, \end{aligned} \quad (3.20)$$

where we only keep first order terms. Substituting Eq. 3.20 to Eq. 3.19, we get the expression of the Berry phase for a closed path (loop) for the continuum limit:

$$\phi = \oint \langle u_\lambda | i \partial_\lambda u_\lambda \rangle d\lambda, \quad (3.21)$$

where, we have taken into account that $\langle u_\lambda | \partial_\lambda u_\lambda \rangle$ is a purely imaginary quantity. The integrand of Eq. 3.21 is known as the Berry connection $A(\lambda)$:

$$A(\lambda) = \langle u_\lambda | i \partial_\lambda u_\lambda \rangle. \quad (3.22)$$

Next, we evaluate the transformation of Berry connection and Berry phase under the gauge $|\tilde{u}_\lambda\rangle = e^{-i\beta(\lambda)} |u_\lambda\rangle$. For the Berry connection, starting from Eq. 3.22, we have

$$\begin{aligned} \tilde{A}(\lambda) &= \langle \tilde{u}_\lambda | i \partial_\lambda \tilde{u}_\lambda \rangle = \\ &= \langle u_\lambda | e^{i\beta(\lambda)} i \partial_\lambda e^{-i\beta(\lambda)} |u_\lambda\rangle = \\ &= \langle u_\lambda | i \partial_\lambda |u_\lambda\rangle + \partial_\lambda \beta(\lambda) = \\ &= A(\lambda) + \partial_\lambda \beta(\lambda), \end{aligned} \quad (3.23)$$

implying that it is gauge-dependent quantity. Regarding the Berry phase, we recall that $|u_{\lambda=0}\rangle = |u_{\lambda=1}\rangle$, which after integration, based on Eq. 3.21, implies:

$$\int_0^1 \frac{\beta(\lambda)}{d\lambda} d\lambda = \beta_{\lambda=1} - \beta_{\lambda=0} = 2\pi m, \quad (3.24)$$

that leads to:

$$\tilde{\phi} = \phi + 2\pi m. \quad (3.25)$$

It is noted that since the Berry phase is a phase angle, it is well defined as modulo 2π , meaning that it is gauge-independent quantity in a closed loop whereas it is gauge-dependent in any open path.

3.3. Berry curvature

As we have seen from Eq. 3.23, the Berry connection is not a gauge invariant quantity and therefore cannot be measured. In order to overtake this obstacle, an alternative quantity, namely the Berry curvature, should be used instead.

Starting from the parameter space, the function λ is denoted as $\boldsymbol{\lambda} = (\lambda_1, \lambda_2, \dots)$ and the Berry connection becomes $\mathbf{A}(\boldsymbol{\lambda}) = (A_1, A_2, \dots)$, with Eq. 3.22 being written as:

$$A_\mu = \langle u_{\boldsymbol{\lambda}} | i\partial_\mu u_{\boldsymbol{\lambda}} \rangle. \quad (3.26)$$

Consequently, the Berry phase of Eq. 3.21 is written as a dot product of the Berry connection and $d\boldsymbol{\lambda}$

$$\phi = \oint \mathbf{A} \cdot d\boldsymbol{\lambda}. \quad (3.27)$$

The Berry curvature $\boldsymbol{\Omega}(\boldsymbol{\lambda})$ is then defined as the Berry phase flux, *i.e.* the Berry phase per unit area in the parameter space, expressed by the curl of the Berry connection in the continuum limit as:

$$\boldsymbol{\Omega} = \nabla \times \mathbf{A}. \quad (3.28)$$

The Berry phase flux is then given by:

$$\phi = \oint (\nabla \times \mathbf{A}) \cdot d\boldsymbol{\lambda}. \quad (3.29)$$

The main motivation of multi-dimensional space generalization was to create a gauge invariant quantity as the integrand. In order to verify this, we apply the gauge transformation $|\tilde{u}_\lambda\rangle = e^{-i\beta(\lambda)} |u_\lambda\rangle$ to the Berry curvature. The multi-dimensional generalization of the gauge transformation of Berry connection of Eq. 3.23 reads:

$$\tilde{\mathbf{A}}(\lambda) = \mathbf{A}(\lambda) + \nabla\beta(\lambda), \quad (3.30)$$

therefore, acting with the curl in both sides, will give the gauge transformation of Berry curvature:

$$\begin{aligned} \nabla \times \tilde{\mathbf{A}}(\lambda) &= \nabla \times (\mathbf{A}(\lambda) + \nabla\beta(\lambda)) = \\ &= \nabla \times \mathbf{A}(\lambda) + \nabla \times \nabla\beta(\lambda) = \\ &= \nabla \times \mathbf{A}(\lambda), \end{aligned} \quad (3.31)$$

where we have taken into account that the curl of a divergence is zero, leading to the conclusion that the Berry curvature is a gauge invariant quantity.

It is noted that for a system evolving in parameter space, the overlap of two infinitesimally close states is called "quantum geometric tensor" and it is given by:

$$\langle \psi_\alpha(\lambda) | \psi_\alpha(\lambda + \delta\lambda) \rangle = \mathcal{F}_\alpha(\lambda) e^{i\phi_\alpha(\lambda)}, \quad (3.32)$$

with \mathcal{F} being the fidelity. In order to be able to draw connections to known quantities, we expand the left hand side of Eq. 3.32:

$$\begin{aligned} \langle \psi_\alpha(\lambda) | \psi_\alpha(\lambda + \delta\lambda) \rangle &= 1 + \sum_i \langle \psi_\alpha(\lambda) | \partial_i \psi_\alpha(\lambda) \rangle d\lambda_i + \\ &+ \frac{1}{2} \sum_{ij} \langle \psi_\alpha(\lambda) | \partial_{ij} \psi_\alpha(\lambda) \rangle d\lambda_i d\lambda_j + \mathcal{O}(d\lambda), \end{aligned} \quad (3.33)$$

which can be written as:

$$\begin{aligned} \mathcal{F}_\alpha^2(\lambda) &= [Re \langle \psi_\alpha(\lambda) | \psi_\alpha(\lambda + d\lambda) \rangle]^2 + [Im \langle \psi_\alpha(\lambda) | \psi_\alpha(\lambda + d\lambda) \rangle]^2 = \\ &= 1 - \sum_{ij} [Re \langle \partial_i \psi_\alpha(\lambda) | \partial_j \psi_\alpha(\lambda) \rangle - \mathbf{A}_{\alpha,i}(\lambda) \mathbf{A}_{\alpha,j}(\lambda)] d\lambda_i d\lambda_j + \mathcal{O}(d\lambda), \end{aligned} \quad (3.34)$$

with $\mathbf{A}_{\alpha,i}$ being the Berry connection. Eq. 3.34 helps us define the quantum metric tensor $g_{\alpha,ij}$:

$$g_{\alpha,ij} = \text{Re} \langle \partial_i \psi_\alpha | \partial_j \psi_\alpha \rangle + \langle \psi_\alpha | \partial_i \psi_\alpha \rangle \langle \psi_\alpha | \partial_j \psi_\alpha \rangle, \quad (3.35)$$

and the Berry curvature $\Omega_{\alpha,ij}$:

$$\Omega_{\alpha,ij} = \partial_i \mathbf{A}_{\alpha,j} - \partial_j \mathbf{A}_{\alpha,i}, \quad (3.36)$$

demonstrating that they are parts of the quantum geometric tensor. Specifically, the metric tensor corresponds to the real part and expresses the distance between the quantum states and the Berry curvature corresponds to the imaginary part.

3.4. Bloch's theorem

So far, we have discussed the notions of Berry phase and Berry curvature in an arbitrary quantum system (arbitrary parameter space). Since we are interested in crystals, from now on we specialize the parameter space to the wavevector components k_j that are labeling the states in the Brillouin zone. Hence, we start from the Bloch's theorem to find the eigenstates (Bloch states) of a system in a periodic potential.

Let's consider a quantum system, described by the Hamiltonian:

$$H = -\frac{\hbar^2}{2m} \nabla^2 + V(\mathbf{r}), \quad (3.37)$$

where the potential, obeying the relation

$$V(\mathbf{r}) = V(\mathbf{r} + \mathbf{R}_n), \quad (3.38)$$

is periodic in respect to the Bravais lattice:

$$\mathbf{R}_n = n_1 \mathbf{a}_1 + n_2 \mathbf{a}_2 + n_3 \mathbf{a}_3. \quad (3.39)$$

The solution of the Schrödinger equation:

$$H\psi_{\mathbf{k}}(\mathbf{r}) = E(\mathbf{k})\psi_{\mathbf{k}}(\mathbf{r}), \quad (3.40)$$

with H being the Hamiltonian of Eq. 3.37, can be written as:

$$\psi_{\mathbf{k}}(\mathbf{r}) = e^{i\mathbf{k}\cdot\mathbf{r}} u_{\mathbf{k}}(\mathbf{r}), \quad (3.41)$$

with $u_{\mathbf{k}}(\mathbf{r})$ being a periodic function with the same periodicity as the lattice:

$$u_{\mathbf{k}}(\mathbf{r}) = u_{\mathbf{k}}(\mathbf{r} + \mathbf{R}_n). \quad (3.42)$$

We distinguish two cases:

- If \mathbf{k} lies within the Brillouin zone, then the wavefunctions take the form $\psi_{\mathbf{k}}(\mathbf{r}) = u_{\mathbf{k}}(\mathbf{r}) e^{i\mathbf{k}_{BZ}\cdot\mathbf{r}}$.
- If \mathbf{k} lies outside the Brillouin zone, then $\mathbf{k} = \mathbf{G} + \mathbf{k}_{BZ}$ and the wavefunctions take the form $\psi_{\mathbf{k}}(\mathbf{r}) = u_{\mathbf{k}}(\mathbf{r}) e^{i\mathbf{G}\cdot\mathbf{r}} e^{i\mathbf{k}_{BZ}\cdot\mathbf{r}}$, with \mathbf{G} being a reciprocal lattice vector.

As a result, the Bloch theorem allows us to write the eigenstates in the form:

$$\psi_{n\mathbf{k}}(\mathbf{r}) = u_{n\mathbf{k}}(\mathbf{r}) e^{i\mathbf{k}\cdot\mathbf{r}}. \quad (3.43)$$

The immediate question that follows up is whether we should express the Berry curvature (and phase) as a function of the Bloch states $\psi_{n\mathbf{k}}(\mathbf{r})$ or of the periodic function $u_{n\mathbf{k}}(\mathbf{r})$. It has been proven that the periodic function $u_{n\mathbf{k}}(\mathbf{r})$ is the only choice because the exponential factor within the definition of the Bloch's theorem causes issues to the evaluation of the integral during the computation of $\langle \psi_{n\mathbf{k}} | \psi_{n,\mathbf{k}+\mathbf{b}} \rangle$. As a result, the Berry phase becomes:

$$\phi_n = \oint \mathbf{A}_n(\mathbf{k}) \cdot d\mathbf{k} = \iint_S \boldsymbol{\Omega} \cdot d\mathbf{S}, \quad (3.44)$$

with n denoting the band index, $\boldsymbol{\Omega}$ the Berry curvature and $\mathbf{A}_n(\mathbf{k})$ being the Berry connection, that reads:

$$\mathbf{A}_n(\mathbf{k}) = i \langle u_{n\mathbf{k}} | \nabla u_{n\mathbf{k}} \rangle. \quad (3.45)$$

Considering that the Berry curvature is given by the curl of the Berry connection, we have:

$$\begin{aligned} \boldsymbol{\Omega} &= \nabla \times \mathbf{A}_n = i \nabla \times \langle u_{n\mathbf{k}} | \nabla u_{n\mathbf{k}} \rangle = \\ &= i \langle \nabla u_{n\mathbf{k}} | \times | \nabla u_{n\mathbf{k}} \rangle + \langle u_{n\mathbf{k}} | \nabla \times | \nabla u_{n\mathbf{k}} \rangle = \\ &= i \langle \nabla u_{n\mathbf{k}} | \times | \nabla u_{n\mathbf{k}} \rangle. \end{aligned} \quad (3.46)$$

Inserting the completeness relation:

$$\sum_m |u_{m\mathbf{k}}\rangle \langle u_{m\mathbf{k}}| = 1, \quad (3.47)$$

into Eq. 3.46, we get:

$$\boldsymbol{\Omega} = \nabla \times \mathbf{A}_n = i \sum_m \langle \nabla u_{n\mathbf{k}} | u_{m\mathbf{k}} \rangle \times \langle u_{m\mathbf{k}} | \nabla u_{n\mathbf{k}} \rangle. \quad (3.48)$$

Since $\langle \nabla u_{n\mathbf{k}} | u_{m\mathbf{k}} \rangle$ is the complex conjugate of $\langle u_{m\mathbf{k}} | \nabla u_{n\mathbf{k}} \rangle$, we only need to simplify the first one. Starting from the Schrödinger equation:

$$H |u_{n\mathbf{k}}\rangle = E_n |u_{n\mathbf{k}}\rangle, \quad (3.49)$$

we apply the spatial gradient to obtain:

$$\begin{aligned} \nabla (H |u_{n\mathbf{k}}\rangle) &= \nabla (E_n |u_{n\mathbf{k}}\rangle) \Leftrightarrow \\ \nabla H |u_{n\mathbf{k}}\rangle + H |\nabla u_{n\mathbf{k}}\rangle &= \nabla E_n |u_{n\mathbf{k}}\rangle + E_n |\nabla u_{n\mathbf{k}}\rangle \Leftrightarrow \\ \langle u_{m\mathbf{k}} | \nabla H |u_{n\mathbf{k}}\rangle + \langle u_{m\mathbf{k}} | H |\nabla u_{n\mathbf{k}}\rangle &= \langle u_{m\mathbf{k}} | \nabla E_n |u_{n\mathbf{k}}\rangle + \langle u_{n\mathbf{k}} | E_n |\nabla u_{n\mathbf{k}}\rangle \Leftrightarrow \\ \langle u_{m\mathbf{k}} | \nabla H |u_{n\mathbf{k}}\rangle + \langle u_{m\mathbf{k}} | H |\nabla u_{n\mathbf{k}}\rangle &= \nabla E_n \delta_{mn} + E_n \langle u_{n\mathbf{k}} | \nabla u_{n\mathbf{k}}\rangle \Leftrightarrow \\ \langle u_{m\mathbf{k}} | \nabla H |u_{n\mathbf{k}}\rangle + E_m \langle u_{m\mathbf{k}} | \nabla u_{n\mathbf{k}}\rangle &= \nabla E_n \delta_{mn} + E_n \langle u_{n\mathbf{k}} | \nabla u_{n\mathbf{k}}\rangle, \end{aligned}$$

where in the last step, we used $\langle u_{m\mathbf{k}} | H |\nabla u_{n\mathbf{k}}\rangle = \langle u_{m\mathbf{k}} | E_m |\nabla u_{n\mathbf{k}}\rangle = E_m \langle u_{m\mathbf{k}} | \nabla u_{n\mathbf{k}}\rangle$. For $m \neq n$, we obtain:

$$\langle u_{m\mathbf{k}} | \nabla u_{n\mathbf{k}}\rangle = \frac{\langle u_{m\mathbf{k}} | \nabla H |u_{n\mathbf{k}}\rangle}{E_n - E_m}. \quad (3.50)$$

So the final expression for the Berry curvature, using Eq. 3.48, is:

$$\Omega = Im \sum_{m \neq n} \frac{\langle u_{n\mathbf{k}} | \nabla H |u_{m\mathbf{k}}\rangle \times \langle u_{m\mathbf{k}} | \nabla H |u_{n\mathbf{k}}\rangle}{(E_n - E_m)^2}. \quad (3.51)$$

An important observation is that the Berry phase of Eq. 3.44 and the Berry curvature of Eq. 3.51 do not depend on the gradient of the state ∇n , making them unrelated to the choice of the states n and m .

3.5. Wannier functions

The most widely used selection of orbitals in study of crystals is the Bloch states that describe the electronic ground state of a set of one-particle orbitals within the independent particle approximation of a periodic system. Wannier functions that were discovered a long time ago [223, 91, 30] are the Fourier transforms of the Bloch wavefunctions, over the whole Brillouin zone and further constitute an alternative to the Bloch states. They are mathematically defined by:

$$|w_0(\mathbf{r})\rangle = \frac{V}{(2\pi)^3} \int_{BZ} |\psi_{\mathbf{k}}(\mathbf{r})\rangle d^3k, \quad (3.52)$$

with V denoting the volume of the cell. Since the function $e^{i\mathbf{k}\cdot\mathbf{r}}$ (that appears in the definition of Bloch's theorem) has different forms at each k , the constructed Wannier functions obtained by superposing Bloch orbitals at different k points are localized. Eq. 3.52 is very restrictive since it only defines the Wannier functions at the original unit cell. A more general definition that includes the translational operator follows:

$$|w_{\mathbf{R}}(\mathbf{r})\rangle = \frac{V}{(2\pi)^3} \int_{BZ} e^{-i\mathbf{k}\cdot\mathbf{R}} |\psi_{\mathbf{k}}(\mathbf{r})\rangle d^3k, \quad (3.53)$$

with \mathbf{R} being the lattice vector. Using the Bloch's theorem $|\psi_{\mathbf{k}}(\mathbf{r})\rangle = e^{i\mathbf{k}\cdot\mathbf{r}} u_{\mathbf{k}}(\mathbf{r})$, we can prove that the Wannier function of different unit cells are identical copies of each other. Namely, the wannier function at a lattice vector $\mathbf{R} + \mathbf{R}'$ is equal to the wannier function at a lattice vector \mathbf{R} :

$$\begin{aligned} |w_{\mathbf{R}+\mathbf{R}'}(\mathbf{r})\rangle &= \int u_{\mathbf{k}}(\mathbf{r}) e^{-i\mathbf{k}(\mathbf{R}+\mathbf{R}')} e^{i\mathbf{k}\cdot\mathbf{r}} d^3k = \\ &= \int u_{\mathbf{k}}(\mathbf{r} - \mathbf{R}') e^{i\mathbf{k}[(\mathbf{r}-\mathbf{R}')-\mathbf{R}]} d^3k = \\ &= |w_{\mathbf{R}}(\mathbf{r} - \mathbf{R}')\rangle, \end{aligned} \quad (3.54)$$

demonstrating their periodic nature.

It is noted that Eq. 3.52 and Eq. 3.53 are valid for a single isolated band (a band that does not become degenerate at any k point). Additionally, they can be used for a group of bands that are degenerate among themselves but isolated with the rest, called composite bands. In this case, an index n , denoting the band, has to be included in the Wannier function and the Bloch wave function.

It is well known that despite the fact that Wannier functions form a good replacement of the Bloch wave functions, their choice is not unique. To overcome this obstacle, for a system with composite bands, we transform the Bloch states according to the formula:

$$|u_{n\mathbf{k}}(\mathbf{r})\rangle = \sum_m U_{mn}^{(k)} |u_{m\mathbf{k}}(\mathbf{r})\rangle, \quad (3.55)$$

with $U_{mn}^{(k)}$ being an arbitrary unitary rotations that mixes the bands for every point in k -space. Then, the Wannier functions of Eq. 3.53 are defined as:

$$|w_{n\mathbf{R}}(\mathbf{r})\rangle = \int_{BZ} \sum_m U_{mn}^{(k)} |\psi_{m\mathbf{k}}(\mathbf{r})\rangle e^{-i\mathbf{k}\cdot\mathbf{R}} d^3k. \quad (3.56)$$

The simplest choice for the unitary rotation matrix is a diagonal matrix consisting of phase ϕ that acts on each band n , such as $e^{i\phi_n(k)}$. It happens that this selection breaks the localized character of the Wannier functions and therefore it is not a good choice. We can instead find another (non-diagonal) form of $U_{mn}^{(k)}$ matrix to minimize the sum of the quadratic spreads of the Wannier probability distributions $|w_n(\mathbf{r})|^2$, the so-called maximally localized Wannier functions. In such a way the problem becomes a minimization problem of the spread functional Ω , given by:

$$\Omega = \sum_n [\langle w_{n0}(\mathbf{r}) | r^2 | w_{n0}(\mathbf{r}) \rangle - \langle w_{n0}(\mathbf{r}) | r | w_{n0}(\mathbf{r}) \rangle^2]. \quad (3.57)$$

The choice of maximally localized Wannier functions resolves the uniqueness problem of the Wannier functions [126, 193]. It is noted that there are still three trivial degrees of freedom left that are unimportant [125]. The technical procedure of obtaining the maximally localized wannier functions is described in Ref [133].

3.6. Weyl points and nodal lines

Topological metals are materials with nontrivial band topology and are further classified in certain classes based on their band structures. Below, we briefly investigate the most important classes based on general Hamiltonians.

We start by considering the following four-band low-energy Hamiltonian [21]:

$$H_{3D} = u\tau_x(\boldsymbol{\sigma} \cdot \mathbf{k}) + m\tau_z + b\sigma_z + b'\tau_z\sigma_x = \begin{bmatrix} m\mathbf{1} + b\sigma_z + b'\sigma_x & u\boldsymbol{\sigma} \cdot \mathbf{k} \\ u\boldsymbol{\sigma} \cdot \mathbf{k} & -m\mathbf{1} + b\sigma_z - b'\sigma_x \end{bmatrix}, \quad (3.58)$$

with u being the velocity parameter, $\mathbf{1}$ the 2×2 identity matrix, $\mathbf{k} = (k_x, k_y, k_z)$ the momentum vector, $\boldsymbol{\sigma} = (\sigma_x, \sigma_y, \sigma_z)$ the Pauli matrices for the spin and $\boldsymbol{\tau} = (\tau_x, \tau_y, \tau_z)$ the Pauli matrices for the pseudospin. Finally, m denotes the mass parameter, b and b' the Zeeman fields (viewed as magnetic fields parallel to z and x axes respectively) that break time-reversal symmetry (T). It is noted that the Hamiltonian of Eq. 3.58 is a decomposed version of a full Dirac Hamiltonian based on γ matrices that requires two Zeeman fields according to [21]. The Hamiltonian matrix can alternatively be written as a 4×4 matrix, the general analytical diagonalization of which is not possible due to the parameters involved. For this reason, we consider the following cases [1, 93]:

- $b' = 0$

The diagonalization of the Hamiltonian matrix results in the following energy spectrum:

$$E(\mathbf{k}) = \pm \sqrt{m^2 + b^2 + u^2 \mathbf{k}^2 \pm 2b \sqrt{u^2 k_z^2 + m^2}}. \quad (3.59)$$

The parameters m and b significantly affect the outcome, therefore, the following cases are noted:

- $m = b = 0$

In this case, the energy dispersion becomes:

$$E(\mathbf{k}) = \pm u^2 \mathbf{k}^2 = \pm (u_x^2 k_x^2 + u_y^2 k_y^2 + u_z^2 k_z^2), \quad (3.60)$$

which corresponds to a degenerate band touching at point $(k_x, k_y, k_z) = (0, 0, 0)$, dubbed Dirac point, as illustrated in Fig. 3.2(a). Materials with such kind of dispersion are called Dirac semimetals. It is emphasized that the simultaneous presence of vanishing b and b' implies the presence of T , forcing Dirac semimetals to be nonmagnetic. Many Dirac semimetals have been predicted and/or confirmed including Na_3Bi [221, 113], Cd_3As_2 [222, 141, 14].

- $|m| > |b|$

In this case, a gap is created between the inner bands, as illustrated in Fig. 3.2(b) and the materials with such dispersion are called semiconductors.

- $|m| < |b|$

In this case, the two inner bands are touching at two points with coordinates $(k_x, k_y, k_z) = (0, 0, \pm \frac{\sqrt{b^2 - m^2}}{u})$, creating, unlike the first case, non-degenerate nodes, called Weyl nodes, as illustrated in Fig. 3.2(c). Materials with such dispersion are called Weyl semimetals and it is further noted that Weyl nodes always appear in pairs. The first materials that were proposed to realize a magnetic Weyl semimetal phase were the pyrochlore iridates $\text{R}_2\text{Ir}_2\text{O}_7$ (R=yttrium or lanthanide element) [218].

- $m = b = 0, b' \neq 0$

In this case, the energy dispersion becomes:

$$E(\mathbf{k}) = \pm \sqrt{u^2 k_x^2 + \left(u \sqrt{k_y^2 + k_z^2} \pm b' \right)^2}. \quad (3.61)$$

Interestingly, the two inner bands touch along a circle, given by the equation $k_y^2 + k_z^2 = \frac{b^2}{u^2}$ at the plane $k_x = 0$, as illustrated in Fig. 3.2(d). The touching points are non-degenerate and materials with such dispersion are called nodal line semimetals. Many materials with such dispersion have been predicted and/or confirmed some of which include Cu_3PdN [86, 236], Ca_3P_2 [229, 26] and CaAgX with $X=(\text{P,As})$ [231].

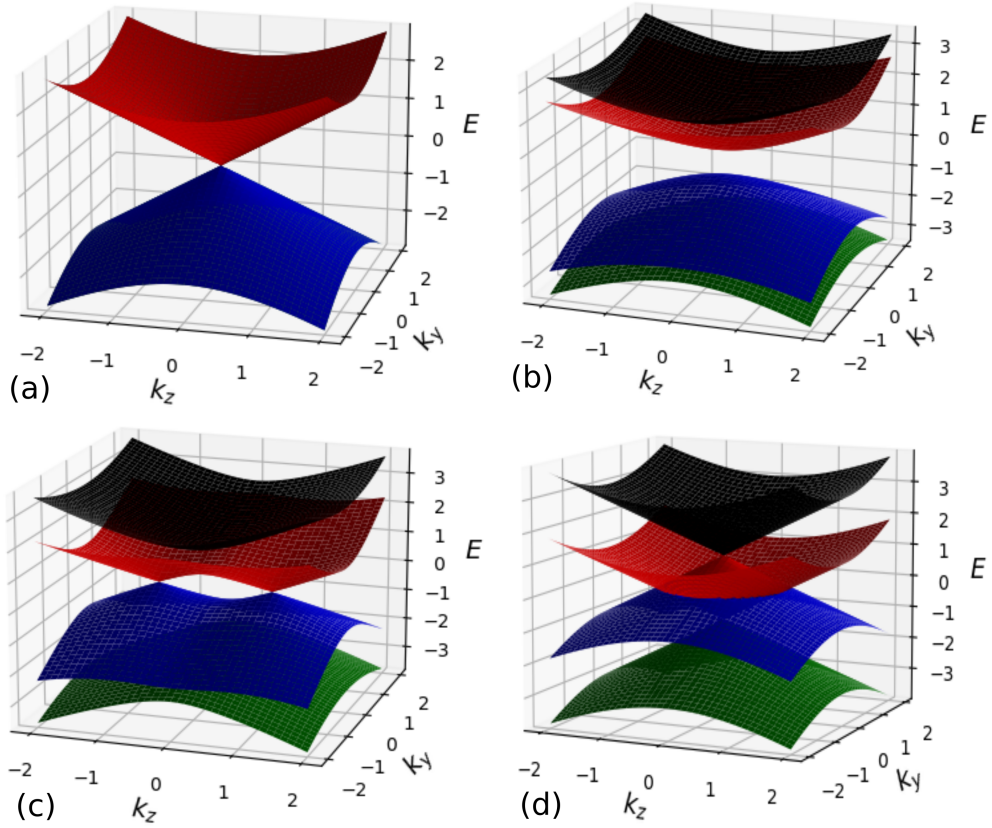


Figure 3.2.: Classes of topological materials (a) Dirac semimetal (b) Semiconductor (c) Weyl semimetal (d) Nodal semimetal. All figures are at $k_x = 0$.

In general, inversion symmetry (P) and time reversal symmetry (T) determine the presence of Weyl semimetal phase. Specifically, at least one has to be broken. If T is broken (magnetic system), the simplest case is realized, in which a pair of Weyl nodes of opposite chirality is sufficient. On the other hand, if P is broken, the presence of T

does not change the chirality of the symmetry equivalent Weyl node [135], therefore two additional Weyl nodes of opposite chirality are required to make the net chirality vanish, giving rise to (at least) four Weyl nodes in total [57]. Lastly, Weyl semimetal phase is also realized when both P and T are broken [251]. It is further noted that the change of a topological phase is possible when a pair of Weyl nodes associated with opposite chirality are combined in the same spatial position. The presence of both P and T leads to the Dirac semimetal phase [113, 141].

3.6.1. Topological protection

After briefly discussing the Dirac nodes and the Weyl nodes, we focus on their stability upon applying perturbations on the Hamiltonian of the system, which will reveal their nature and we demonstrate that unlike Dirac nodes, Weyl nodes are robust in perturbation and hence have a topological nature.

Weyl nodes

Starting with the Weyl nodes, we consider a simple two-band model in 2D and 3D k-space, given by the Hamiltonians:

$$\begin{aligned} H_{2D}(\mathbf{k}) &= u(k_x\sigma_x + k_y\sigma_y) = \begin{bmatrix} 0 & (k_x + ik_y) \\ u(k_x - ik_y) & 0 \end{bmatrix} \\ H_{3D}(\mathbf{k}) &= u(k_x\sigma_x + k_y\sigma_y + k_z\sigma_z) = \begin{bmatrix} uk_z & u(k_x + ik_y) \\ u(k_x - ik_y) & -uk_z \end{bmatrix}, \end{aligned} \quad (3.62)$$

where u is a constant and $\sigma_x, \sigma_y, \sigma_z$ the Pauli matrices. The eigenvalues of these Hamiltonians are given by:

$$\begin{aligned} E_{2D} &= \pm u\sqrt{k_x^2 + k_y^2} \\ E_{3D} &= \pm u\sqrt{k_x^2 + k_y^2 + k_z^2}. \end{aligned} \quad (3.63)$$

Weyl nodes, being the solutions of $\Delta E_{2D,3D} = 0$ with ΔE expressing the difference between the energies of the two bands, are obtained at $(k_x, k_y) = (0, 0)$ and $(k_x, k_y, k_z) = (0, 0, 0)$ for the 2D and 3D case respectively.

The nature of the Weyl nodes in materials depends on the dimensions of the k-space. In order to elucidate this behavior, we add a small mass term $m\sigma_z$ as a perturbation to the Hamiltonians 3.62, in order to obtain:

$$\begin{aligned}
H_{2D}^{per} &= u(k_x\sigma_x + k_y\sigma_y) + m\sigma_z = \begin{bmatrix} m & u(k_x + ik_y) \\ (k_x - ik_y) & -m \end{bmatrix} \\
H_{3D}^{per} &= u(k_x\sigma_x + k_y\sigma_y + k_z\sigma_z) + m\sigma_z = \begin{bmatrix} uk_z + m & (k_x + ik_y) \\ u(k_x - ik_y) & uk_z - m \end{bmatrix},
\end{aligned} \tag{3.64}$$

where the ‘‘per’’ superscript denotes the perturbed Hamiltonians. The obtained eigenvalues are given by:

$$\begin{aligned}
E_{2D}^{per} &= \pm\sqrt{u^2k_x^2 + u^2k_y^2 + m^2} \\
E_{3D}^{per} &= \pm u\sqrt{k_x^2 + k_y^2 + \left(k_z + \frac{m}{u}\right)^2}.
\end{aligned} \tag{3.65}$$

It is noted that in the 2D case, there is no real solution to the equation $\Delta E_{2D}^{per} = 0$, therefore no Weyl nodes are possible, however, in the 3D case, the \mathbf{k} -point $(k_x, k_y, k_z) = (0, 0, -\frac{m}{u})$ is the solution of $\Delta E_{3D}^{per} = 0$. As a consequence, the perturbation term applied to the Hamiltonian destroyed the Weyl node by opening the gap in 2D case, whereas it displaced the spatial position of the Weyl node in the 3D case, demonstrating that the Weyl nodes are robust against perturbations and hence they are topologically protected, having topological nature.

Dirac nodes

Regarding the Dirac nodes, we consider the following Hamiltonian:

$$H(\mathbf{k}) = k_x\Gamma_1 + k_y\Gamma_2 + k_z\Gamma_3, \tag{3.66}$$

where $\Gamma_{i=1,2,3}$ are 4×4 matrices obeying $\Gamma^2 = I$ and $\Gamma_i\Gamma_j = -\Gamma_j\Gamma_i$ (for $i \neq j$). The energy spectrum is given by:

$$E(\mathbf{k}) = \pm\sqrt{k_x^2 + k_y^2 + k_z^2}, \tag{3.67}$$

where, we can observe the existence of a degenerate Dirac node at $(k_x, k_y, k_z) = (0, 0, 0)$. After adding a mass perturbation of the form $m\Gamma_4$ to the Hamiltonian, we get the perturbed Hamiltonian that reads:

$$H^{per}(\mathbf{k}) = k_x\Gamma_1 + k_y\Gamma_2 + k_z\Gamma_3 + m\Gamma_4, \tag{3.68}$$

which leads to the following energy dispersion:

$$E^{per}(\mathbf{k}) = \pm \sqrt{k_x^2 + k_y^2 + k_z^2 + m^2}. \quad (3.69)$$

We notice that after applying the perturbation, the energy gap has opened, proving that the Dirac nodes are not robust against perturbations.

3.6.2. Types of Weyl nodes

Until recently it was believed that the Weyl nodes were similar to the ones depicted in Fig. 3.3(a), having a point-like Fermi surface, as illustrated in Fig. 3.3(c). It was later found that if the Weyl nodes are tilted enough (see Fig. 3.3(b)), they have electron-hole pockets Fermi surface, as the one illustrated in Fig. 3.3(d). The former type is called type-I, whereas the latter type-II. The first type-II Weyl semimetal predicted was WTe_2 in Ref [191] and the authors present the following dispersion relation:

$$E(\mathbf{k}) = Ak_x + Bk_y \pm \sqrt{e^2k_z^2 + (ak_x + ck_y)^2 + (bk_x + dk_y)^2}, \quad (3.70)$$

where A, B, a, b, c, d and e being constants.

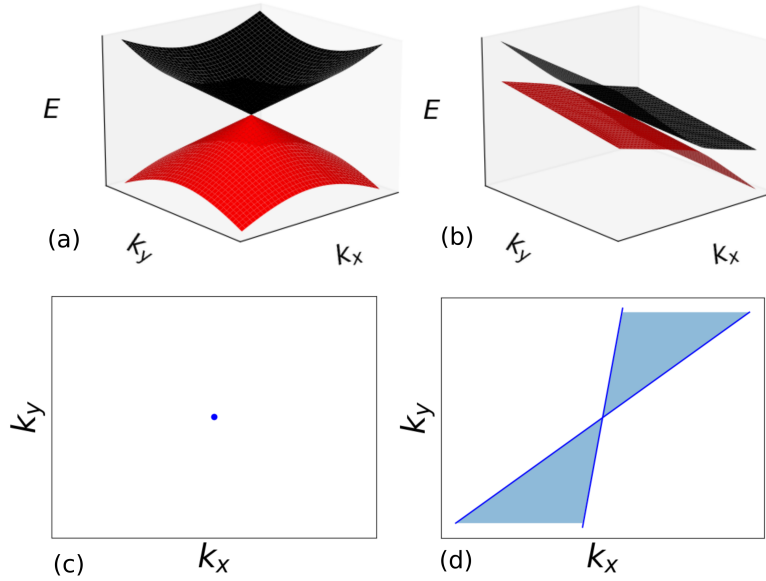


Figure 3.3.: Type-I Weyl point (a) and type-II Weyl point (b) with their respective Fermi surfaces (c) and (d)

3.6.3. Connection to Berry curvature

The eigenfunctions of a Hamiltonian describing a Weyl semimetal are given by:

$$u_{\pm}(\mathbf{k}) = \begin{pmatrix} \sqrt{\frac{k_{\pm}k_z}{2k}} e^{-i\frac{\delta}{2}} \\ \pm \sqrt{\frac{k_{\mp}k_z}{2k}} e^{i\frac{\delta}{2}} \end{pmatrix}, \quad (3.71)$$

with $\delta = \arctan\left(\frac{k_y}{k_x}\right)$. As we have already discussed, Eq. 3.51 describes the Berry curvature of a system consisting of many bands. The equivalent expression for a Weyl system with only 2 bands (denoted by "+" and "-") reads:

$$\Omega_{\pm}(\mathbf{k}) = \text{Im} \frac{\langle u_{\pm}(\mathbf{k}) | \nabla H(\mathbf{k}) | u_{\mp}(\mathbf{k}) \rangle \times \langle u_{\mp}(\mathbf{k}) | \nabla H(\mathbf{k}) | u_{\pm}(\mathbf{k}) \rangle}{(E_{+}(\mathbf{k}) - E_{-}(\mathbf{k}))^2}. \quad (3.72)$$

After performing the calculations, we end up with:

$$\Omega_{\pm}(\mathbf{k}) = \mp \frac{1}{2} \frac{\mathbf{k}}{k^3}. \quad (3.73)$$

Since Eq 3.73 is equivalent to that of a Dirac magnetic monopole, with the magnetic field being replaced by the Berry curvature, Weyl nodes can be viewed as sinks or sources of Berry curvature in momentum space.

3.6.4. Chern number

A topological charge that corresponds to the Chern number can be defined. This Chern number, being the integral of the Berry curvature flux over any closed 2-dimensional manifold, is quantized to be 2π times integer and can be mathematically expressed by:

$$C = \frac{1}{2\pi} \iint_S \boldsymbol{\Omega} \cdot d\mathbf{S}, \quad (3.74)$$

where the integration is performed in the surface S .

The Chern number, being the exchange of Berry curvature between two bands is zero in gapped states and nonzero for gapless states like Weyl nodes. In order to show that the nonvanishing Chern number is originating from the Weyl node, we insert the Berry curvature of Eq. 3.73, obtained for the Weyl node, to the definition of Chern number in Eq. 3.74 and after performing the integration, we find $C = 1$.

Since the topological charge must be zero in the whole Brillouin zone due to the fermion doubling problem [142, 143, 144], Weyl points are only allowed to be in pairs of opposite chirality. A sketch of opposite chirality Weyl points is illustrated in Fig. 3.4.

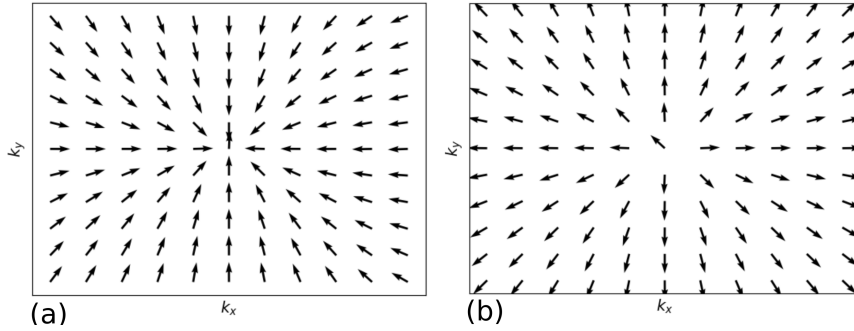


Figure 3.4.: Weyl points of opposite chirality

In general the treatment of the Berry formalism has a lot of similarities with electromagnetism with the most important equivalencies being summarized in Tab. 3.1.

Table 3.1.: Equivalent quantities in Berry formalism and electrodynamics.

Berry formalism		Electrodynamics
Berry connection		Vector potential
$A(k) = \langle u_{nk} i \nabla_k u_{nk} \rangle$	\leftrightarrow	$A(r)$
Berry curvature		Magnetic field
$\Omega(k)$	\leftrightarrow	$B(r)$
Berry phase		Aharonov-Bohm phase
$\oint_{\mathcal{C}} A(k) dk = \iint dS \Omega(k)$	\leftrightarrow	$\oint_{\mathcal{C}} A(r) dr = \iint dS B(r)$
Chern number		Dirac monopole
$\frac{1}{2\pi} \iint dS \Omega(k) = \text{integer}$	\leftrightarrow	$\iint dS B(r) = \text{integer} \frac{\hbar}{e}$

3.7. Charge and spin currents

Before proceeding to the Hall effects, a short discussion of spin and charge currents is essential. Since both charge and spin are fundamental properties of electrons, the notions of charge and spin currents take place in transport properties. We consider a material with equal number of spin-up and spin-down electrons. In case both electron's spin channels move towards the same direction, a charge current J_c is observed, antiparallel to the direction of the motion, since the electrons are negatively charged particles. This current is alternatively called pure charge current (see Fig. 3.5(a)). In case the spin-up and spin-down electrons move towards opposite directions, the charge current is zero, however,

the spin imbalance between the two sides of the conductor gives rise to a spin current J_s , the pure spin current (see Fig. 3.5(c)).

A natural question is whether charge and spin currents can simultaneously be present. In order to answer to this question, we consider a ferromagnetic material in which there is an imbalance of spin-up and spin-down electrons. When the electrons, irrespective of their spin channel, move towards the same direction, then a charge current, due to the motion of electrons and a spin current due to the imbalance of spin-up and spin-down electrons are observed. The combined currents are dubbed spin polarized charge current (see Fig. 3.5(b)).

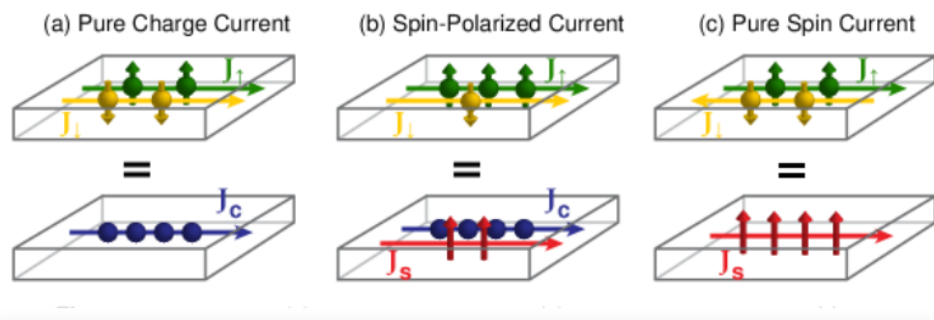


Figure 3.5.: Different types of current: (a) Pure charge current, $j_c \neq 0$, $j_s = 0$ (b) Spin-polarized current $j_c \neq 0$, $j_s \neq 0$ (c) Pure spin current $j_c = 0$, $j_s \neq 0$.
Source: [Czeschka, Franz Dominik. "Spin currents in metallic nanostructures" (2011)]

Mathematically, the current \mathbf{J} (either spin or charge) is given by Ohm's law

$$\mathbf{J} = \boldsymbol{\sigma}\mathbf{E}, \quad (3.75)$$

with \mathbf{E} being the applied electric field and $\boldsymbol{\sigma}$ the conductivity tensor which is a matrix:

$$\boldsymbol{\sigma} = \begin{pmatrix} \sigma_{xx} & \sigma_{xy} & \sigma_{xz} \\ \sigma_{yx} & \sigma_{yy} & \sigma_{yz} \\ \sigma_{zx} & \sigma_{zy} & \sigma_{zz} \end{pmatrix}. \quad (3.76)$$

An alternative notation used is: $\sigma_{xy} = \sigma_z$, $\sigma_{xz} = \sigma_y$ and $\sigma_{yz} = \sigma_x$.

3.8. Anomalous Hall effect

In 1879, Edwin Hall discovered that, due to the Lorentz force in the presence of an external magnetic field, electrons are pushed towards the one side of a current-carrying conductor, generating a transverse current, dubbed (ordinary) Hall effect [60], as illustrated in Fig. 3.7(a). Later, he discovered that this effect is ten times larger in ferromagnetic iron than in non-magnetic conductors [61]. This result was explained by the simultaneous presence of the already discovered (ordinary) Hall effect, alongside an additional contribution, dubbed “anomalous Hall effect” and the following empirical relation was later introduced to describe the resistivity that governs the effect:

$$\rho_{xy} = R_0 H_z + R_s M_z, \quad (3.77)$$

with R_0 , R_s and H_z being an independent of material constant, a material dependent constant and the magnetic field respectively.

Interestingly, the Hall resistivities of magnetic and non-magnetic materials, exhibit a drastically discrepant behavior, as shown in Fig. 3.6. On the one hand, in non magnetic conductors the Hall resistivity increases linearly with the applied magnetic field, as expected from the Lorentz force. On the other hand, for magnetic conductors, a steep increase is observed for small magnetic fields, followed by an almost constant value regardless of the magnetic field for large values of magnetic field.

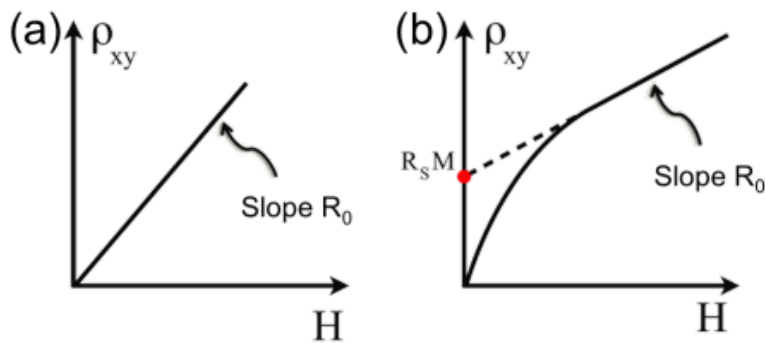


Figure 3.6.: (a) Ordinary Hall effect (b) Anomalous Hall effect. Source: [arXiv:1508.02967]

The anomalous Hall effect [136], being the transverse Hall voltage obtained by the transverse velocity electrons acquire can be understood by considering a ferromagnet, in which there is an imbalance of spin-up and spin-down electrons. In this ferromagnet,

the application of an electric field creates a potential difference that forces electrons to move parallel to the direction of the electric field, generating a longitudinal current. In addition to this, a transverse spin polarized charge current (charge current and spin current) is observed, as illustrated in Fig. 3.7(b), originating from spin orbit coupling mechanisms where the role of the external magnetic field is played by the Berry curvature. In other words, the anomalous Hall effect can be viewed as the generation of a transverse spin-polarized current in response to an applied longitudinal electric field.

The spin orbit coupling dependent mechanisms leading to the transverse generation of the spin polarized charge current are classified in two categories, namely intrinsic and extrinsic. On the one hand, the intrinsic contribution is only dependent on the Berry curvature [84, 136]. On the other hand, the extrinsic are further divided in skew scattering and side jump contributions. One can think of the skew scattering as an effective field gradient that causes force towards or away from the scattering plane, depending on the spin direction and the side-jump as an effective displacement due to spin dependent acceleration and deceleration. Further analysis of the extrinsic contributions is outside of the scopes of this work and the interested reader can find more information in the following literature [136, 190, 11]. From now on, with the term anomalous Hall conductivity, we exclusively refer to the intrinsic part.

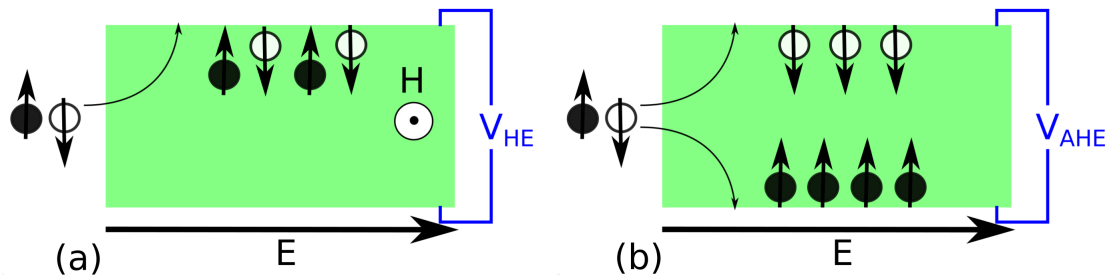


Figure 3.7.: Illustration of (a) Ordinary Hall effect (b) anomalous Hall effect

From all the above discussion it becomes clear that the role of spin orbit coupling is critical in the mechanisms generating the anomalous Hall effect. One can argue though that an additional mechanism that is not dependent on spin orbit coupling, may give rise to finite Hall effect in ferromagnets having topologically nontrivial spin texture, such as skyrmions and pyrochlore ferromagnet with geometrically frustrated lattice structure. This effect is solely originating from Berry phase acquired by an electron moving in a smoothly varying magnetization and has been dubbed “topological Hall effect” [20] and has been reported, among others, in MnSi [140, 108], MnGe [82], FeGe [237, 72].

The intrinsic contribution to the anomalous Hall conductivity is given by:

$$\sigma_{ij}^{int} = e^2 \hbar \sum_{n \neq m} \int \frac{d\mathbf{k}}{(2\pi)^3} [f(\epsilon_n(\mathbf{k})) - f(\epsilon_m(\mathbf{k}))] \text{Im} \frac{\langle u_{n\mathbf{k}} | v_i(\mathbf{k}) | u_{m\mathbf{k}} \rangle \langle u_{m\mathbf{k}} | v_j(\mathbf{k}) | u_{n\mathbf{k}} \rangle}{[\epsilon_n(\mathbf{k}) - \epsilon_m(\mathbf{k})]^2}, \quad (3.78)$$

with u , f and ϵ being the state, the Fermi-Dirac distribution and the energy band of occupied (n) and empty (m) states respectively and v the anomalous velocity given by:

$$v(\mathbf{k}) = \frac{1}{\hbar} \nabla_{\mathbf{k}} H(\mathbf{k}). \quad (3.79)$$

What makes Eq. 3.78 special is its connection to the topological properties of Bloch states [80, 148] and more specifically proportional to the integration of the Berry curvature over the Fermi sea [59, 220], expressed by:

$$\langle u_{n\mathbf{k}} | \nabla_{\mathbf{k}} | u_{m\mathbf{k}} \rangle = \frac{\langle u_{n\mathbf{k}} | \nabla_{\mathbf{k}} H(\mathbf{k}) | u_{m\mathbf{k}} \rangle}{\epsilon_m(\mathbf{k}) - \epsilon_n(\mathbf{k})}. \quad (3.80)$$

Combining Eq. 3.78, Eq. 3.79 and Eq. 3.80, we extract the final expression used for our calculations that reads:

$$\begin{aligned} \sigma_{ij} &= -\epsilon_{ijl} \frac{e^2}{\hbar} \sum_n \int \frac{d\mathbf{k}}{(2\pi)^d} f(\epsilon_n(\mathbf{k})) \Omega_n^l(\mathbf{k}) \\ \Omega_n(\mathbf{k}) &= \nabla_{\mathbf{k}} \times \mathbf{A}_n(\mathbf{k}) \\ \mathbf{A}_n(\mathbf{k}) &= i \langle u_{n\mathbf{k}} | \nabla_{\mathbf{k}} | u_{n\mathbf{k}} \rangle, \end{aligned} \quad (3.81)$$

where $\Omega(\mathbf{k})$ and $\mathbf{A}_n(\mathbf{k})$ being the Berry curvature and the Berry connection defined in Eq. 3.28 and Eq. 3.45 respectively, demonstrating the topological nature of the anomalous Hall effect. Since the units of Berry curvature in three dimensions are “length²”, we extract that the anomalous Hall conductivity is given in units of $\Omega^{-1} \text{cm}^{-1} = S/\text{cm}$.

Since the anomalous Hall effect is linked to ferromagnetic materials, the term “spontaneous Hall effect” is used in some articles to describe the transverse current obtained from the transverse velocity that electrons acquire in the absence of external magnetic fields in ferromagnetic and antiferromagnetic materials.

3.9. Anomalous Nernst effect

In complete analogy to the anomalous Hall effect, its thermoelectric counterpart, the anomalous Nernst effect [139, 228], being the generation of a transverse spin-polarized

current in response to an applied thermal gradient, as illustrated in Fig. 3.8 can be defined [172]:

$$\alpha_{ij} = \frac{1}{e} \int d\epsilon \frac{\partial f}{\partial \mu} \sigma_{ij}(\epsilon) \frac{\epsilon - \mu}{T}, \quad (3.82)$$

with σ_{ij} , e , f , μ and T being the anomalous Hall conductivity at $T = 0$, the electron charge, the Fermi-Dirac distribution function, the chemical potential and the temperature respectively. At low temperatures, the above relation reduces to Mott relation:

$$\alpha_{ij}(\epsilon) = \frac{\pi^2 k_B^2 T}{3e} \sigma'_{ij}(\epsilon_F), \quad (3.83)$$

with k_B , ϵ_F and σ' being the Boltzmann's constant, the Fermi energy and derivative of the anomalous Hall conductivity with respect to the energy respectively.

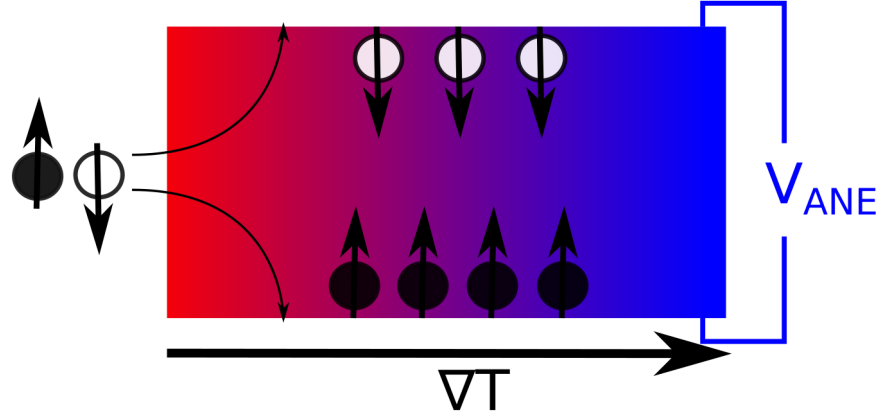


Figure 3.8.: Illustration of Anomalous Nernst effect

3.10. Computational techniques

Having discussed about the nature of the anomalous Hall and Nernst effects and their dependence on the Weyl nodes, nodal lines and avoided crossing sections, we are ready to deal with their computational challenges. As we have seen, the anomalous Hall conductivity is dependent on the Berry curvature, which is given by $\Omega_n(\mathbf{k}) = \nabla_{\mathbf{k}} \times \mathbf{A}_n(\mathbf{k})$, that can be written as a second-rank antisymmetric tensor as:

$$\begin{aligned}\Omega_{n,\gamma}(\mathbf{k}) &= \epsilon_{\alpha\beta\gamma}\Omega_{n,\alpha\beta}(\mathbf{k}) \\ \Omega_{n,\alpha\beta}(\mathbf{k}) &= -2Im \left\langle \frac{\partial u_{n\mathbf{k}}}{\partial k_\alpha} \middle| \frac{\partial u_{n\mathbf{k}}}{\partial k_\beta} \right\rangle,\end{aligned}\tag{3.84}$$

with $\epsilon_{\alpha\beta\gamma}$ being the Levi-Civita tensor. Recently, following the increased demand for accurate, fast and large scale calculations, several codes, written in different programming languages, that can compute the anomalous Hall conductivity were released, with the most famous being “Wannier90” [133], “Wanniertools” [226] and “Wannierberri” [207]. In the following we briefly discuss two of the most famous methodologies of evaluating Berry curvature, namely Kubo formula and Wannier interpolation.

Kubo formula

The simplest way to evaluate Berry curvature is to directly use Eq. 3.84. The presence of the derivatives in k-space however poses some difficulties which are circumvented by replacing the derivatives by sums over states [104, 205], getting the so-called Kubo formula:

$$\begin{aligned}\Omega_{n,\alpha\beta}(\mathbf{k}) &= -2Im \sum_{m \neq n} \frac{u_{nm,\alpha}(\mathbf{k}) u_{mn,\beta}(\mathbf{k})}{[\omega_m(\mathbf{k}) - \omega_n(\mathbf{k})]^2} \\ \omega_n(\mathbf{k}) &= \frac{\epsilon_{n\mathbf{k}}}{\hbar} \\ u_{nm,\alpha}(\mathbf{k}) &= \frac{1}{\hbar} \langle u_{n\mathbf{k}} | \frac{\partial H(\mathbf{k})}{\partial k_\alpha} | u_{m\mathbf{k}} \rangle.\end{aligned}\tag{3.85}$$

Due to the fact that the Berry curvature is enhanced at the vicinity of Weyl nodes, nodal lines and avoided crossing areas, monopole behavior is expected close to these areas. As a consequence, a high number of computationally expensive ab-initio calculations to evaluate the Berry curvature on a dense grid is required to guarantee convergence. Despite the tremendous computational effort required, the anomalous Hall conductivity of $\text{Fe}_x\text{Ni}_{1-x}\text{Pd}$, bcc Fe and SrRuO_3 have been calculated by Lowitzer et al. [116], Yao et al. [235] and Fang et al. [35] respectively.

Wannier interpolation

Since the computational effort of the Kubo formula method is enormous, an alternative technique that allows faster calculations is desired. The method relies on Wannier functions, discussed in a previous sections, and it is called Wannier interpolation. In this section, we

shall discuss the method in the anomalous hall conductivity context, even though its use is more extended.

The idea of Wannier interpolation is to obtain the Berry curvature (hence anomalous Hall conductivity) on a dense k grid using Wannier functions, based on first-principles calculations of energy and wavefunctions on a coarse grid q . Since the Wannier functions are defined as the Fourier transform of the Bloch states, based on Eq. 3.53, we can obtain the Bloch states, in the Wannier gauge, by using the inverse Fourier transform:

$$|\psi_{n\mathbf{k}}^{(W)}\rangle = \sum_{\mathbf{R}} e^{-i\mathbf{k}\cdot(\mathbf{r}-\mathbf{R})} |w_{n\mathbf{R}}\rangle, \quad (3.86)$$

where the superscript W corresponds to the Wannier gauge. The form of Eq. 3.86 is the same as the tight binding Bloch formula, demonstrating that the Wannier functions can play the role of atomic orbitals in the tight-binding theory. The Hamiltonian matrix elements of the Bloch states are then obtained by:

$$H_{nm}^{(W)}(\mathbf{k}) = \sum_{\mathbf{R}} e^{i\mathbf{k}\cdot\mathbf{R}} \langle w_{n0} | H | w_{m\mathbf{R}} \rangle, \quad (3.87)$$

which are diagonalized by:

$$[U^\dagger(\mathbf{k}) H^{(W)}(\mathbf{k}) U(\mathbf{k})]_{nm} = \epsilon_{n\mathbf{k}} \delta_{nm}, \quad (3.88)$$

where U is a rotation matrix, to obtain the energy eigenvalues. A graphical illustration of the procedure is provided in Fig. 3.9.

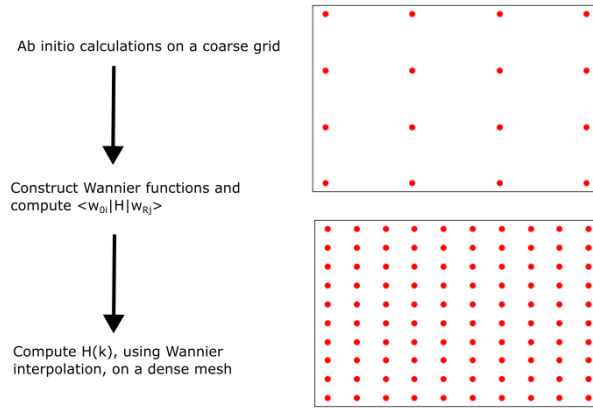


Figure 3.9.: Wannier interpolation technique

The wannier interpolated Bloch eigenstates are represented by rotating the Bloch states with the same matrix that diagonalized the Hamiltonian, according to:

$$|\psi_n\rangle = \sum_j |\psi_j^{(W)}\rangle U_{jn}. \quad (3.89)$$

Expressing the Berry curvature in terms of the Bloch functions, we obtain:

$$\mathbf{\Omega}_n = -Im \langle \nabla_{\mathbf{k}} u_n | \times | \nabla_{\mathbf{k}} u_n \rangle. \quad (3.90)$$

The ingredient needed to compute the Berry curvature is the k-derivative of the Bloch wavefunction that can be written as:

$$|\nabla_{\mathbf{k}} u_n\rangle = \sum_m |u_m\rangle \mathbf{D}_{mn} + \sum_j |\nabla_{\mathbf{k}} u_j^{(W)}\rangle U_{jn}, \quad (3.91)$$

with \mathbf{D} matrix being equal to:

$$\mathbf{D}_{nm} = \frac{[U^\dagger (\nabla_{\mathbf{k}} H^{(W)}) U]_{nm}}{\epsilon_m - \epsilon_n}. \quad (3.92)$$

Combining Eq. 3.90 and Eq. 3.91 allows us to express the Berry curvature in terms of \mathbf{D} matrix, which is indeed the interpolated Berry curvature. More detailed description of the method is found in Refs [219, 115].

3.11. Symmetry analysis

An immediate observation is that the anomalous Hall and Nernst conductivities, given by Eq. 3.78 and Eq. 3.82 respectively, explicitly depend on Berry curvature. As a consequence, determining the behavior of Berry curvature in the Brillouin zone will reveal the presence (or absence) of anomalous Hall and Nernst conductivities. Next, we discuss in detail how the Berry curvature transforms under each symmetry operation.

The Berry curvature behaves as a pseudovector under any symmetry operation and its basic spatial and directional transformations are illustrated in Fig. 3.10. Firstly, it is noted that the length of the pseudovector remains unchanged under the application of any symmetry operation. Unlike its length, the direction depends on the nature of the symmetry operation and it is further discussed below. As shown in Fig. 3.10, the identity (part a) and the spatial inversion (part b) have no impact to the orientation of the Berry curvature pseudovector, while the mirror planes (part c), the rotation axes (part e), the roto-inversions (part f) and the time reversal (part d) operators do have.

In order to elucidate the direction change of the Berry curvature pseudovector under the underlying symmetry operations, we create Fig.3.10(c-e). For a mirror plane, the component of the pseudovector which is parallel to the plane is flipped, whereas the perpendicular component remains unchanged (see part c). As for the rotation axis, it rotates in such a way that the vector always remains tangential to the circular plane with normal the rotation axis (see part e). Finally, in order to visualize the impact of the time reversal symmetry, we associate a current to each pseudovector flowing circularly on the plane that has normal the pseudovector, with its direction being determined by the right hand rule, as illustrated in part d. Therefore, the time reversal operator flips the direction of the current and hence the direction of the pseudovector. As it becomes clear though, time reversal is never by itself a symmetry of any magnetic system.

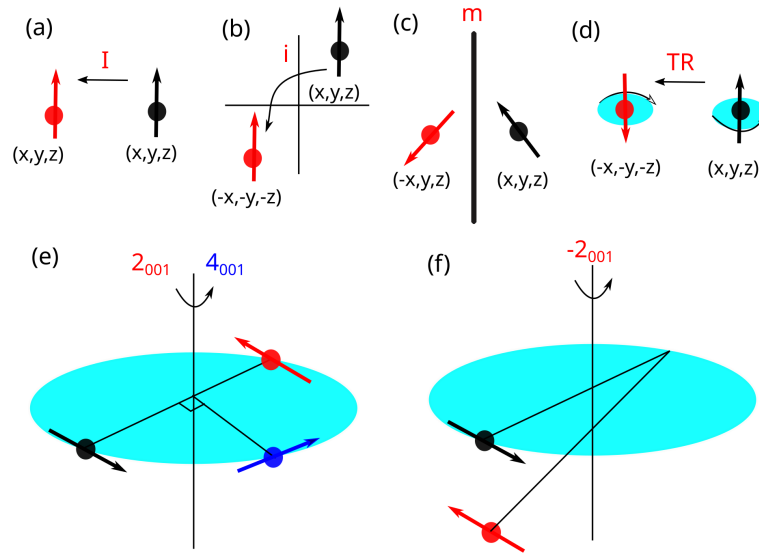


Figure 3.10.: Spatial and directional transformation of pseudovectors (arrows) under the application of identity (a) inversion (b) mirror plane (c) time reversal (d) rotation (e) and roto-inversion (f) operators. Black arrows correspond to the initial spatial positions whereas red (or blue) to the final positions of the respective symmetry operator

In general, it is possible, using the linear response theory presented in Ref. [180], to express mathematically the transformations of the Berry curvature pseudovector for an arbitrary symmetry operation. Considering the Berry curvature as a pseudovector with

coordinates $\boldsymbol{\Omega} = (\Omega_x, \Omega_y, \Omega_z)$, each symmetry operation will transform it based on the formula:

$$s\boldsymbol{\Omega}(\mathbf{r}) = \det(\mathbf{D}(\mathbf{R})) \mathbf{D}(\mathbf{R}) \boldsymbol{\Omega}(s^{-1}\mathbf{r}), \quad (3.93)$$

with $\boldsymbol{\Omega}$ being the Berry curvature, \mathbf{D} denoting the three-dimensional matrix representation of a symmetry operation without the translation part and s an arbitrary symmetry operation. Tab. 3.2 presents the most common symmetry operations, their three-dimensional matrix representations and the resulting Berry curvature transformations. Since the magnetic Laue group of a compound governs its reciprocal lattice symmetries, the shape of the anomalous Hall and Nernst conductivities tensors will be determined by the symmetries of the magnetic Laue group.

A quick look at the Berry curvature transformations of Tab. 3.2 reveals the first obvious condition of vanishing anomalous Hall effect. Since the Berry curvature under the application of T (time reversal symmetry) transforms according to $\Omega_n(\mathbf{k}) = -\Omega_n(-\mathbf{k})$, it is obvious that the resulting anomalous Hall effect must vanish. This observation is understood from the fact that the anomalous Hall conductivity is proportional to the sum of Berry curvature in the whole Brillouin zone hence summing up $\Omega_n(\mathbf{k})$ with $-\Omega_n(\mathbf{k})$ gives rise to the vanishing result.

Another condition that forces Berry curvature to be zero is the combination of P and T . In this case the Berry curvature is transformed under the application of the P according to $\Omega_n(\mathbf{k}) = \Omega_n(-\mathbf{k})$. Hence, it becomes clear that for a system that preserves PT (both inversion and time reversal), the Berry curvature must obey $\Omega_n(-\mathbf{k}) = -\Omega_n(-\mathbf{k})$. This condition is valid only if $\Omega_n(-\mathbf{k}) = 0$ hence the Berry curvature is forced to vanish, giving rise to zero anomalous Hall conductivity.

Table 3.2.: Transformation of the Berry curvature pseudovector under the application of the most common symmetry operations. 1 (unity operator), $P = -1$ (spatial inversion), 2_{001} (2-fold rotation axis along z-direction), m_{001} (mirror plane with normal parallel to z-direction), -4_{001}^+ (4-fold counter clockwise rotoinversion along z-direction), $T = 1'$ (time reversal)

Number	Symmetry	Matrix Representation	Berry Curvature
1	1	$\begin{pmatrix} 1 & 0 & 0 \\ 0 & 1 & 0 \\ 0 & 0 & 1 \end{pmatrix}$	$\Omega_x(k_x, k_y, k_z) = \Omega_x(k_x, k_y, k_z)$ $\Omega_y(k_x, k_y, k_z) = \Omega_y(k_x, k_y, k_z)$ $\Omega_z(k_x, k_y, k_z) = \Omega_z(k_x, k_y, k_z)$
2	-1	$\begin{pmatrix} -1 & 0 & 0 \\ 0 & -1 & 0 \\ 0 & 0 & -1 \end{pmatrix}$	$\Omega_x(-k_x, -k_y, -k_z) = \Omega_x(k_x, k_y, k_z)$ $\Omega_y(-k_x, -k_y, -k_z) = \Omega_y(k_x, k_y, k_z)$ $\Omega_z(-k_x, -k_y, -k_z) = \Omega_z(k_x, k_y, k_z)$
3	2_{001}	$\begin{pmatrix} -1 & 0 & 0 \\ 0 & -1 & 0 \\ 0 & 0 & 1 \end{pmatrix}$	$\Omega_x(-k_x, -k_y, k_z) = -\Omega_x(k_x, k_y, k_z)$ $\Omega_y(-k_x, -k_y, k_z) = -\Omega_y(k_x, k_y, k_z)$ $\Omega_z(-k_x, -k_y, k_z) = \Omega_z(k_x, k_y, k_z)$
4	m_{001}	$\begin{pmatrix} 1 & 0 & 0 \\ 0 & 1 & 0 \\ 0 & 0 & -1 \end{pmatrix}$	$\Omega_x(k_x, k_y, -k_z) = -\Omega_x(k_x, k_y, k_z)$ $\Omega_y(k_x, k_y, -k_z) = -\Omega_y(k_x, k_y, k_z)$ $\Omega_z(k_x, k_y, -k_z) = \Omega_z(k_x, k_y, k_z)$
5	-4_{001}^+	$\begin{pmatrix} 0 & 1 & 0 \\ -1 & 0 & 0 \\ 0 & 0 & -1 \end{pmatrix}$	$\Omega_x(k_y, -k_x, -k_z) = \Omega_y(k_x, k_y, k_z)$ $\Omega_y(k_y, -k_x, -k_z) = \Omega_x(k_x, k_y, k_z)$ $\Omega_z(k_y, -k_x, -k_z) = \Omega_z(k_x, k_y, k_z)$
6	$1'$	$\begin{pmatrix} 1 & 0 & 0 \\ 0 & 1 & 0 \\ 0 & 0 & 1 \end{pmatrix}$	$\Omega_x(-k_x, -k_y, -k_z) = -\Omega_x(k_x, k_y, k_z)$ $\Omega_y(-k_x, -k_y, -k_z) = -\Omega_y(k_x, k_y, k_z)$ $\Omega_z(-k_x, -k_y, -k_z) = -\Omega_z(k_x, k_y, k_z)$

So far the role of spin orbit coupling has been of significant importance to the presence of finite anomalous Hall and Nernst conductivities. In an inspiring work by Suzuki et al. [198], it is argued that for a general magnetic structure, the combined $R_S T$ symmetry (effective T-symmetry, combination of spin rotation and time reversal) must be broken in order to observe finite anomalous Hall conductivity. Even though the spin orbit coupling is necessary to break $R_S T$ in coplanar magnetic orientations, it is not required in non-coplanar cases. This result demonstrates the presence of finite anomalous Hall conductivities in certain magnetic structures without spin orbit coupling.

3.12. Materials

The anomalous Hall effect has been theoretically calculated and experimentally measured in many different types of materials. Below we discuss several classes of compounds that anomalous Hall effect was measured or calculated and highlight the most promising compounds.

As previously discussed, the anomalous Hall effect is proportional to the Berry curvature and since it behaves as a pseudovector under any symmetry operation, we can extract that the presence of T by itself or the combined presence of P and T symmetries force its cancellation. As a consequence, in order to realize the anomalous Hall effect besides the presence of magnetic ordering, T and the combined PT symmetries should not be

present.

- Non magnetic materials

Since the anomalous Hall effect is coupled to the magnetic ordering, it becomes clear that nonmagnetic materials do not exhibit anomalous Hall conductivity values. It is noted that anomalous Hall signals have been measured in ZrTe_5 [109] and KV_3Sb_5 [233] that are centrosymmetric nonmagnetic material, however, this non-spontaneous Hall signal requires the application of an external magnetic field hence it does not belong to the same category.

- Magnetic materials

The presence of magnetic ordering breaks T hence non-vanishing anomalous Hall conductivities are in principle allowed in magnetic materials

- Ferromagnets

The largest reported value of roughly 2000 S/cm was calculated for Fe [235] followed by $\text{Co}_3\text{Sn}_2\text{S}_2$ [112, 48]. Finite values have been calculated in many other compounds including HgCr_2Se_4 [232], XPt_3 with $X=(\text{V},\text{Cr},\text{Mn})$ [123], Fe_3GeTe_2 [85], Co_2MnGa [49, 9, 171, 145, 117] and Fe_2MnX with $X=(\text{P}, \text{As}, \text{Sb})$ [147]. Recently though accurate high-throughput techniques allowed large scale calculations, as a result the anomalous Hall conductivity was calculated in several classes of materials such as antiperovskites [184], Fe-based binary ferromagnets [172], itinerant ferromagnets [130] and Heuslers [146, 100, 122] in an attempt to find promising compounds. Regarding the anomalous Nernst conductivity, non-zero values have been calculated for several compounds such as $\text{Co}_3\text{Sn}_2\text{S}_2$ [233], $\text{CuCr}_2\text{Se}_{4-x}\text{Br}_x$ [103], Fe_3O_4 [166], MnSi [69], FePt , Co , Fe [224], Co_2MnGa [168] and many others [64, 130].

- Antiferromagnets

Even though the anomalous Hall effect (and anomalous Nernst effect) was initially linked to the ferromagnets, the symmetry conditions discussed in a previous section do not forbid its presence in antiferromagnets.

- * Collinear

Even though it was originally believed that the anomalous Hall effect cannot appear in collinear antiferromagnets, recent studies demonstrated the presence of the so called “crystal Hall effect” in certain magnetic point groups [189]. Further analysis is outside of the scopes of this work.

- * Non-collinear

Chen et al were the first to calculate finite anomalous Hall conductivity

Table 3.3.: Most notable compounds with large anomalous Hall conductivity

Compound	Magnetic ordering	AHC (S/cm)	Reference
Rh ₂ MnGa	Collinear ferromagnet	-1862	[146]
Rh ₂ MnAl	Collinear ferromagnet	-1723	[146]
Co ₂ MnAl	Collinear ferromagnet	-1631	[146]
Co ₂ VSn	Collinear ferromagnet	-1489	[100]
Co ₃ Sn ₂ S ₂	Collinear ferromagnet	1130	[112, 48]
Mn ₃ PtN	Non-collinear antiferromagnet	799	[74]
Mn ₃ GeN	Non-collinear antiferromagnet	-624	[74]
Mn ₃ IrN	Non-collinear antiferromagnet	-575	[74]
Mn ₃ Ge	Non-collinear antiferromagnet	-298	[242]
Mn ₃ Rh	Non-collinear antiferromagnet	-284	[242]

Table 3.4.: Most notable compounds with large anomalous Nernst conductivity

Compound	Magnetic ordering	ANC (A/mK)	Reference
Co ₃ PtN	Collinear ferromagnet	6.27	[184]
Co ₂ MnGa	Collinear ferromagnet	-5.00	[146]
Ru ₂ FeP	Collinear ferromagnet	-4.23	[146]
Ru ₂ FeAs	Collinear ferromagnet	-4.07	[146]
Fe ₂ MnSb	Collinear ferromagnet	-4.00	[146]
YbMnBi ₂	Non-collinear antiferromagnet	10.0	[152]
Mn ₃ NiN	Non-collinear antiferromagnet	2.00	[248]
Mn ₃ Sn	Non-collinear antiferromagnet	-1.16	[51]
Mn ₃ Ge	Non-collinear antiferromagnet	-1.18	[51]

in Mn₃Ir [27] and after this achievement many others compounds have followed, including the rest of the members of the Mn₃X family with X=(Sn, Ge, Ga, Rh, Pt) [195, 101, 138, 51, 87, 242], the Mn₃XN family with (X=Ag, Au, Co, Ga, Hg, In, Ir, Ni, Pd, Pt, Rh, Zn) [74, 186, 13, 54, 248, 249, 137], and the Cr₃XN family with X=(Ir, Pt, Rh) [186]. The anomalous Hall conductivity was also in calculated in isolated compounds including Mn₅Si₃ [197, 196], Pr₂Ir₂O₇ [120, 211], and Nd₂Mo₂O₇ [200]. Regarding the anomalous Nernst conductivity, the obtained values for Mn₃X family [76, 107, 51, 51] are in principle smaller than their ferromagnetic counterparts, however very recently, a giant value has been reported for YbMnBi₂ [152].

The most notable anomalous Hall and Nernst conductivity values are presented in Tab. 3.3 and Tab. 3.4 respectively. It is noted that further details related to the magnetic structure and the temperature the Nernst conductivity was calculated can be found within the corresponding literature.

3.13. Applications

Conventional thermoelectric devices are based on the Seebeck effect (see Fig. 3.11(a)) which is the generation of a longitudinal electric current in response to an applied longitu-

dinal thermal gradient. In reality, two (semi-)conductors (one of type n and one of type p) with different Seebeck coefficients are electrically connected, as shown in Fig. 3.11(b) [46], and a thermal gradient is applied from the one side of the thermocouple. The electron flow from the n to the p type (semi-)conductor generates the electric Seebeck current. Since the generated current from one pillar is small, the Seebeck module in real applications consists of multiple thermocouples that are connected in series to increase the Seebeck voltage, as shown in Fig. 3.11(c). The longitudinal nature of the Seebeck effect however requires thick and high enough conductors, imposing limitations to the construction of the module since it increases the size of the device along the thermal gradient direction and hampers its flexibility and durability.

An alternative module, utilizing the anomalous Nernst effect instead, can be constructed as illustrated in Fig. 3.11(d). The main advantage originates from the transverse geometry of the anomalous Nernst effect that allows to enlarge the thermoelectric output by elongating the total length of the wire, without increasing the height along the thermal gradient direction [131, 174]. As a consequence, more durable and flexible generators are possible. A particular example of utilizing anomalous Nernst effect module features is the construction of a coil-shaped generator [234] and of a flexible heat flux sensor [246]. Despite the remarkable progress in search of materials with large anomalous Nernst conductivities, the current record at room temperature is smaller than 10 A/mK , rendering the newly proposed module to have 1-2 orders of magnitude smaller thermopower than the conventional Seebeck module [210]. Therefore novel approaches of using this module in combination with searching new materials with even large anomalous Nernst values could in principle be beneficial for future thermoelectric applications.

Since applications of transverse thermoelectric generation require a thermopower of at least $20 \mu\text{V/K}$ [173], an attempt to increase the thermopower by proposing a new module named Seebeck-driven transverse thermoelectric generation (STTG) [247] has been proposed. In short, a thermoelectric (TE) and a ferromagnetic (FM) material are electrically connected and a thermal gradient is applied, as illustrated in Fig. 3.11(e). As we have already discussed the presence of the thermal gradient generates a longitudinal Seebeck current in the TE material that in turns generates a transverse anomalous Hall current, due to the anomalous Hall effect, when passing through the FM material. The effective thermopower of this module is larger than the one of anomalous Nernst effect module and suggests that materials with large values of anomalous Hall conductivities are useful for thermoelectric conversion [210, 127].

Since the use of thermoelectric modules provide green energy technology without production of hazardous for the environment wastes and contain no moving parts, they are used in several applications, some notable of which include, portable camping stoves, jet engines, pavements, oil and gas pipelines, space exploration and automobile [52, 65,

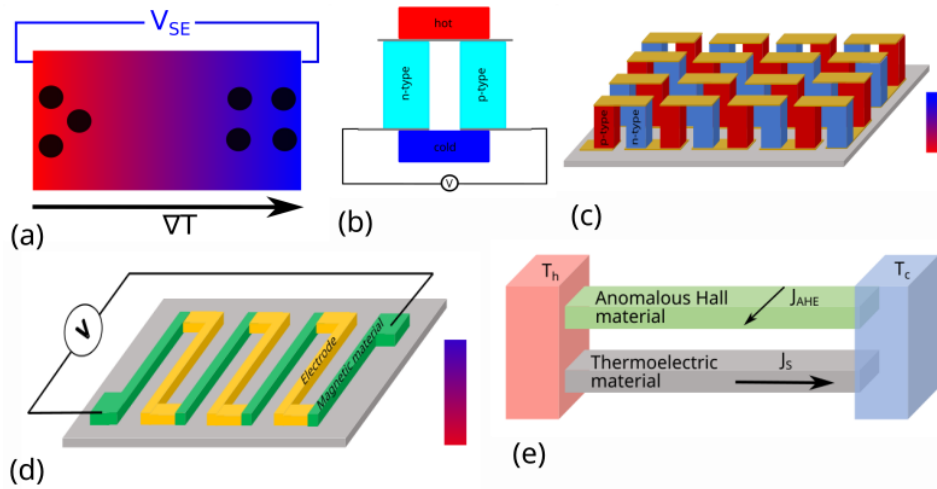


Figure 3.11.: (a) Schematic illustration of Seebeck effect (b) Seebeck thermopile (c) Seebeck thermoelectric module (d) Anomalous Nernst thermoelectric module (e) Seebeck-driven transverse thermoelectric generation (STTG)

241, 25]. Despite the advantages of the new modules, the current figure of merit is still low [209] compared to the conventional one and therefore more research to the field is required.

4. Topological properties of non-collinear antiferromagnets

The term Perovskites includes all ceramics with the generalized formula M_3AB with M denoting non metallic anions whereas A and B atoms being metallic cations. Reversing the positions of anions with that of cations in the arrangement leads to the antiperovskite structure that is illustrated in Fig. 4.1. Both perovskites and antiperovskite have cubic crystal structures belonging to the $Pm\bar{3}m$ (221) space group. Antiperovskite materials have attracted attention due to their interesting properties and applications including superconductivity [149, 225], negative thermal expansion [202, 53, 71], magnetostriction [182], barocaloric [181], thermoelectric [110], solid state batteries [245] among others. For instance, the first oxygen-free superconductor is the antiperovskite Ni_3MgC [66]. Manganese based antiperovskites form an interesting subclass of magnetic antiperovskites with interesting properties [206] such as piezomagnetism [239] and magnetostriction [185] and magnetoresistance [81]. Additionally they offer a great variety of magnetic configurations and transitions [40] that motivated me to investigate the tunability of their transport properties.

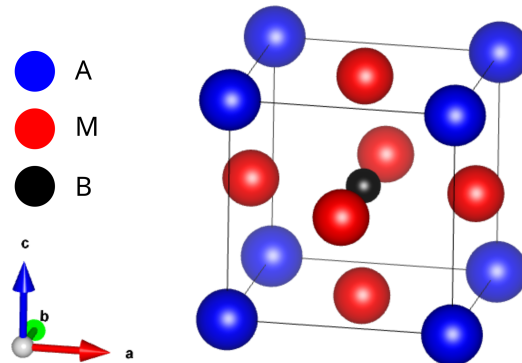


Figure 4.1.: Antiperovskite structure

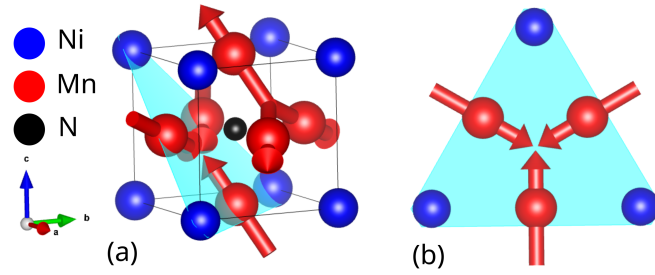


Figure 4.2.: (a) Γ_{4g} magnetic configuration of Mn_3NiN (b) View from (111)-plane

In this chapter, the anomalous Hall and Nernst conductivities of the non-collinear antiferromagnetic antiperovskites Mn_3NiN and Mn_3GaN are calculated and their dependence on applied biaxial strain and magnetization direction rotations is investigated. A complete methodology of obtaining the shape of the anomalous Hall/Nernst conductivity tensors based on the symmetries of the magnetic point group of the compound is provided. My results further demonstrate that the Weyl nodes and nodal lines located in the proximity of the Fermi energy significantly contribute to the calculated anomalous Hall and Nernst conductivities and they can be further tuned by means of external stimuli in order to further enhance their topological properties. The current chapter is based on Ref. [175] and Ref. [13].

4.1. Magnetic configurations

Mn_3NiN

The magnetic ground state configuration of Mn_3NiN is found to be of Γ_{4g} -type. Explicit DFT calculations reveal a smaller than Mn_3GaN magnetocrystalline anisotropy energy with the Γ_{4g} state lying 0.15meV below the Γ_{5g} , in agreement with literature [186]. The magnetic moments in the Γ_{4g} state exclusively originate from Mn atoms and lie on the (111)-plane (see Fig. 4.2(a)), facing towards the N atom (see Fig. 4.2(b)). The small magnetocrystalline anisotropy energy allows easy rotation of the magnetic moments on the (111)-plane.

Mn_3GaN

In contrast to the Γ_{4g} -type non-collinear antiperovskite Mn_3NiN , the ground state of Mn_3GaN is of Γ_{5g} -type. In this magnetic configuration the magnetic moments originate exclusively from Mn atoms and lie on the (111)-plane (see Fig. 4.3(a)) facing the adjacent Mn atom (see Fig. 4.3(b)). My results compare the energies of Γ_{5g} , Γ_{4g} , ferromagnetic,

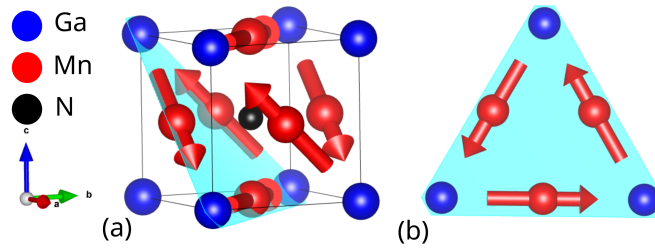


Figure 4.3.: (a) Γ_{5g} magnetic configuration of Mn_3GaN (b) View from (111)-plane

in-(111)-plane rotation and out-of-(111)-plane tilting configurations. It is found that the Γ_{5g} is the ground state being 0.5meV lower than the Γ_{4g} and 0.11eV lower than the ferromagnetic, in agreement with literature [186]. Moreover, it is noticed that the magnetocrystalline anisotropy within the (111)-plane of Mn_3GaN is larger than that of Mn_3NiN , which can be attributed to the larger spin orbit coupling of Ga atoms compared to the spin orbit coupling of Ni atoms. Additionally, it is noted that the energy of in-(111)-plane rotation of the magnetic moments, that follows a typical sinusoidal behaviour, is energetically more favorable than the out of-(111)-plane tilting, as considered for Mn_3Ir [27]. Specifically, an energy lift of 1.1 meV is required for a 2° out of (111)-plane tilt.

4.2. Symmetry analysis

The presence of spin orbit coupling in combination with the symmetry of the magnetic configuration describes the shape of the anomalous Hall conductivity tensor for Mn_3NiN and Mn_3GaN . The dependence of the spin orbit coupling is analyzed first. In an inspiring work by Suzuki et al [198], the role of $R_S T$ symmetry (combination of spin rotation R_S and time reversal T) is discussed. Specifically it is noted that for any magnetic configuration that is invariant under the $R_S T$ symmetry, the anomalous Hall effect is forced to vanish. This happens because the Berry curvature transforms according to $\Omega^a(k_x, k_y, k_z) = -\Omega^a(k_x, k_y, k_z)$ making sum of the Berry curvature zero after integrating over the whole Brillouin zone. The absence of spin orbit coupling does not break $R_S T$ symmetry and forces the topological Hall effect to vanish. My results verify the the validity of the $R_S T$ rule demonstrating zero topological Hall effect for any angle of rotation within the (111)-plane, as shown in Fig. 4.4(b).

The presence of spin orbit coupling breaks the $R_S T$ symmetry therefore further analysis of the symmetries of the underlying system is required. The absence of T and PT are

necessary but not sufficient conditions for finite anomalous Hall conductivity. Since the anomalous Hall conductivity is proportional to the Berry curvature, the symmetry transformations of the latter determined the former. As already discussed, Berry curvature behaves as a pseudovector and transforms under any symmetry operation according to Eq. 3.93. For the Γ_{5g} state with magnetic space group $R\bar{3}m$ (166.97) and corresponding magnetic point group ($\bar{3}m$), the presence of $M_{\bar{1}10}$ mirror plane transforms the Berry curvature according to:

$$\begin{aligned}\Omega_x(k_x, k_y, k_z) &= \Omega_x(-k_y, -k_x, -k_z) \\ \Omega_y(k_x, k_y, k_z) &= \Omega_y(-k_y, -k_x, -k_z) \\ \Omega_z(k_x, k_y, k_z) &= -\Omega_z(-k_y, -k_x, -k_z),\end{aligned}\tag{4.1}$$

leading to vanishing z-component of anomalous Hall conductivity after integrating over the whole Brillouin zone. Similar conditions from the symmetry equivalent planes $M_{\bar{1}01}$ and $M_{01\bar{1}}$ imply the vanishing x and y components. In contrast, for Γ_{4g} and strain-distorted- Γ_{4g} configurations, the magnetic space group changes to $R\bar{3}m'$ (166.101) (magnetic point group $\bar{3}m'$) and $C2'/m'$ (12.62) (magnetic point group $2'/m'$) respectively, there are no symmetries imposing vanishing conditions to the Berry curvature, therefore the anomalous Hall effect is allowed to exhibit finite values. Similarly, for magnetic configurations deviating from Γ_{5g} by a finite angle, the magnetic space group becomes $R\bar{3}$ (148.17) (magnetic point group $\bar{3}$) and there is also no symmetry operation which prohibits finite anomalous Hall conductivity. Finally, for distorted- Γ_{5g} configurations, the magnetic space group changes to $C2/m$ (12.58) (magnetic point group $2/m$) and therefore only the $M_{\bar{1}10}$ remains that forces the z-component to vanish, while leaves x and y unrestricted.

The results based on the symmetry analysis are fully consistent with our numerical values of anomalous Hall conductivity which is further confirmed by explicitly constructed conductivity tensors following Ref. [111] for the magnetic space groups. The form of the anomalous Hall conductivity tensor for all the above mentioned magnetic configurations are shown in Tab. 4.1.

It is noted that the anomalous Hall conductivity tensor depends on the geometry of the measurements. The symmetry analysis of the magnetic point group of the underlying magnetic configurations uses the Cartesian basis $a||[100]$, $b||[010]$ and $c||[001]$. However, a change of the basis will affect the vanishing conditions hence extra care is required.

Table 4.1.: Anomalous Hall conductivity tensor for different magnetic configurations. The symbols as well as the numbers of the magnetic space groups correspond to the Belov-Neronova-Smirnova (BNS) settings

Magnetic configuration	Magnetic space group	Anomalous Hall conductivity tensor		
Γ_{5g}	$R\bar{3}m$ (166.97)	0	0	0
Γ_{4g}	$R\bar{3}m'$ (166.101)	0	σ_{xy}	$-\sigma_{xy}$
$\theta \neq 0, 90$	$R\bar{3}$ (148.17)	$-\sigma_{xy}$	0	σ_{xy}
Distorted Γ_{5g}	$C2/m$ (12.58)	σ_{xy}	$-\sigma_{xy}$	0
Distorted Γ_{4g}	$C2'/m'$ (12.62)	0	0	$-\sigma_{zx}$
		0	0	$-\sigma_{zx}$
		σ_{zx}	σ_{zx}	0
		0	σ_{xy}	$-\sigma_{zx}$
		$-\sigma_{xy}$	0	σ_{zx}
		σ_{zx}	$-\sigma_{zx}$	0

4.3. Magnetization induced anomalous Hall/Nernst conductivities

The possibility of tuning the anomalous Hall and Nernst conductivities by rotating the magnetization direction on the (111)-plane, as shown in Fig. 4.4(a), is investigated. Despite the small energy difference between the Γ_{5g} and the Γ_{4g} magnetic states, the behaviour of the corresponding anomalous Hall conductivity is very distinct. Fig. 4.4(b) shows the calculated anomalous Hall conductivity for several angles of rotation θ , starting from the Γ_{5g} state that corresponds to $\theta = 0$. First of all, it is noted that all components of the anomalous Hall conductivity ($\sigma_{x/y/z}$) exhibit a sinusoidal behaviour with a maximum absolute value of $62S/cm$ that corresponds to the Γ_{4g} state. Additionally, the magnitude of the absolute value of the anomalous Hall conductivity is symmetric in respect to the $x = 180$ line, meaning that configurations that correspond to angles having the same distance from $\theta = 180^\circ$ (for example $\theta = 150^\circ$ and $\theta = 210^\circ$) are forced to exhibit the same absolute value anomalous Hall effect, regulated by symmetry, according to: $\sigma(\mathbf{M}) = -\sigma(-\mathbf{M})$. My results verify that increasing the absolute value of the anomalous Hall conductivity from 0 to $62S/cm$ by means of in plane rotation of the magnetic moments is possible in Mn_3GaN , similar results are obtained for Mn_3Ir [27].

Similarly to the anomalous Hall, the anomalous Nernst coefficient is also tunable by rotating the magnetization direction. Since the anomalous Nernst coefficient is expressed as the energy derivative of the anomalous Hall conductivity $\frac{d\sigma_i}{d\epsilon}$, based on Mott relation [2], it is straightforward to calculate it for several magnetization directions. It is observed that the magnitude of the anomalous Nernst coefficient follows a sinusoidal behaviour, being

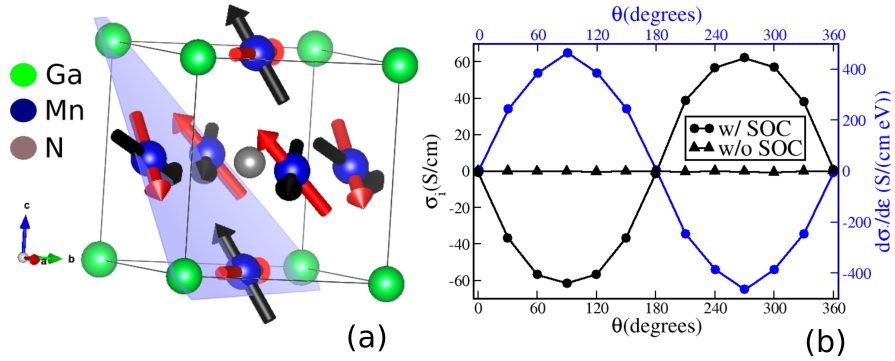


Figure 4.4.: Mn₃GaN: (a) Crystal structure and magnetic configurations for in-plane rotation of Mn magnetic moments. Red arrows correspond to angle $\theta = 0$, whereas black to $\theta = 90$. (b) Anomalous Hall conductivity and its energy derivative for different in-plane rotation angles θ of Mn magnetic moments

zero at Γ_{5g} state ($\theta = 0$) and exhibiting its maximum value of $\approx -500 \frac{S}{cm \cdot eV}$ at the Γ_{4g} state, as illustrated in Fig. 4.4(b). The maximum value of $\approx -500 \frac{S}{cm \cdot eV}$, found for the Γ_{4g} state, is very comparable to the value of $-527 \frac{S}{cm \cdot eV}$, calculated for Mn₃Sn in Ref. [51], indicating that tunable anomalous Nernst coefficients by means of in plane rotation of magnetic moments is doable in Mn₃GaN. Further enhancement of the anomalous Nernst coefficient is possible by means of doping and values of the order of $\approx 9000 \frac{S}{cm \cdot eV}$ are expected.

A change of basis modifies the calculated anomalous Hall conductivity values. The calculated anomalous Hall conductivity for the Γ_{4g} magnetic configuration allows finite values in all three components. It will be beneficial however to have an alternative basis in which only one component is finite and the rest are forced to vanish. This is achieved by using the so-called hexagonal geometry, *i.e.*, $a \parallel [1\bar{1}0]$, $b \parallel [10\bar{1}]$ and $c \parallel [111]$. My results verify the presence of one non vanishing component when the magnetic configuration is deviated from the Γ_{5g} . Specifically, the non vanishing component of the anomalous Hall conductivity for the Γ_{4g} state is calculated to be 102 S/cm, corresponding to $\sqrt{3}$ times the $\sigma_{x/y/z}$ in the Cartesian basis, being consistent with the value of 96.3 S/cm calculated in Ref. [74].

4.4. Strain induced anomalous Hall conductivities

An alternative to magnetization rotation mechanism to tune the anomalous Hall and Nernst conductivities is the applied strain. Below, the tunability of these transport properties in Mn_3GaN and Mn_3NiN is discussed.

Mn_3GaN

Finite net magnetization is observed in the distorted Γ_{5g} unit cell. In the unstrained Γ_{5g} magnetic configuration, the magnetic moments are explicitly originating from Mn atoms, lie on the (111)-plane and face towards the adjacent Mn atom. As a result the net magnetization is forced to be zero. Upon applied biaxial strain in the Γ_{5g} configuration, the net magnetization deviates from zero, as shown in Fig. 4.5(a). Specifically, it is found that a value as large as $-0.04 \mu_B$ ($0.03 \mu_B$) for $c/a = 0.99$ ($c/a = 1.01$) is obtained, being consistent with previous studies, the results of which ($\approx 0.04 \mu_B$) [118, 239, 240] match my outcome. The finite value of net magnetization has its roots in the applied strain. By distorting the unit cell, even though the local magnetic moments of all Mn atoms still lie on the (111)-plane, it is observed that the magnitude of all local moments is altered and additionally, the direction of magnetic moments of the atoms Mn2 and Mn3 are canted inwards or outwards depending on the strain (compressive or tensile), forcing the net magnetization to be finite (see inset of Fig. 4.5(c)).

Similarly, finite net magnetization is induced in the distorted Γ_{4g} state. The application of biaxial strain (either compressive or tensile) induces net magnetization with its values being as large as $\mp 0.007 \mu_B$ for $c/a = 0.99$ and $c/a = 1.01$ (see Fig. 4.5(b)), one order of magnitude smaller than those induced in the Γ_{5g} . These finite values occur due to the canting of the local magnetic moments. As in the Γ_{5g} case, when strain is applied, the magnetic moments of all Mn atoms lie on the (111)-plane and have the same magnitude. In contrast, there is a smaller tilt of the magnetic moments of Mn2 and Mn3 atoms which is calculated at around -0.5° (0.5°) for -1% (1%) strain, as illustrated in Fig. 4.5(d).

As previously discussed, magnetic space group symmetries determine the shape of the anomalous Hall conductivity tensor. It is observed that the canting of the magnetic moments in the Γ_{5g} state alters the magnetic space group from $R\bar{3}m$ (166.97) to $C2/m$ (12.58) and that in the Γ_{4g} state from $R\bar{3}m'$ (166.101) to $C2'/m'$ (12.62). As a consequence the new symmetries impose $\sigma_z = 0$ while the leave σ_x and σ_y unrestricted. The calculated anomalous Hall conductivity for several values of compressive and tensile strain and for both Γ_{5g} and Γ_{4g} magnetic configurations are illustrated in Fig, 4.5(c) and Fig. 4.5(d) respectively. Interestingly, for the distorted Γ_{5g} state, σ_x and σ_y are the additive inverse of each other while for the distorted Γ_{4g} state, σ_x and σ_y are identical. My results are in complete agreement with the symmetry imposed form of the anomalous

Hall conductivity tensor for the magnetic space groups $C2/m$ and $C2'/m'$ as well as with the ones for $R\bar{3}m$ and $R\bar{3}m'$, reported in Ref. [54], all constructed using Ref [111] and shown in Tab. 4.1. Since the applied strain alters the anomalous Hall conductivity in both magnetic states, a change of $138 S/cm$ in the $\sigma_x = \sigma_{yz}$ is observed as a response to an applied strain of 3.5% for the Γ_{5g} and a change of $60 S/cm$ for a compressive strain of 3.5% in the Γ_{4g} , it is suspected that significant anomalous Hall conductivities is universal for the whole family of antiperovskites and also other materials systems, where piezomagnetic effect is observed. [239]

Mn₃NiN

In contrast to the relatively small anomalous Hall conductivity calculated for the Γ_{4g} state of Mn₃GaN, Mn₃NiN has a significantly larger value at its unstrained Γ_{4g} state. Specifically, a value around $-170 S/cm$ is calculated in its ground state, which is further tuned to almost $300 S/cm$ by applying compressive strain, as shown in Fig. 4.6(a). Since the magnetic space group is independent of the compound, the same arguments for the vanishing components hold in this case. Focusing on Fig. 4.6(b), it is noticed that a sharp peak of the anomalous Hall conductivity is created and shifted in respect to the Fermi energy by applying strain. This observation is particularly important because even though it is not stable for applied compressive strains in Mn₃NiN, its presence could potentially lead to large anomalous Hall conductivity changes in other compounds.

4.5. Origin of anomalous Hall conductivity

In order to investigate the physical reason of the anomalous Hall conductivity peak and its tunability, detailed analysis on the electronic structure was performed. Next we discuss the origin of the peak in Mn₃GaN and the same principles apply to Mn₃NiN.

An interesting question to address is what is the origin of the anomalous Hall conductivity peaks. Focusing on the 3.5% applied compressive biaxial strain, explicit band structure analysis reveals the occurrence of Weyl nodes, located at $(-0.02, 0.02, -0.4996)$ (in the k -space with the unit of $2\pi/a$) (and symmetry equivalent). In order to calculate the contribution of these Weyl nodes to the total value, a cube of acme 0.08 with the Weyl point in its centre for each symmetry related Weyl node was constructed in the Brillouin zone. Subsequently, the anomalous Hall conductivity was calculated for each of those cubes, therefore the sum shows the contribution exclusively originating from the vicinity of the Weyl nodes. Fig. 4.7 shows the calculated total anomalous Hall conductivity from the whole Brillouin zone (solid lines) as well as the sum of the Weyl nodes contribution (dot-dashed lines). My results demonstrate the Weyl nodes significantly contribute to

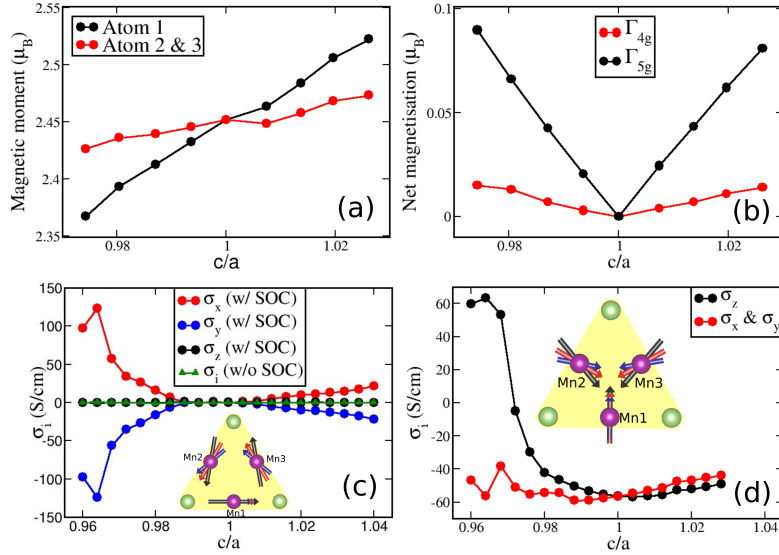


Figure 4.5.: Mn_3GaN : (a) Magnetic moments of Mn atoms in both Γ_{5g} and Γ_{4g} configurations for different c/a values. (b) Net magnetization for different c/a values for Γ_{5g} and Γ_{4g} configurations. (c) Anomalous Hall conductivity in the Γ_{5g} configuration for different c/a values. Configuration canting due to strain is illustrated in the inset where the red arrows correspond to the initial unstrained configuration whereas blue arrows correspond to compressive and black arrows to tensile applied biaxial strain respectively. (d) Anomalous Hall conductivity in the Γ_{4g} configuration for different c/a values. Configuration canting due to strain is illustrated in the inset where the red arrows correspond to the initial unstrained configuration whereas blue arrows correspond to compressive and black arrows to tensile applied biaxial strain respectively

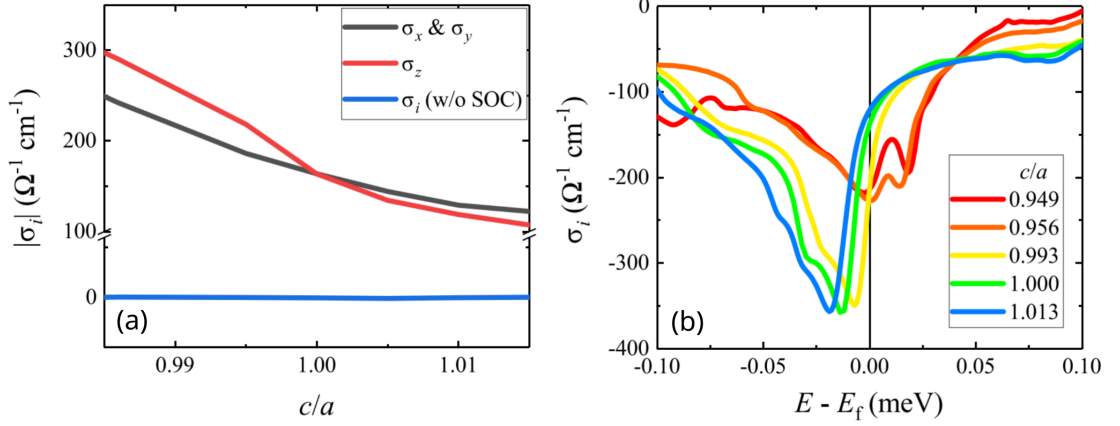


Figure 4.6.: Mn_3NiN , Γ_{4g} : (a) Anomalous Hall conductivity at the Fermi energy as a function of strain in Mn_3NiN (b) Anomalous Hall conductivity as a function of energy for different strain values.

the total value by being responsible for 68 S/cm out of 76 S/cm , as shown in Fig. 4.7. Similarly, for the case of 3% applied strain, 95 S/cm out of 138 S/cm is originating from the vicinity of the Weyl nodes.

Focusing on Fig. 4.7, it becomes clear that the applied strain tunes the energy position of the anomalous Hall conductivity peak in respect to the Fermi energy. Specifically, the position of the peaks moves from 0.075 eV above to 0.010 eV below the Fermi energy for applied compressive strain between 1.0% and 3.5%. Detailed analysis reveals that the same Weyl nodes are responsible for the enhanced value of anomalous Hall conductivity for all values of applied strain and additionally their energy positions are matching the energy positions of the peaks in relatively good agreement. Therefore, it is observed that the energy position of the Weyl nodes are tuned due to the applied strain leading to anomalous Hall contribution peaks which are also tuned in energy. The most significant contribution the anomalous Hall conductivity at the Fermi energy is observed in 3.0% and 3.5% compressive strain where the position of the Weyl nodes are located 0.024 eV and -0.014 eV in respect to the Fermi energy. For larger values of strain there is no contribution to the anomalous Hall conductivity at the Fermi energy (from these specific Weyl nodes) due to the large distance between the Weyl node and the Fermi energy. It is stressed that my results witness that a difference of 0.024 eV in energy between the Fermi level and the Weyl point is enough to have significant contributions to the total anomalous Hall conductivity in contrast to Ref. [74], according to which Weyl points located more than

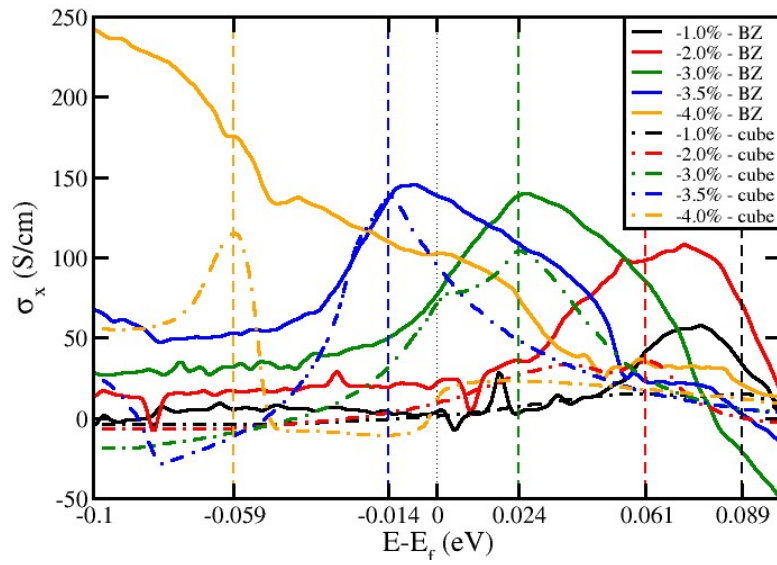


Figure 4.7.: The x-component of total (solid line) and Weyl point driven (dashed line) anomalous Hall conductivity for different applied strain in Mn_3GaN

0.001eV away from the Fermi level have negligible contribution to the total anomalous Hall conductivity.

5. Topological properties of ferromagnets

The anomalous Hall and Nernst conductivities of ferromagnetic compounds and their dependence on applied biaxial strain, doping and magnetization direction changes were investigated. Similar symmetry arguments to the non-collinear ferromagnets are extracted, demonstrating the universality of the analysis. My results further demonstrate that the Weyl nodes, nodal lines and small gap areas located in the proximity of the Fermi energy significantly contribute to the calculated anomalous Hall and Nernst conductivities and they can be further tuned by means of external stimuli in order to further enhance their topological properties. The current chapter is based on Ref. [176], Ref. [177] and Ref. [178].

5.1. Workflow

The topological transport properties of all compounds have been calculated using an in-house developed Python scheme that is available in github¹. The scheme links VASP [99, 97, 98] and Wannier90 [163] software to construct Wannier functions in four steps and subsequently Wanniertools [226] to compute the topological properties. It is applicable for any transition metal based compound, with or without the inclusion of spin orbit interaction. It is further noted that code offers an error detection functionality which is able to identify partially finished or problematic calculations and resubmit only the missing parts.

The complete process is illustrated in Fig. 5.1 and each step of the process is briefly discussed. A detailed explanation is provided in Ref. [244]

- In the first step, a self consistent first-principles calculation is performed.
- In the second step, an accurate projected density of states for all orbitals is performed.
- Subsequently, the Wannier functions are constructed. Bloch states are projected on maximally localized Wannier functions with the selection of the projected orbitals

¹Github link: <https://github.com/TMM-TUDA/Automatic-wannier-flow>

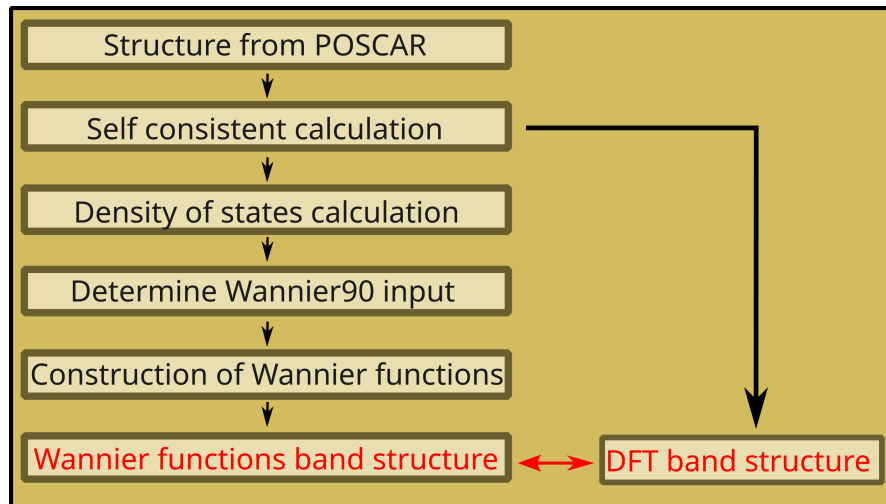


Figure 5.1.: Automated wannier flow

and the inner and outer windows used for disentanglement and wannierization by Wannier90 are determined automatically based on the projected density of states in order to minimize human intervention.

- Then, the band structure of the DFT is calculated and compared to the one obtained from the Wannier functions.
- Finally, the anomalous Hall and Nernst conductivities are calculated

The workflow was used to construct the Wannier functions of 289 ferromagnetic compounds, resulting in good agreement of wannier-functions-based band structures and DFT-based-band structures in 266 of them, giving rise to a success rate of 92%. In comparison, a success rate of 93% and 97% is achieved in Ref. [43] and Ref. [215] respectively. My results provide an alternative to the existing automatic construction of Wannier functions [146, 172, 43, 215, 238] and enabled me to perform further calculations to evaluate the desired physical properties.

Since unexpected errors can occur while running different software, it is important to anticipate of them. The scheme is equipped with an automated error handling functionality that can identify several errors in the procedure, adjust the input files, if necessary, and resubmit the missing parts. In this way, computational resources are saved and the results are delivered faster.

5.2. Notable anomalous Hall/Nernst values

The aforementioned workflow has been used to construct the maximally localized Wannier functions that were subsequently used to compute the anomalous Hall and Nernst conductivities of the 266 ferromagnetic compounds shown in Tab B.1 in supplementary for two magnetization directions ([001] and [100]). Fig. 5.2 shows the z-component of the anomalous Hall and Nernst conductivities of the most notable compounds when the magnetization direction is parallel to [001] axis. It is noted that 11 compounds exhibit absolute value of anomalous Hall conductivity larger than $1000S/cm$, with the most notable being $-2051S/cm$ for Ni_3Pt and $2040S/cm$ for $CrPt_3$. It is noted that these compounds exhibit anomalous Hall conductivities that are larger than the $-1862S/cm$ for Rh_2MnGa and $-1723S/cm$ for Rh_2MnAl , [146] which are the largest reported, arising the question whether there is an upper limit and opens up the possibility to engineer materials with more significant magnitudes. Similarly, the anomalous Nernst conductivity of 16 compounds exceeds $3A/(m \cdot K)$, with the most notable values being $-7.29A/(m \cdot K)$ and $5.83A/(m \cdot K)$ that are attributed to Ni_3Pt and BCo_4Y respectively.

Concomitant, the x-component of the anomalous Hall conductivity, with the magnetization direction being parallel to [100]-axis, is calculated and the results are illustrated in Fig. 5.3. There exist also 11 compounds with anomalous Hall conductivity larger than the absolute value of $1000S/cm$ and also 16 with anomalous Nernst larger than the absolute value of $3A/(m \cdot K)$ while the differences arise in the case of non cubic compounds in which the symmetries towards these directions are discrepant.

It is noted that even though the total anomalous Hall and Nernst conductivities are not dependent on the choice of the unit cell, their projected values along the unit cell axes are. This fact makes comparisons with the literature difficult and sometimes inaccurate. However, my results are, in general, in good agreement with the literature with some examples being $Co_3Sn_2S_2$ with a reported value of $1130S/cm$ [112] that was calculated $988S/cm$ in my work, the Heusler compounds Co_2VGa and Co_2MnSn with reported values of $137S/cm$ in Ref. [122] and $118S/cm$ in Ref. [100] that were calculated $140S/cm$ and $200S/cm$ in my work and the XPt_3 family with $X = (Cr, Mn)$ where the reported cases of $2040S/cm$ and $1400S/cm$ [123] are reproduced by my values of $2000S/cm$ and $1471S/cm$. As for the anomalous Nernst conductivity, the parameter of temperature is an additional factor that makes comparisons difficult although the calculated value of $4.58A/(m \cdot K)$ for $MnPt_3$ is consistent with the reported value of $4A/(m \cdot K)$ in Ref. [123].

Magnetism might generate anisotropic responses. In the absence of time reversal symmetry (magnetic materials), after considering spin orbit coupling, the symmetry and the electron structure is dependent on the magnetization direction. The relation

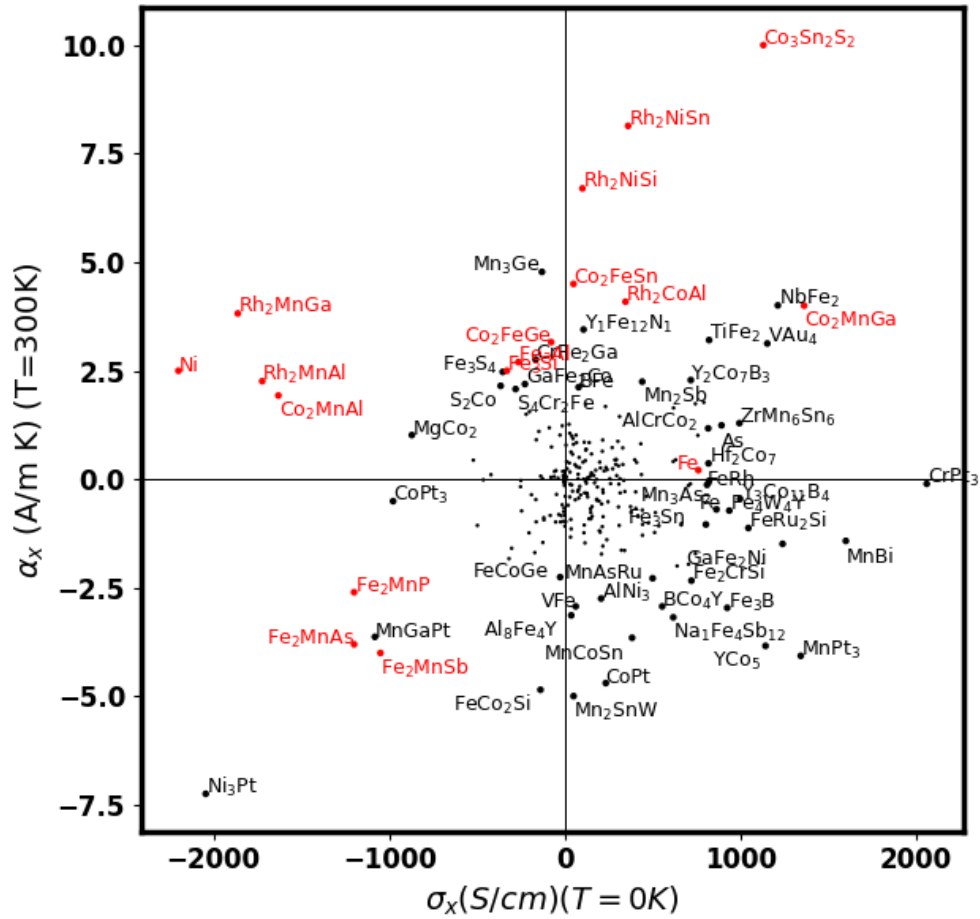


Figure 5.3.: The x-component of anomalous Hall conductivity and anomalous Nernst conductivity for the most promising ferromagnetic compounds. Existing values in literature are marked in red while the results of this work in black

between the direction of the induced vector and the magnetization has been studied in Ref. [238], challenging the commonly assumed formula $j^{AHE} = M \times E$. In my work, I quantify ferromagnetic materials based on the difference of the induced anomalous Hall conductivity for two different magnetization directions *i.e.* [100] and [001] by using the anisotropy. Specifically, the ratio $\sigma_{x,M||[100]}/\sigma_{z,M||[001]}$ or $\alpha_{x,M||[100]}/\alpha_{z,M||[001]}$ is calculated and subsequently the compounds are classified into anisotropic or isotropic depending on the resulting anisotropy. Clearly large “large” values signify large changes in favor of the [100] direction while “small” values (excluding the cases where both anomalous Hall conductivity values are lower than $10S/cm$ and both anomalous Nernst conductivity values lower than $0.05A/(m \cdot K)$ and therefore considered negligible) are in favor of the [001] magnetization direction. The most anisotropic compounds in favour of the [100] direction are Rh_2MnSb and Fe_3Se_4 , with anisotropy values of 53.32 and -33.39 respectively and the most anisotropic in favour of [001] are PFe and Fe_2Ge with values of -0.01 and 0.004 respectively. In Tab. B.1 the anisotropy values of all compounds are presented.

5.3. Symmetry analysis

The simple ferromagnetic nature of the compounds allows detailed analysis of the Berry curvature transformations that will give an insight on the anomalous Hall conductivity. In the following, I discuss in detail the transformations of the Berry curvature and their impact to the anomalous Hall conductivity of a compound that belongs to the magnetic space group $P4/mmm'm'$ (123.345) with the corresponding magnetic point group being $4/mmm'm'$ (15.6.58). Tab. 5.1 shows the resulting Berry curvature under the application of all symmetries of the magnetic point group $4/mmm'm'$. It is noted that the application of 2_{001} , m_{001} , $2'_{100}$ and m'_{100} reverses the sign of the x-component of the Berry curvature and similarly the application of 2_{001} , m_{001} , $2'_{010}$ and m'_{010} the sign of the y-component, whereas no symmetry reverses the sign of the z-component. Since the components of the anomalous Hall conductivities are proportional to the summation of the respective Berry curvature in the whole Brillouin zone, the sign reverse in x- and y- components of Berry curvature implies $\sigma_x = \sigma_y = 0$, however z-component is allowed to exhibit finite value.

In order to further investigate the importance of each symmetry on the previous example, I consider a random point with spatial coordinates $\mathbf{k} = (k_x, k_y, k_z)$ and corresponding Berry curvature pseudovector $\boldsymbol{\Omega} = (\Omega_x, \Omega_y, \Omega_z)$, denoted by the red triangle, square and circular shapes respectively, as illustrated in Fig 5.4. The transformations of each of the 16 symmetry operations of the magnetic Laue group are marked with numbers from 1 to 16 and the order matches with the order presented in the Tab. 5.1. Symbols with red

represent positive Berry curvature values, whereas the negative ones are denoted with blue. In panels (a), (b), (c) and (d), cuts of the Brillouin zone along the k_z and $-k_z$ planes for the Ω_x and Ω_y components of the Berry curvature are illustrated and the presence of equal number of the opposite colored symbols forces Ω_x and Ω_y components of the Berry curvature to vanish. On the other hand, no symmetry reverses the sign of Ω_z component of the Berry curvature as illustrated in panels (e) and (f), therefore it is allowed to exhibit finite value. Since the anomalous Hall conductivity is proportional to the sum of the Berry curvature in the whole Brillouin zone, the x and y components are expected to vanish, whereas the z component is allowed to have finite value.

Table 5.1.: The matrix representation and the Berry curvature transformation of the symmetry operations of the magnetic point group $4/m\bar{m}'m'$ (15.6.58)

Number	Symmetry	Matrix Representation	Berry Curvature
1	1	$\begin{pmatrix} 1 & 0 & 0 \\ 0 & 1 & 0 \\ 0 & 0 & 1 \end{pmatrix}$	$\Omega_x(k_x, k_y, k_z) = \Omega_x(k_x, k_y, k_z)$ $\Omega_y(k_x, k_y, k_z) = \Omega_y(k_x, k_y, k_z)$ $\Omega_z(k_x, k_y, k_z) = \Omega_z(k_x, k_y, k_z)$
2	4_{001}^+	$\begin{pmatrix} 0 & -1 & 0 \\ 1 & 0 & 0 \\ 0 & 0 & 1 \end{pmatrix}$	$\Omega_x(-k_y, k_x, k_z) = \Omega_y(k_x, k_y, k_z)$ $\Omega_y(-k_y, k_x, k_z) = -\Omega_x(k_x, k_y, k_z)$ $\Omega_z(-k_y, k_x, k_z) = \Omega_z(k_x, k_y, k_z)$
3	4_{001}^-	$\begin{pmatrix} 0 & 1 & 0 \\ -1 & 0 & 0 \\ 0 & 0 & 1 \end{pmatrix}$	$\Omega_x(k_y, -k_x, k_z) = -\Omega_y(k_x, k_y, k_z)$ $\Omega_y(k_y, -k_x, k_z) = \Omega_x(k_x, k_y, k_z)$ $\Omega_z(k_y, -k_x, k_z) = \Omega_z(k_x, k_y, k_z)$
4	2_{001}	$\begin{pmatrix} -1 & 0 & 0 \\ 0 & -1 & 0 \\ 0 & 0 & 1 \end{pmatrix}$	$\Omega_x(-k_x, -k_y, k_z) = -\Omega_x(k_x, k_y, k_z)$ $\Omega_y(-k_x, -k_y, k_z) = -\Omega_y(k_x, k_y, k_z)$ $\Omega_z(-k_x, -k_y, k_z) = \Omega_z(k_x, k_y, k_z)$
5	-1	$\begin{pmatrix} -1 & 0 & 0 \\ 0 & -1 & 0 \\ 0 & 0 & -1 \end{pmatrix}$	$\Omega_x(-k_x, -k_y, -k_z) = \Omega_x(k_x, k_y, k_z)$ $\Omega_y(-k_x, -k_y, -k_z) = \Omega_y(k_x, k_y, k_z)$ $\Omega_z(-k_x, -k_y, -k_z) = \Omega_z(k_x, k_y, k_z)$
6	-4_{001}^+	$\begin{pmatrix} 0 & 1 & 0 \\ -1 & 0 & 0 \\ 0 & 0 & -1 \end{pmatrix}$	$\Omega_x(k_y, -k_x, -k_z) = \Omega_y(k_x, k_y, k_z)$ $\Omega_y(k_y, -k_x, -k_z) = -\Omega_x(k_x, k_y, k_z)$ $\Omega_z(k_y, -k_x, -k_z) = \Omega_z(k_x, k_y, k_z)$
7	-4_{001}^-	$\begin{pmatrix} 0 & -1 & 0 \\ 1 & 0 & 0 \\ 0 & 0 & -1 \end{pmatrix}$	$\Omega_x(-k_y, k_x, -k_z) = -\Omega_y(k_x, k_y, k_z)$ $\Omega_y(-k_y, k_x, -k_z) = \Omega_x(k_x, k_y, k_z)$ $\Omega_z(-k_y, k_x, -k_z) = \Omega_z(k_x, k_y, k_z)$
8	m_{001}	$\begin{pmatrix} 1 & 0 & 0 \\ 0 & 1 & 0 \\ 0 & 0 & -1 \end{pmatrix}$	$\Omega_x(k_x, k_y, -k_z) = -\Omega_x(k_x, k_y, k_z)$ $\Omega_y(k_x, k_y, -k_z) = -\Omega_y(k_x, k_y, k_z)$ $\Omega_z(k_x, k_y, -k_z) = \Omega_z(k_x, k_y, k_z)$
9	$2'_{100}$	$\begin{pmatrix} 1 & 0 & 0 \\ 0 & -1 & 0 \\ 0 & 0 & -1 \end{pmatrix}$	$\Omega_x(-k_x, k_y, k_z) = -\Omega_x(k_x, k_y, k_z)$ $\Omega_y(-k_x, k_y, k_z) = \Omega_y(k_x, k_y, k_z)$ $\Omega_z(-k_x, k_y, k_z) = \Omega_z(k_x, k_y, k_z)$
10	$2'_{010}$	$\begin{pmatrix} -1 & 0 & 0 \\ 0 & 1 & 0 \\ 0 & 0 & -1 \end{pmatrix}$	$\Omega_x(k_x, -k_y, k_z) = \Omega_x(k_x, k_y, k_z)$ $\Omega_y(k_x, -k_y, k_z) = -\Omega_y(k_x, k_y, k_z)$ $\Omega_z(k_x, -k_y, k_z) = \Omega_z(k_x, k_y, k_z)$
11	$2'_{110}$	$\begin{pmatrix} 0 & 1 & 0 \\ 1 & 0 & 0 \\ 0 & 0 & -1 \end{pmatrix}$	$\Omega_x(-k_y, -k_x, k_z) = -\Omega_y(k_x, k_y, k_z)$ $\Omega_y(-k_y, -k_x, k_z) = -\Omega_x(k_x, k_y, k_z)$ $\Omega_z(-k_y, -k_x, k_z) = \Omega_z(k_x, k_y, k_z)$
12	$2'_{1-10}$	$\begin{pmatrix} 0 & -1 & 0 \\ -1 & 0 & 0 \\ 0 & 0 & -1 \end{pmatrix}$	$\Omega_x(k_y, k_x, k_z) = \Omega_y(k_x, k_y, k_z)$ $\Omega_y(k_y, k_x, k_z) = \Omega_x(k_x, k_y, k_z)$ $\Omega_z(k_y, k_x, k_z) = \Omega_z(k_x, k_y, k_z)$
13	m'_{100}	$\begin{pmatrix} -1 & 0 & 0 \\ 0 & 1 & 0 \\ 0 & 0 & 1 \end{pmatrix}$	$\Omega_x(k_x, -k_y, -k_z) = -\Omega_x(k_x, k_y, k_z)$ $\Omega_y(k_x, -k_y, -k_z) = \Omega_y(k_x, k_y, k_z)$ $\Omega_z(k_x, -k_y, -k_z) = \Omega_z(k_x, k_y, k_z)$
14	m'_{010}	$\begin{pmatrix} 1 & 0 & 0 \\ 0 & -1 & 0 \\ 0 & 0 & 1 \end{pmatrix}$	$\Omega_x(-k_x, k_y, -k_z) = \Omega_x(k_x, k_y, k_z)$ $\Omega_y(-k_x, k_y, -k_z) = -\Omega_y(k_x, k_y, k_z)$ $\Omega_z(-k_x, k_y, -k_z) = \Omega_z(k_x, k_y, k_z)$
15	m'_{110}	$\begin{pmatrix} 0 & -1 & 0 \\ -1 & 0 & 0 \\ 0 & 0 & 1 \end{pmatrix}$	$\Omega_x(k_y, k_x, -k_z) = -\Omega_y(k_x, k_y, k_z)$ $\Omega_y(k_y, k_x, -k_z) = -\Omega_x(k_x, k_y, k_z)$ $\Omega_z(k_y, k_x, -k_z) = \Omega_z(k_x, k_y, k_z)$

16	m'_{1-10}	$\begin{pmatrix} 0 & 1 & 0 \\ 1 & 0 & 0 \\ 0 & 0 & 1 \end{pmatrix}$	$\begin{aligned} \Omega_x(-k_y, -k_x, -k_z) &= \Omega_y(k_x, k_y, k_z) \\ \Omega_y(-k_y, -k_x, -k_z) &= \Omega_x(k_x, k_y, k_z) \\ \Omega_z(-k_y, -k_x, -k_z) &= \Omega_z(k_x, k_y, k_z) \end{aligned}$
----	-------------	---	---

SiMnY

From the materials point of view, considering SiMnY with the magnetization direction to be aligned along [100]-direction, as an example, we find that the magnetic space group is $Pmm'n'$ (BNS: 59.410) with corresponding magnetic point group $m'm'm$ (8.4.27). As a consequence the presence of the m_{100} symmetry forces σ_y and σ_z components to vanish, whereas leaves σ_x unrestricted, according to:

$$\begin{aligned} \Omega_x(-k_x, k_y, k_z) &= \Omega_x(k_x, k_y, k_z) \\ \Omega_y(-k_x, k_y, k_z) &= -\Omega_y(k_x, k_y, k_z) \\ \Omega_z(-k_x, k_y, k_z) &= -\Omega_z(k_x, k_y, k_z). \end{aligned}$$

On the other hand, the magnetic space group of SiMnY changes to $P4/nm'm'$ (BNS: 129.417) with corresponding magnetic point group $4/mm'm'$ (15.6.58), for the magnetization direction parallel to [001] axis. As a result, the Berry curvature behaves as an odd pseudovector under the application of 2_{100} obeying:

$$\begin{aligned} \Omega_x(-k_x, -k_y, k_z) &= -\Omega_x(k_x, k_y, k_z) \\ \Omega_y(-k_x, -k_y, k_z) &= -\Omega_y(k_x, k_y, k_z) \\ \Omega_z(-k_x, -k_y, k_z) &= \Omega_z(k_x, k_y, k_z). \end{aligned}$$

In this case, the summation over the whole Brillouin zone forces $\sigma_x = \sigma_{yz}$ and $\sigma_y = \sigma_{xz}$ to vanish, leading to the conclusion that for the high-symmetric magnetization directions, the direction of the anomalous Hall conductivity tensor (for this magnetic space groups) is always aligned with the magnetization direction. Since the anomalous Hall and Nernst conductivities depend on the distribution of the Berry curvature in the Brillouin zone that originates from the band topology, it is not uncommon for a system to exhibit incidental zero value despite the lack of symmetries forcing their cancellation. In other words, the absence of symmetries forcing specific components of Berry curvature does not necessarily mean its finite value. For instance, negligible anomalous Hall conductivity is calculated in PFe with magnetization direction parallel to [001]-axis ($Pn'a2'_1$, BNS: 33.146) despite the absence of symmetries forcing the cancellation of σ_z component. In Fig. 5.5(a) and (c) the distributions of σ_z in the whole Brillouin zone, evaluated at $E = E_f$ and $E = E_f - 0.2$ eV are illustrated respectively. The negligible values at the Fermi level are due to the presence of opposite-signed anomalous Hall conductivity in non-symmetry related positions, which

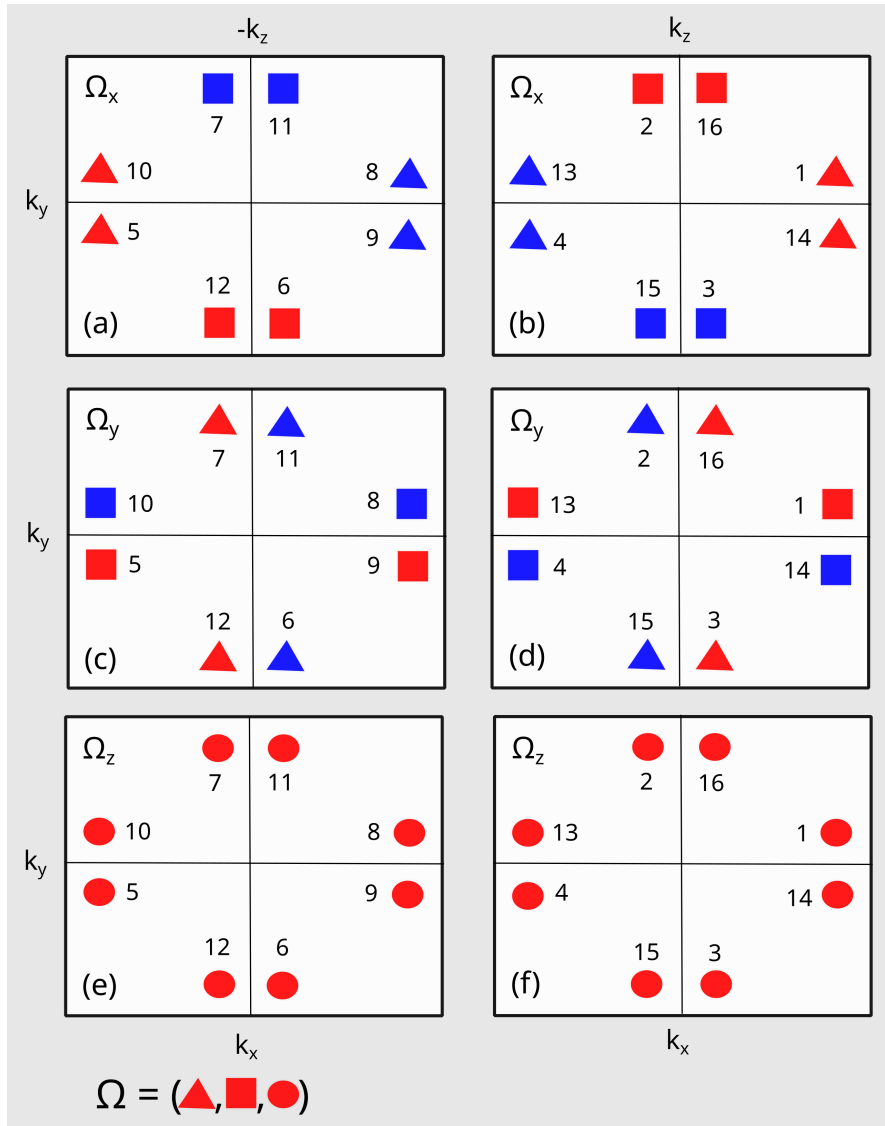


Figure 5.4.: Transformation of every component of the Berry curvature for each of the 16 symmetries of the magnetic point group $4/mmm'$ (15.6.58) (labeled with numbers from 1 to 16) for Brillouin zone cuts along k_z and $-k_z$ planes. Triangles, squares and circles correspond to Ω_x , Ω_y and Ω_z component of the Berry curvature respectively with red color denoting positive Berry curvature values and blue negative

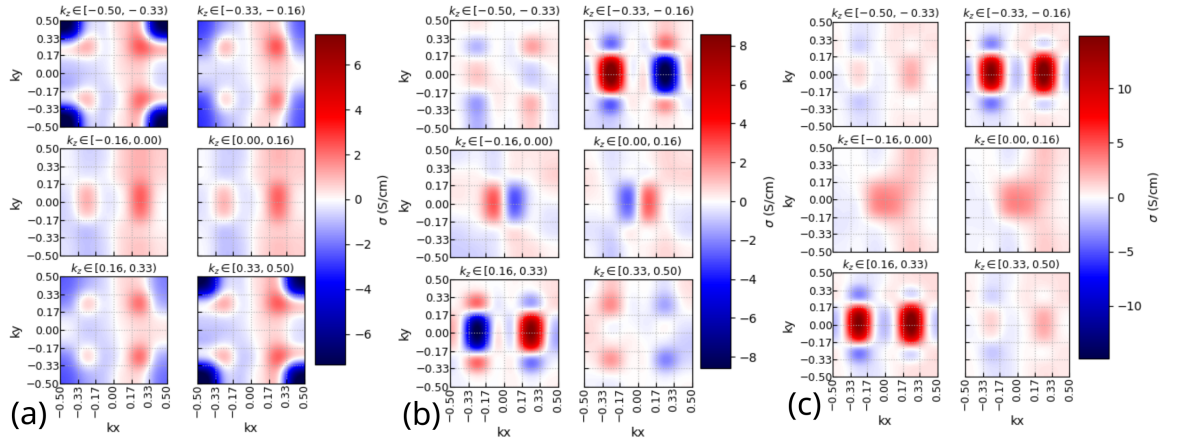


Figure 5.5.: PFe, M//[001]: (a) Distribution of σ_z in the whole Brillouin zone at $E = E_f$ (b) Distribution of σ_x in the whole Brillouin zone at $E = E_f$ (c) Distribution of σ_z in the whole Brillouin zone at $E = E_f - 0.2$ eV

does not occur at $E = E_f - 0.2$ eV. Finally, I present the distribution of σ_x in the whole Brillouin zone, evaluated at $E = E_f$ in Fig. 5.5(b) as a clear indication opposite-signed anomalous Hall conductivities at symmetry related positions.

Since the same symmetry principles apply to both anomalous Hall and Nernst conductivity tensors, it is natural to think that negligible value of the one guarantees negligible value of the other. This is true for components forced to vanish by symmetry, however, there are some conditions which allow zero anomalous Nernst conductivity in the presence of finite anomalous Hall conductivity. As the anomalous Nernst conductivity is proportional to the energy derivative of the anomalous Hall conductivity, the first obvious case appears when the anomalous Hall conductivity is constant for a large energy range around the Fermi energy.

5.4. Origin of anomalous Hall/Nernst conductivities

In this section, I investigate what gives rise to large anomalous Hall conductivity. Recent works have shown that Weyl nodes and nodal lines, behave either as sinks or as sources of the Berry curvature [136, 186, 230] and hence they are expected to contribute to the total anomalous Hall conductivity. The presence of one of them does not exclude the presence of the others therefore there are systems with mixed contributions. The methodology to identify the mechanism of the enhanced anomalous Hall and Nernst conductivity values

is discussed. The Brillouin zone is cut in $6 \times 6 \times 6 = 216$ cubes of acme 0.166 (in units of $2\pi/a$) and the anomalous Hall conductivity is calculated in each of them. Hot-spot areas (if they exist) are identified and the band gap of all band pairs within a specified energy range are evaluated. The shape of the band gaps in three dimensional k space witnesses the type of the contribution mechanism. Below, I discuss in detail some compounds in which the contributions are originating from different mechanisms.

MnZn

The anomalous Hall and Nernst conductivities as a function of energy for MnZn with magnetization direction parallel to [001]-axis are shown in blue curves of Fig. 5.6(a) and (b) respectively. A sharp peak of $1082S/cm$, at the anomalous Hall conductivity curve, located about $4meV$ below the Fermi energy, is noted. In order to investigate the origin, we split the Brillouin zone in 216 cubes, as already discussed and evaluate the anomalous Hall conductivity in each of those. The results are illustrated in Fig. 5.7. Several hot-spot areas are identified, such as the cube $k_x \in [0.000, 0.166]$, $k_y \in [0.333, 0.500]$, $k_z \in [-0.333, -0.166]$. However, deeper analysis of the magnetic point group of the compound, reveals that all these hot spot areas are symmetry related with each other, therefore analyzing one is sufficient. Focusing on the aforementioned cube, the band gap of all pairs of bands within $E \in [-8, 0]$ meV from the Fermi level is calculated and the results for different k_z planes are shown in Fig. 5.8(a)-(c). Using a much denser k_z mesh, it is possible to extract the shape of the touching points that happens to form nodal lines of the form of Fig.5.8(d). Hence the contribution to both anomalous Hall and Nernst around the nodal lines are evaluated and turns out to be 73% ($782S/cm$ out of $1082S/cm$), similarly to the role of Weyl nodes in Mn_3PdN [186] and 95% of the total conductivities respectively, as shown in red curves Fig. 5.6(a) and (b).

Ni₃Pt

Significantly different anomalous Hall and Nernst conductivity curves than the one discussed are calculated for Ni₃Pt. An increasing negative value without the presence of any notable peaks close to the Fermi energy is observed in Fig. 5.9(a) and (b). Using the same methodology described above, the distribution of the anomalous Hall conductivity for Ni₃Pt with magnetization direction parallel to [100] axis for the 216 cubes was evaluated and it is shown in Fig. 5.10. In contrast to the MnZn case, Ni₃Pt does not show any notable hot spot area, instead almost every cube significantly contribute to the total anomalous Hall conductivity. This result is supported by the Weyl nodes search that resulted in more than 200 Weyl nodes within an energy range of $2meV$ above and below the Fermi energy, making the explicit analysis challenging. Additionally, two snapshots of the band gap at different k_z planes shown in Fig. 5.11(a) and (b) confirm

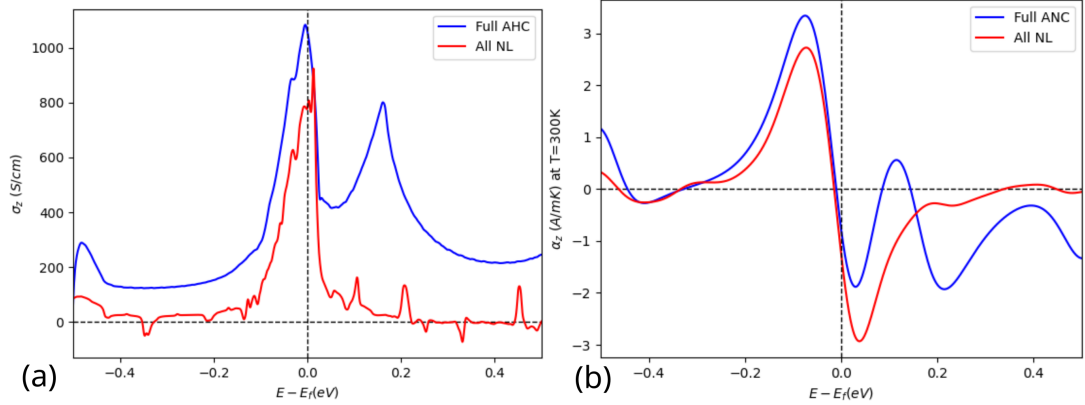


Figure 5.6.: MnZ, M//[001]: (a) Total and nodal line driven anomalous Hall conductivity as a function of energy (b) Total and nodal line driven anomalous Nernst conductivity as a function of energy

the rich behaviour of Weyl nodes, nodal lines and small gap areas. Despite the difficulties, it is possible to identify several nodal lines as well as small gap areas, as the one with $k_x \in [0.333, 0.500]$, $k_y \in [0.000, 0.166]$ proving that compounds without hot-spot areas are able of exhibiting large anomalous Hall and Nernst conductivities of $-2051 S/cm$ and $-7.29 A/mK$ respectively.

Re₂MnTa

A large anomalous Hall conductivity has been found in Re₂MnTa², where a value of almost $2060 S/cm$ has been calculated at the Fermi energy, as shown in Fig. 5.12. The distribution of the anomalous Hall conductivity within the Brillouin zone, indicates 16 symmetry related hot-spots, similar to the one with $k_x \in [0.166, 0.333]$, $k_y \in [-0.166, 0.000]$, $k_z \in [0.333, 0.500]$ shown in Fig. 5.13. Explicit Weyl point search indicates the presence of Weyl nodes within the hot-spot cubes that comprise almost 3/4 of the total anomalous Hall conductivity, illustrated in Fig. 5.12, despite being only 7.4% of the total volume of the unit cell, demonstrating that anomalous Hall conductivity can originate from areas around Weyl nodes.

²The calculations of anomalous Hall conductivity for Re₂MnTa were performed by Farhan Tanzim during his master thesis project in the group of theory of magnetic materials, under the supervision of Dr. Ruiwen Xie and myself.

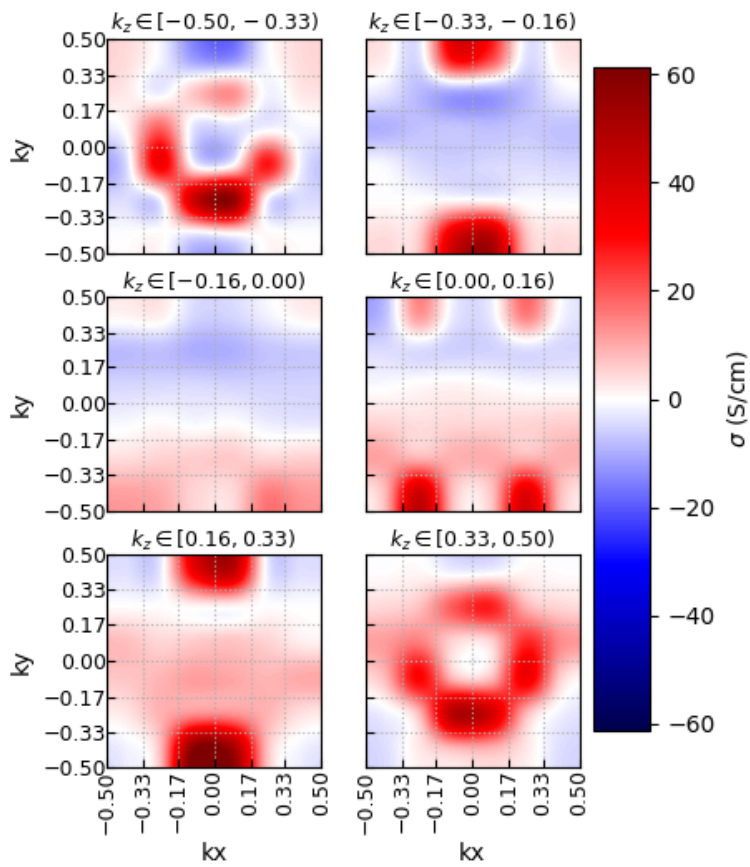


Figure 5.7.: MnZn, M//[001]: Distribution of σ_z in the whole Brillouin zone at $E = E_f$

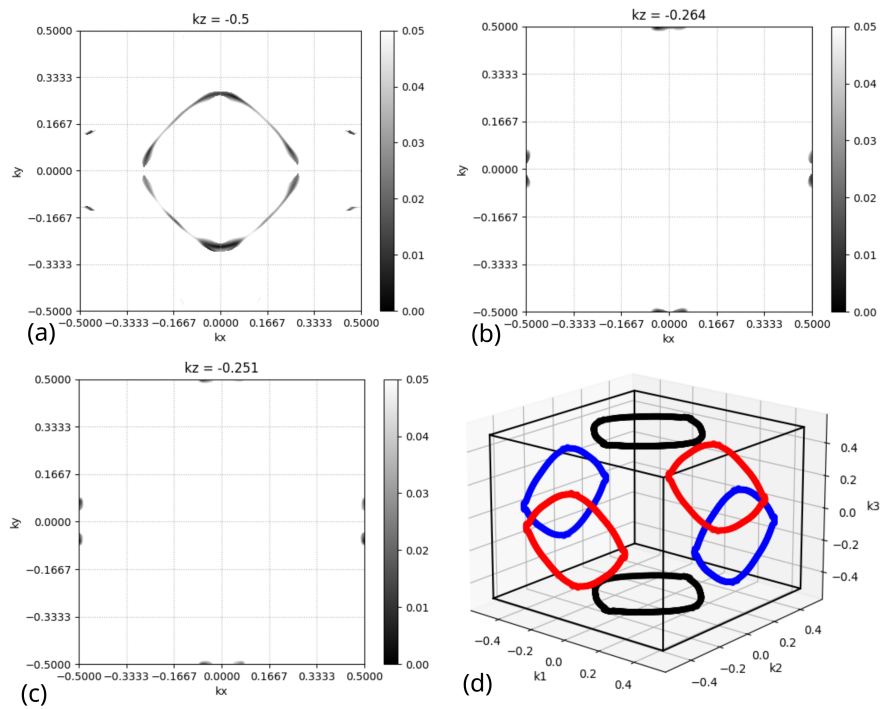


Figure 5.8.: MnZn, M//[001]: (a)-(c) The gap of a pair of bands for cuts of Brillouin zone at different k_z planes. (d) Shape of reconstructed nodal lines

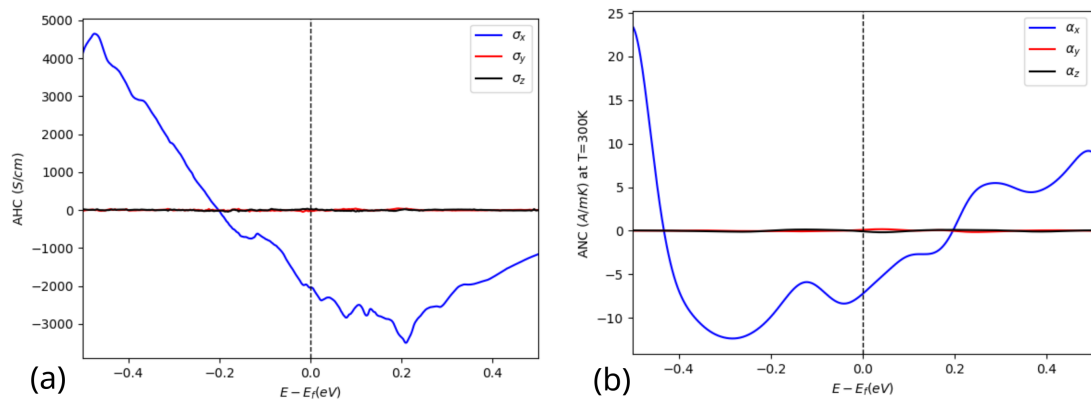


Figure 5.9.: Ni₃Pt, M//[100]: (a) Total anomalous Hall conductivity as a function of energy. (b) Total anomalous Nernst conductivity as a function of energy

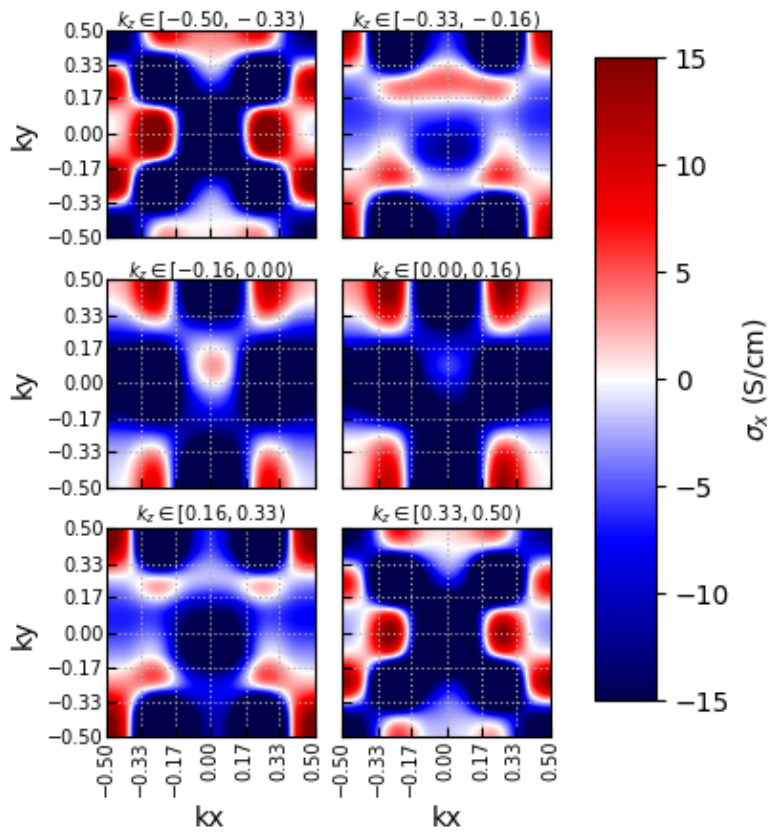


Figure 5.10.: Ni_3Pt , $M//[100]$: Distribution of σ_x in the whole Brillouin zone at $E = E_f$

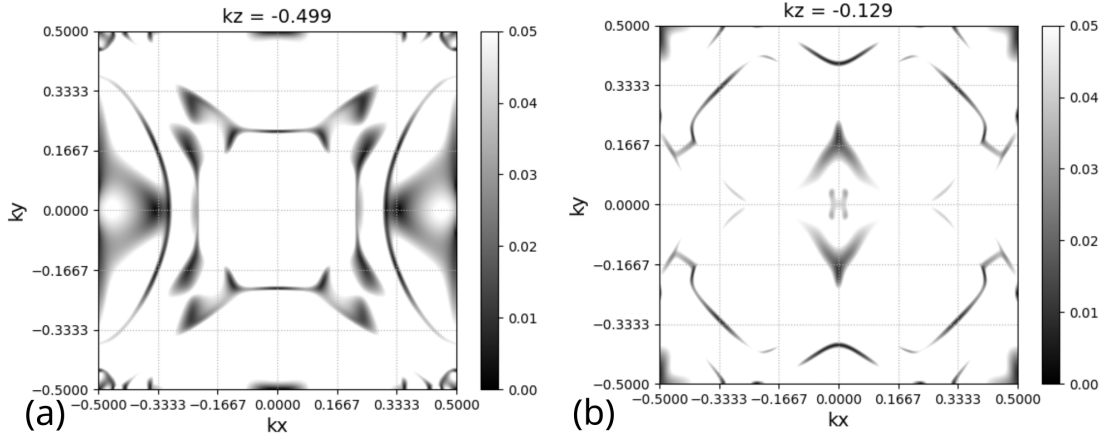


Figure 5.11.: Ni_3Pt , $M//[100]$: The gap of a pair of bands for cuts of Brillouin zone at different k_z planes

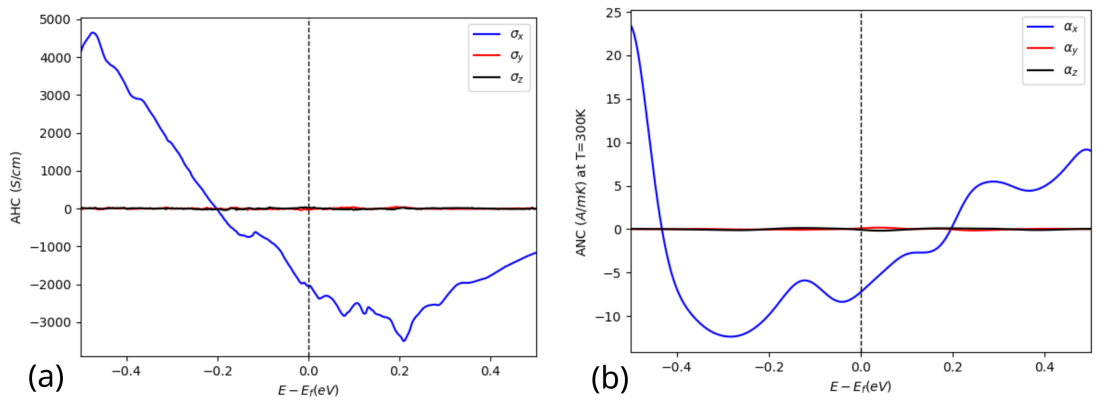


Figure 5.12.: Re_2MnTa , $M//[001]$: (a) Total anomalous Hall conductivity as a function of energy (b) Total anomalous Nernst conductivity as a function of energy

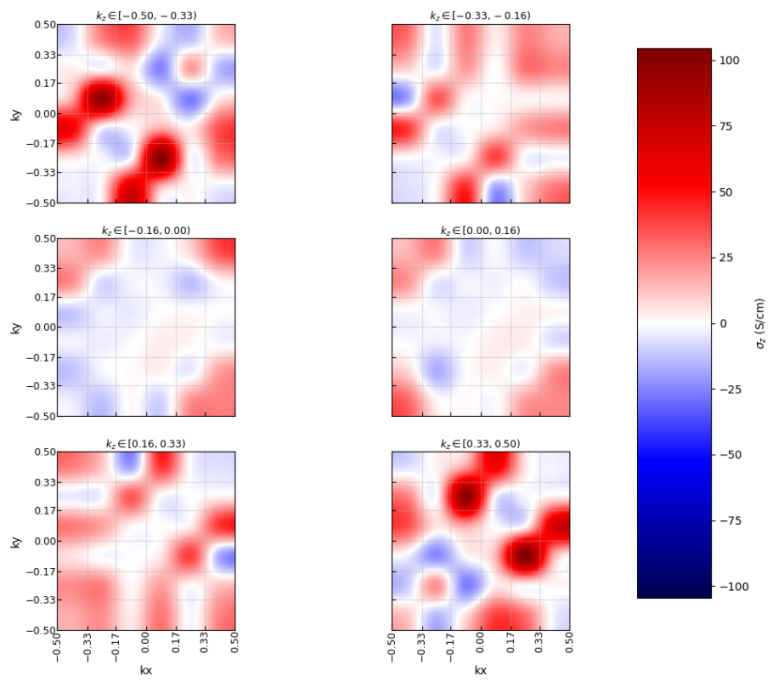


Figure 5.13.: Re_2MnTa , $M//[101]$: Distribution of σ_z in the whole Brillouin zone at $E = E_f$

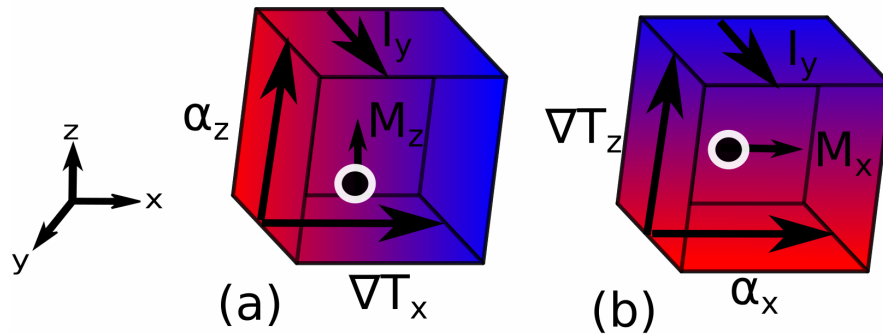


Figure 5.14.: Schematic illustration of the induced anomalous Nernst conductivity direction change for (a) magnetization direction parallel to [001] axis (b) magnetization direction parallel to [100] axis.

5.5. Magnetization induced anomalous Hall/Nernst conductivities

In the presence of spin orbit coupling, the magnetization direction can have significant impact to the anomalous Hall conductivity as it was already discussed. Additionally, the magnetic space group of the compounds discussed implies anomalous Hall and Nernst conductivities to be parallel to the magnetization direction, offering in such a way interesting possibilities of different geometries, as shown in Fig. 5.14. In this section the possibility of inducing different value of anomalous Hall conductivity for two magnetization directions [100]-axis and [001]-axis is discussed. It is expected that for cubic systems there will be no difference between the anomalous Hall conductivity of the two discrepant directions. Some interesting cases follow.

YCo₅

Magnetization direction significantly affects the induced anomalous Hall and Nernst conductivities. One of the most subtle changes is observed in YCo₅ where a change of almost $900 S/cm$ (from $250 S/cm$ to $1142 S/cm$) while changing the magnetization from [001] to [100] axis, as illustrated in Fig. 5.15(a). Interestingly, the anomalous Nernst conductivity not only exhibits a large change of more than $7 A/(m \cdot K)$ (from $-3.83 A/(m \cdot K)$ to $3.33 A/(m \cdot K)$) but also a change of sign. As shown in Fig. 5.15(b), YCo₅ exhibits one of the largest reported anomalous Nernst conductivity values ($-11.54 A/(m \cdot K)$) that is located $0.078 eV$ above the Fermi level. Since the peak is located close enough to the Fermi energy, applied mechanical deformations can tune the position of the peak in respect to

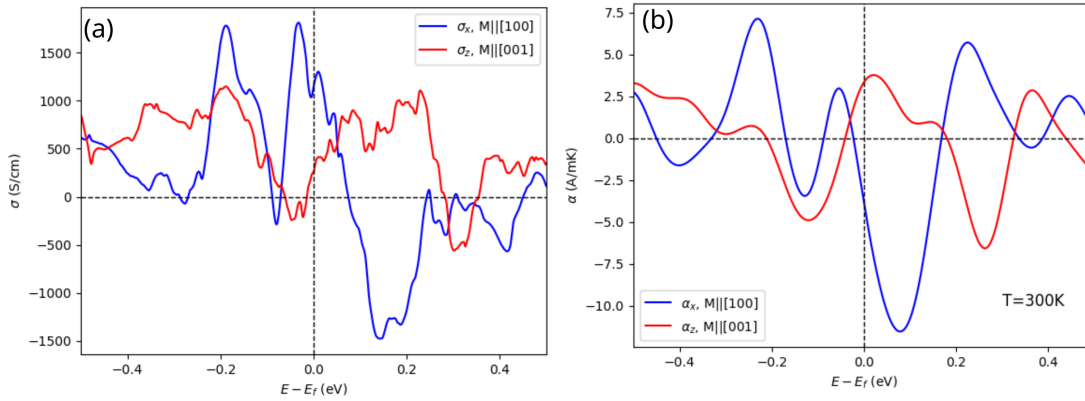


Figure 5.15.: YCo₅: (a) Anomalous Hall conductivity for different magnetization directions. (b) Anomalous Nernst conductivity at $T = 300K$ for different magnetization directions

the Fermi energy, rendering it as a promising compounds for thermoelectric applications

TiMnP

The anomalous Hall conductivity of TiMnP for magnetization direction parallel to [100]-axis and [001]-axis has been calculated and the results signify an increase of more almost three times in favour of the [100]-axis (from $224S/cm$ to $624S/cm$). In order to investigate the origin of the difference, the k_z axis is split in 50 parts ($k_z \in [0.00, 0.50]$ is sufficient since the symmetry indicated that the negative part is equivalent) and the anomalous Hall conductivity is calculated within. The percentage of anomalous Hall conductivity difference between the two magnetization directions, namely [100] and [001] is illustrated in Fig. 5.16. It is clear that the largest difference originates from $k_z \in [0.00, 0.01]$ that is responsible for almost 15% of the whole difference. Detailed calculations demonstrate an increase of the anomalous Hall conductivity calculated for $M \parallel [100]$ in comparison to the value calculated for $M \parallel [001]$ in the regions $k_x \in [-0.2, 0.2], k_y \in [0.0, 0.1]$ (and symmetry equivalent), as shown in Fig. 5.17, which is possibly linked to the creation of Weyl nodes, nodal line or small gap areas in these areas. Despite this observation, as it is obvious, the difference is quite uniform in the whole Brillouin zone and it cannot be attributed specifically to these regions. Surprisingly, the anomalous Nernst conductivity exhibits a peculiar behavior, where the negligible value at magnetization parallel to [001] axis becomes $-2.08 A/mK$ for magnetization parallel to [100]-axis.

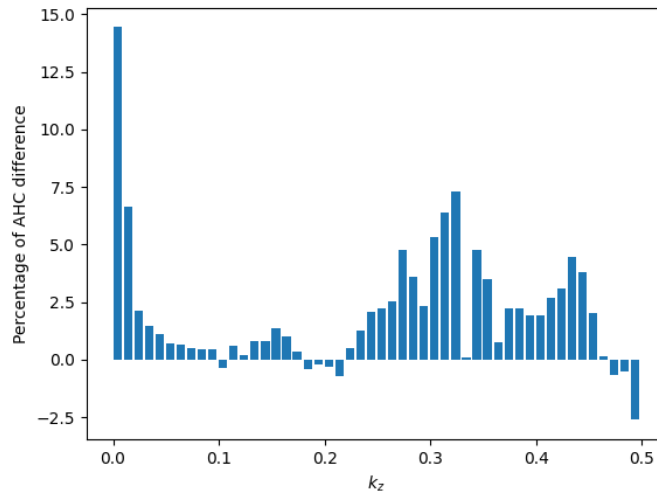


Figure 5.16.: TiMnP: Percentage of anomalous Hall conductivity difference evaluated for $M//[100]$ and $M//[001]$ for different k_z ranges

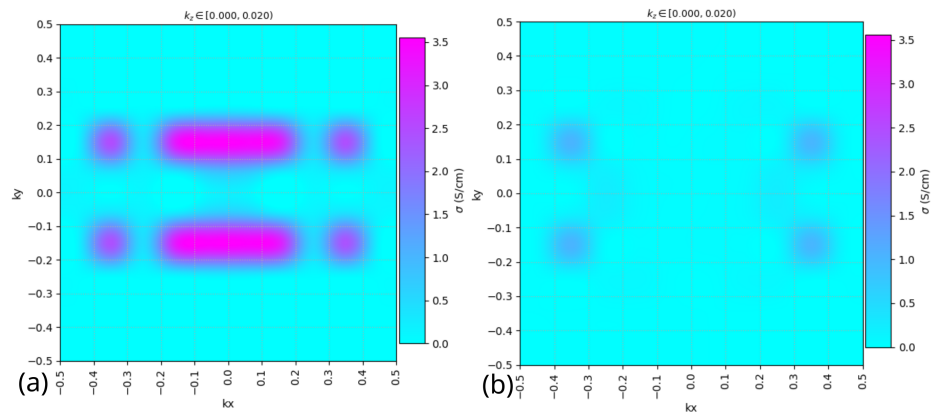


Figure 5.17.: TiMnP: (a) x-component of anomalous Hall conductivity for the specified part of the Brillouin zone for magnetization direction along $[100]$ -axis. (b) z-component of anomalous Hall conductivity for the specified part of the Brillouin zone for magnetization direction along $[001]$ -axis

5.6. Tunable anomalous Hall/Nernst conductivities

Materials with large anomalous Hall and Nernst conductivity values are desirable for being part of thermoelectric devices. There are cases though that the large values are not at the charge neutral point. In these cases, several mechanisms of tuning these values to the charge neutral point are used. In this chapter, mechanical strain and doping will be discussed as potential mechanism for tuning the anomalous Hall and Nernst conductivity values.

5.6.1. Strain induced anomalous Hall conductivity

Applying biaxial strain can potentially lead to significant changes to the anomalous Hall conductivity curve due to the changes in the crystal and band structure of the material. CoSe_4 is discussed as an example of tuning the anomalous Hall conductivity.

CoSe₄

The anomalous Hall conductivity curve of CoSe_4 exhibits a peak of almost $500\text{S}/\text{cm}$, located 5 meV above the Fermi level, as shown in Fig. 5.18(a). Therefore, an interesting question to ask is whether tuning of this peak is possible by applying biaxial strain to the system. My result demonstrate that not only the energy position of the peak is moved closer to the Fermi energy by applying biaxial strain, but also the maximum of the peak is increased from $500\text{S}/\text{cm}$ to $750\text{S}/\text{cm}$ for 1.5% compressive strain, as illustrated in Fig. 5.18. It is also noted that even though the unit cell changes due to the applied strain, the x -component of the anomalous Hall conductivity is always allowed to be finite, in contrast to the non-collinear cases discussed in the previous chapter.

5.6.2. Doping induced anomalous Hall/Nernst conductivities

Doping, being the replacement of some occupied sites of a specific element with another changes the band structure of a compound and therefore it might influence the induced anomalous Hall and Nernst conductivities. Below, I discuss Fe_3Sn doped with Mn as a tentative example.

Fe₃Sn

The first principles calculations on Fe_3Sn with the magnetization direction being parallel to [100]-axis resulted in an anomalous Hall conductivity of around $700\text{S}/\text{cm}$ as well as an anomalous Nernst conductivity of $-2.86\text{A}/\text{mK}$. A closer look at the respective curve reveals a sharp peak of $1308\text{S}/\text{cm}$ located at 60 meV below the Fermi level, therefore an interesting question is whether the position of the peak (and possible its value) can

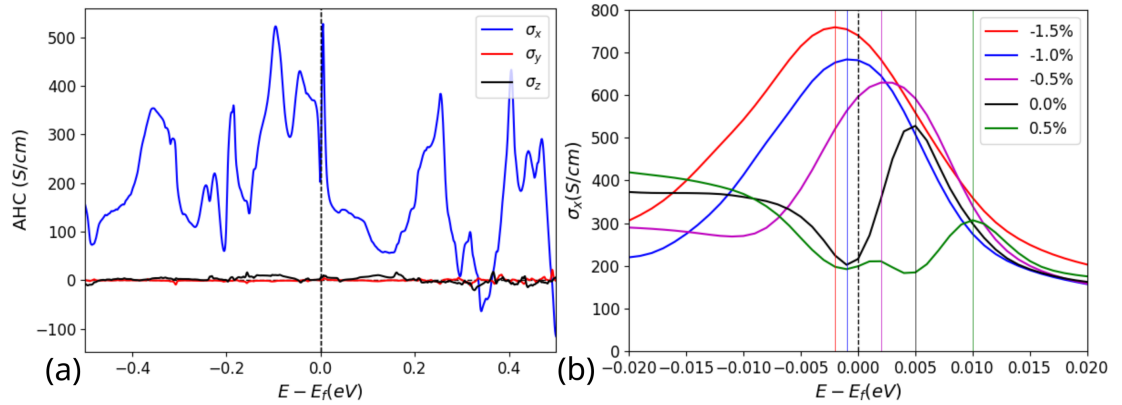


Figure 5.18.: CoSe₄, M//[100]: (a) Anomalous Hall conductivity as a function of energy. (b) x-component of anomalous Hall conductivity as a function of energy for different applied strain

be tuned by doping Mn at Fe sites. In order to investigate this possibility the compound Fe_{1-x}Mn_x)₃Sn was considered with the values of x indicating the percentage of Mn doping to the system and being within the specified range $x \in [0, 0.2]$. It is observed that for increasing values of x that corresponds to the percentage of dopant Mn, the position of the peak is moved closer to the Fermi level with the value of $x = 0.15$ making the energy of the peak and that of the Fermi energy practically coincide (see Fig. 5.19(a)). It is also noted that for $0.0 < x < 0.15$ the energy position of the peak is smaller than that of the Fermi level but for $x > 0.15$ the energy of the peak becomes larger. The outcome of this observation is the sign change of the anomalous Nernst conductivity due to the opposite slope of the peak, as illustrated in Fig. 5.19(b). Therefore, with Mn doping of Fe₃Sn, tuning of the anomalous Hall conductivity curve has been succeeded that corresponds to change of the anomalous Nernst conductivity sign, making Fe₃Sn interesting for potential spintronics applications.

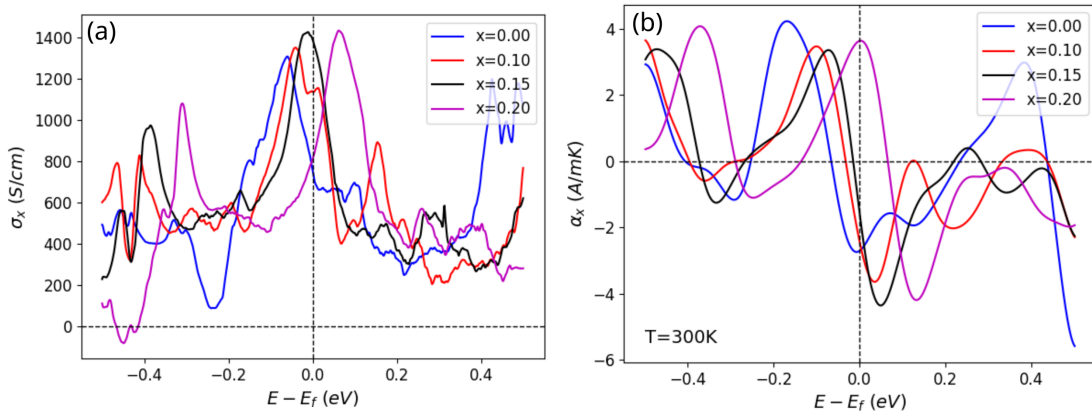


Figure 5.19.: Fe_3Sn , $M//[100]$: (a) The x-component ($\sigma_x = \sigma_{yz}$) of the full anomalous Hall conductivity as a function of energy for different doping concentrations x of $(\text{Fe}_{1-x}\text{Mn}_x)_3\text{Sn}$ (b) The x-component ($\alpha_x = \alpha_{yz}$) of the full anomalous Nernst conductivity as a function of energy for different doping concentrations x of $(\text{Fe}_{1-x}\text{Mn}_x)_3\text{Sn}$

6. Conclusion and Outlook

To sum up, based on first principles calculations, we have obtained the anomalous Hall and anomalous Nernst conductivities for several ferromagnetic and non-collinear anti-ferromagnetic transition-metal based compounds, using an in-house developed Python scheme. We demonstrated that the large localized anomalous Hall conductivity values were attributed to the presence of Weyl nodes, nodal lines and extended small gap areas that could be tuned in respect to the Fermi energy by either magnetization direction manipulations or by applied perturbations such as doping and biaxial strain.

The basic tool to obtain our results is the successful development of a Python scheme that links VASP, Wannier90 and Wanniertools software to construct Wannier functions for any transition metal based compound, with or without the inclusion of spin orbit interaction and with a success rate of 92%. The human intervention is minimized by automatically generating the required input files for the forthcoming steps based on the output files of the previous steps and additionally including an error handling "SMART_SEARCH" part for the automatic recognition and solution of several known errors.

Using the aforementioned automated algorithms we calculated surprisingly large anomalous Hall conductivity values. Namely, Pt₃Cr holds our record of the highest anomalous Hall conductivity, being equal to 2060 *S/cm*, while Ni₃Pt has both the second highest anomalous Hall conductivity (-2044 *S/cm*) and the highest anomalous Nernst conductivity (-7.2 *A/mK*). Detailed analysis on the transformations of the Berry curvature under the symmetry operations of the magnetic point group was performed and the shape of both anomalous Hall and Nernst conductivities tensors were extracted, offering useful insights on determining the non vanishing components prior the calculation. Our results were in complete agreement with the symmetry imposed shape of the tensors.

The origin of the anomalous Hall conductivity (and the anomalous Nernst conductivity) was investigated. The localized large anomalous Hall conductivity values were associated with the presence of also localized Weyl nodes and nodal lines in the Brillouin zone, with the most characteristic example being the ferromagnetic MnZn, in which, 73% of the total anomalous Hall conductivity value was originating from the vicinity of nodal rings, occupying less than 10% of the whole Brillouin zone. In contrast, spread anomalous Hall conductivity peaks were associated with the presence of small gap areas which may also

include localized Weyl nodes and nodal lines, with the most characteristic example being the ferromagnetic Ni_3Pt .

Further, it is demonstrated that even in cases where the anomalous Hall conductivity is vanishing (or small) in the ground state, altering the magnetization direction can lead to enhanced anomalous Hall and Nernst conductivity values. Particular examples include the ferromagnetic Mn_5Ge_2 , where a change of more than $600\text{S}/\text{cm}$ (from $185\text{S}/\text{cm}$ to $791\text{S}/\text{cm}$) is observed for changing the magnetization direction from $M//z$ to $M//x$ and to the ferromagnet Fe_3S_4 , in which a sign change is also observed, witnessing an anomalous Hall conductivity jump of $1191\text{S}/\text{cm}$ (from $-353\text{S}/\text{cm}$ to $837\text{S}/\text{cm}$) by changing the magnetization from $M//x$ to $M//z$.

The outcome of applied perturbations such as biaxial strain and doping to the magnitude and energy position of the anomalous Hall conductivity of ferromagnetic and antiferromagnetic systems was investigated. Our results showed that such perturbations tune the energy position of the Weyl nodes that in turn tune the energy position of the anomalous Hall conductivity. Specifically, we found that for the non-collinear antiperovskite Mn_3GaN , the anomalous Hall conductivity is increased by almost $130\text{S}/\text{cm}$, when a compressive biaxial strain of 3.5% is applied and that for the ferromagnetic CoSe_4 , a much smaller compressive biaxial strain of 1%, tunes the anomalous Hall effect spike by 5meV. Utilizing doping, we were able to tune the energy position of the anomalous Hall conductivity spike, after doping Mn at Fe sites in metastable Fe_3Sn .

In conclusion, with the development of automatic algorithms, large scale calculations that can result in the increase of the record anomalous Hall and Nernst conductivities values are feasible and moreover desirable since they can be used as parts of transverse thermoelectric generation devices. Additionally, understanding the underlying mechanisms of inducing large anomalous Hall and Nernst conductivities by altering magnetization direction, applying biaxial strain and doping leads to the techniques of engineering compounds with even larger values, useful of future applications.



Appendices

A. Numerical details

In order to perform the self consistent first-principles calculations, I used the projected augmented wave (PAW) method, as implemented in VASP and the generalized gradient approximation (GGA), as parametrized by Perdew-Burke-Ernzerhof (PBE), for the exchange-correlation functional. Spin-orbit coupling was included in all calculations and additionally, an energy cutoff of $500eV$ was selected. The kmesh was set to 50 in respect to the lattice parameters for the self consistent part and to 60 for the projected density of states part. The anomalous Hall conductivity was calculated by integrating the Berry curvature in the whole Brillouin zone by using Wanniertools software and the anomalous Nernst conductivity using a Python script to perform the integration based on the formula:

$$\alpha_{ij}(T, \mu) = -\frac{1}{e} \int d\epsilon \left(\frac{\partial f}{\partial \epsilon} \right) \sigma_{ij}(0, \epsilon) \frac{\epsilon - \mu}{T} \quad (\text{A.1})$$

with e , f , μ , ϵ and T being the electron charge (without the negative sign), the Fermi-Dirac distribution function, the chemical potential, the band energy and the temperature respectively.

B. High throughput results

Tab. B.1 summarizes all calculated AHC & ANC values for two different magnetization directions (M//x and M//z) and the respective anisotropy defined by $\frac{\sigma_{x,M//[100]}}{\alpha_{x,M//[100]}}$ and $\frac{\sigma_{z,M//[001]}}{\alpha_{z,M//[001]}}$ respectively.

N	Compound	SPG	σ_x [$\frac{S}{cm}$]	α_x [$\frac{A}{m \cdot K}$]	σ_z [$\frac{S}{cm}$]	α_z [$\frac{A}{m \cdot K}$]	Anisotropy in AHC	Anisotropy in ANC
1	Cr ₃ Te ₄	12	27.58	1.06	315.96	0.52	0.09	2.05
2	Te ₁₆ Cr ₁₄	12	441.73	-1.29	291.11	-1.00	1.52	1.28
3	Se ₁₆ Cr ₁₄	12	240.75	0.22	146.16	-1.40	1.65	-0.16
4	Fe ₃ Se ₄	12	114.49	-1.47	469.53	0.04	0.24	-33.39
5	Cr ₃ Se ₄	12	301.94	0.87	-36.22	0.36	-8.34	2.46
6	Hf ₂ Co ₇	12	817.75	0.37	402.61	-0.14	2.03	-2.65
7	Mn ₆ As ₄	12	820.61	-0.03	373.57	2.46	2.20	-0.01
8	K ₄ Mn ₄ F ₁₆	14	0.00	0.00	-0.00	-0.00	-0.54	-0.24
9	C ₄ Fe ₁₀	15	703.86	-1.96	554.15	0.56	1.27	-3.48
10	Ba ₂ V ₂ S ₆	20	67.11	0.29	-12.88	0.12	-5.21	2.34
11	Se ₈ Ag ₄ Ge ₂ Mn ₂	31	-0.61	-0.02	7.70	-0.11	-0.08	0.15
12	Co ₂ Nb ₁ Sn ₁	51	-15.15	-0.59	91.57	0.17	-0.17	-3.41
13	C ₈ N ₁₂ Co ₂	58	18.70	-0.60	20.68	0.19	0.90	-3.13
14	C ₈ N ₁₂ Ni ₂	58	-0.06	-0.04	0.01	0.00	-9.30	-14.21
15	P ₄ Mn ₄	62	154.64	-0.63	160.07	-1.58	0.97	0.40
16	Mn ₄ Co ₄ Ge ₄	62	155.18	-0.85	113.56	-0.27	1.37	3.19
17	Mn ₄ Co ₄ Si ₄	62	6.31	0.79	-14.53	0.74	-0.43	1.07
18	Fe ₁₂ C ₄	62	432.26	0.82	690.77	0.67	0.63	1.22
19	Mn ₄ Co ₄ P ₄	62	408.78	0.39	-45.07	1.11	-9.07	0.35
20	Si ₄ Mn ₄ Ni ₄	62	116.73	0.43	451.49	0.61	0.26	0.71
21	Cr ₄ Ni ₄ P ₄	62	78.51	-0.24	237.27	0.14	0.33	-1.64
22	B ₄ Fe ₄	62	78.15	2.12	31.24	0.63	2.50	3.38
23	Fe ₄ Co ₄ P ₄	62	329.66	0.72	26.17	-0.08	12.60	-9.20
24	P ₄ Fe ₄	62	0.46	0.16	-48.42	-0.38	-0.01	-0.42
25	Fe ₁₂ B ₄	62	924.23	-2.96	522.07	-1.72	1.77	1.72
26	Si ₄ S ₁₆ Mn ₈	62	0.01	-0.04	0.03	-0.14	0.31	0.31
27	F ₈ K ₄ Cu ₂	64	0.06	-0.00	0.05	-0.00	1.13	0.32
28	Mn ₃ Pd ₅	65	223.49	0.19	155.85	0.17	1.43	1.12
29	Mn ₁₀ Ge ₄	72	791.05	1.77	185.03	1.52	4.28	1.17
30	P ₄ Fe ₁₂	82	238.85	-1.39	276.83	-1.63	0.86	0.85
31	Ni ₁₂ P ₄	82	12.64	0.24	-7.57	-0.02	-1.67	-10.04
32	Mn ₁ Au ₄	87	272.27	0.24	154.49	0.40	1.76	0.61
33	V ₁ Au ₄	87	1152.27	3.13	1036.60	1.11	1.11	2.83
34	Cu ₄ Fe ₄ Se ₈	112	515.61	-0.77	761.76	-3.62	0.68	0.21
35	Fe ₁ Pt ₁	123	440.96	-0.71	861.79	-0.60	0.51	1.18
36	Pt ₁ Cr ₁	123	403.08	-0.29	-105.21	0.91	-3.83	-0.32
37	Fe ₂ Ni ₂	123	313.37	0.01	153.52	-0.29	2.04	-0.05
38	Co ₂ Pt ₂	123	233.05	-4.69	79.55	-2.35	2.93	2.00
39	Fe ₂ Pd ₂	123	122.29	-0.09	290.13	-0.21	0.42	0.42
40	Mn ₄ Ga ₁₀	127	294.98	0.09	345.73	1.04	0.85	0.08
41	Rh ₁₀ Sc ₄ B ₄ Fe ₂	127	-14.85	1.23	83.92	0.05	-0.18	22.55
42	Mn ₄ Sb ₂	129	440.31	2.25	445.24	1.86	0.99	1.21
43	Al ₂ Mn ₂ Ge ₂	129	121.35	0.69	62.23	0.18	1.95	3.80
44	Si ₂ Mn ₂ Y ₂	129	-20.19	-0.84	223.91	-0.16	-0.09	5.11
45	Al ₈ Fe ₄ Y ₁	139	36.33	-3.13	327.58	-0.11	0.11	27.92
46	Y ₂ Fe ₂₄ N ₂	139	106.23	3.45	29.26	0.76	3.63	4.56
47	Tl ₂ Cu ₄ Se ₄	139	-4.99	-0.03	-1.97	-0.04	2.54	0.65

48	Rb ₂ Cr ₁ Cl ₄	139	0.15	-0.00	-7.57	-0.05	-0.02	0.00
49	S ₂ Co ₂ Tl ₁	139	43.58	-0.27	-200.52	-0.27	-0.22	1.01
50	Fe ₈ W ₈ Fe ₈ Y ₂	139	936.06	-0.72	316.07	-1.97	2.96	0.37
51	Co ₁ Sn ₁ Rh ₂	139	311.28	1.45	337.86	1.13	0.92	1.28
52	Fe ₁ Sn ₁ Rh ₂	139	-204.19	-1.23	436.68	0.48	-0.47	-2.58
53	V ₁ Pt ₃	139	314.51	-0.31	-292.64	1.27	-1.07	-0.25
54	Mn ₂ Ge ₂ Y ₁	139	83.68	0.27	266.29	0.25	0.31	1.10
55	Be ₁₂ Cr ₁	139	25.24	0.38	24.54	0.07	1.03	5.36
56	Rh ₄ Co ₂ Sb ₂	139	217.67	-0.31	87.49	-0.92	2.49	0.34
57	Rh ₄ Fe ₂ Sb ₂	139	124.62	-0.32	81.72	-1.10	1.53	0.29
58	K ₁ Co ₂ Se ₂	139	168.66	-0.08	-180.69	-0.28	-0.93	0.29
59	Mn ₁ Sb ₁ Rh ₂	139	245.36	-0.52	4.60	0.73	53.32	-0.71
60	Rb ₂ Cu ₁ F ₄	139	-1.35	0.00	-1.12	0.00	1.21	0.45
61	Se ₄ Co ₄ Tl ₂	139	106.36	0.00	-148.57	-1.33	-0.72	-0.00
62	Fe ₂ Ge ₄	140	256.17	0.02	304.81	0.39	0.84	0.04
63	Co ₄ B ₂	140	703.07	-0.15	581.86	1.23	1.21	-0.12
64	Fe ₄ B ₂	140	414.57	-0.84	483.77	-1.49	0.86	0.57
65	Te ₆ Cr ₂ Ge ₂	148	0.00	0.02	-0.00	-0.02	-0.49	-0.77
66	Si ₂ Cr ₂ Te ₆	148	-0.00	-0.02	-0.00	-0.01	1.03	2.65
67	F ₆ V ₁ Nb ₁	148	-2.75	-0.07	24.14	0.75	-0.11	-0.09
68	Ni ₁ Pt ₁ F ₆	148	-0.10	-0.00	-0.06	0.03	1.72	-0.07
69	F ₆ Pd ₁ Pt ₁	148	0.01	-0.11	6.49	-1.04	0.00	0.10
70	Mn ₁ Zn ₁ F ₆	148	0.00	-0.00	-0.04	0.03	-0.00	-0.00
71	S ₈ V ₄ Ga ₁	160	4.02	-0.02	3.93	-0.03	1.02	0.70
72	Ga ₁ Mo ₄ S ₈	160	0.05	0.01	0.37	-0.02	0.12	-0.66
73	Ga ₁ Mo ₄ Se ₈	160	-0.07	-0.00	0.26	-0.01	-0.28	0.17
74	N ₃ Fe ₆	162	436.08	0.11	190.10	0.88	2.29	0.12
75	Cr ₈ Te ₁₂	163	-163.44	-0.98	-18.91	0.56	8.64	-1.76
76	Cr ₁₀ Si ₁₂	163	-79.64	0.05	-70.59	-0.01	1.13	-6.47
77	S ₂ Ta ₁	164	-3.96	-0.00	-9.27	-0.12	0.43	0.02
78	Y ₃ Fe ₉	166	304.96	-0.64	64.59	1.92	4.72	-0.33
79	Co ₃ Sn ₂ S ₂	166	757.13	1.01	72.17	1.64	10.49	0.62
80	Tl ₂ Fe ₆ Te ₆	176	-252.63	-0.17	-77.75	-0.30	3.25	0.57
81	Se ₁₆ Nb ₈ Mn ₂	176	-34.74	-0.81	216.66	2.57	-0.16	-0.32
82	N ₂ Fe ₆	182	234.04	0.27	111.88	0.21	2.09	1.31
83	Cr ₂ Nb ₆ Si ₁₂	182	-2.26	-0.14	-53.97	-0.15	0.04	0.97
84	Si ₁₂ Mn ₂ Nb ₆	182	-12.32	0.18	-64.10	0.07	0.19	2.67
85	Se ₁₂ Ta ₄ Cr ₂ Ta ₂	182	-137.59	0.07	-195.55	-0.22	0.70	-0.34
86	Fe ₂ Ta ₆ Si ₁₂	182	-190.51	-0.35	-363.98	0.36	0.52	-0.98
87	S ₂ Cd ₂	186	-2.39	0.00	-0.21	0.01	11.17	0.27
88	Se ₂ Cd ₂	186	0.00	0.03	0.00	0.03	1.28	0.98
89	P ₃ Fe ₆	189	217.79	-0.86	-51.95	-0.71	-4.19	1.21
90	Mn ₃ As ₃ Rh ₃	189	442.21	-1.04	-143.21	1.27	-3.09	-0.82
91	Cr ₃ Ni ₃ As ₃	189	89.23	-0.36	270.38	0.62	0.33	-0.58
92	Mn ₃ P ₃ Rh ₃	189	202.71	0.26	-120.82	-0.30	-1.68	-0.89
93	Pd ₃ Cr ₃ As ₃	189	78.81	-0.43	163.64	-3.66	0.48	0.12
94	Mn ₃ Fe ₃ As ₃	189	33.99	-0.92	-177.30	0.15	-0.19	-6.21
95	Mn ₃ As ₃ Pd ₃	189	148.17	-0.91	236.86	0.68	0.63	-1.34
96	Mn ₃ Ge ₃ Pd ₃	189	463.46	-0.39	420.74	-0.98	1.10	0.40
97	Mn ₃ As ₃ Ru ₃	189	499.62	-2.28	226.23	-3.38	2.21	0.68
98	B ₂ Co ₈ Y ₂	191	554.19	-2.93	-938.76	5.83	-0.59	-0.50
99	Y ₁ Co ₅	191	1142.26	-3.84	256.80	3.33	4.45	-1.15
100	Fe ₁₁ B ₄ Y ₃	191	269.20	0.73	919.22	-2.81	0.29	-0.26
101	Y ₂ Fe ₂ Co ₆ B ₂	191	34.83	0.63	-385.88	1.18	-0.09	0.53
102	Y ₃ Co ₁₁ B ₄	191	997.23	-0.45	-201.09	1.77	4.96	-0.26
103	Y ₄ Co ₁₄ B ₆	191	716.92	2.29	-28.26	0.11	-25.37	20.85
104	Ni ₁₃ Y ₃ B ₂	191	403.96	-0.67	-264.76	-2.65	-1.53	0.25
105	Mn ₆ Sn ₆ Mg ₁	191	175.79	0.21	-6.25	-0.82	-28.14	-0.26
106	Mn ₁ B ₂	191	66.43	0.85	-107.00	0.58	-0.62	1.46
107	Y ₁ Ni ₅	191	-246.34	-0.73	113.57	0.25	-2.17	-2.87
108	Zr ₁ Mn ₆ Sn ₆	191	993.71	1.29	346.42	-0.82	2.87	-1.57
109	Mn ₁₀ Ge ₆	193	196.23	-1.18	964.93	1.69	0.20	-0.70
110	Si ₆ Fe ₁₀	193	209.47	-0.57	-8.44	-2.41	-24.82	0.24
111	Cr ₄ Te ₄	194	-521.03	0.44	-513.33	0.58	1.01	0.76
112	Y ₂ Fe ₁₇	194	374.01	-0.63	474.77	-0.96	0.79	0.66
113	Fe ₆ Ge ₂	194	417.80	-0.85	197.21	0.29	2.12	-2.94
114	Mn ₂ As ₂	194	-38.70	0.02	178.43	-1.63	-0.22	-0.02
115	Sc ₄ Fe ₈	194	213.10	-1.09	189.90	1.09	1.12	-1.00
116	Sc ₆ In ₂	194	-6.66	-0.75	-139.79	0.04	0.05	-20.09
117	Hf ₄ Fe ₈	194	284.54	0.45	415.10	2.42	0.69	0.19
118	Be ₈ Fe ₄	194	475.24	-1.00	385.15	-3.91	1.23	0.26
119	Co ₂	194	38.95	-0.13	482.78	0.05	0.08	-2.39

120	F ₆ Ni ₂ Cs ₂	194	0.06	-0.02	-0.00	0.00	-3023.06	-7987.00
121	Fe ₂ Co ₂ Ge ₂	194	-26.92	-2.25	706.25	0.85	-0.04	-2.65
122	Mn ₂ Bi ₂	194	1599.55	-1.42	849.95	2.35	1.88	-0.60
123	Mn ₂ Co ₂ Sn ₂	194	382.66	-3.65	-280.30	-3.20	-1.37	1.14
124	Mn ₂ Ga ₂ Pt ₂	194	-1081.62	-3.63	611.59	-0.97	-1.77	3.75
125	Mn ₆ Ga ₂	194	119.35	1.73	1605.63	3.91	0.07	0.44
126	Zr ₄ Fe ₂ V ₆	194	-27.76	1.02	-205.58	0.28	0.14	3.59
127	Fe ₆ Sn ₂	194	802.88	-1.04	822.55	-3.13	0.98	0.33
128	Mg ₄ Co ₈	194	-871.05	1.02	204.33	0.07	-4.26	14.89
129	Fe ₄ Ge ₂	194	-464.24	-0.01	1182.00	-2.35	-0.39	0.00
130	Mn ₂ Ni ₂ Ge ₂	194	213.35	0.65	90.35	1.63	2.36	0.40
131	Nb ₄ Fe ₈	194	1212.37	4.01	1029.89	-1.23	1.18	-3.25
132	Cl ₆ Rb ₂ Fe ₂	194	-4.69	-0.66	0.81	0.05	-5.81	-13.57
133	Ti ₄ Fe ₈	194	821.15	3.21	96.72	5.68	8.49	0.56
134	Al ₆ Fe ₂ Y ₄	194	534.80	-1.07	33.74	1.81	15.85	-0.59
135	Mn ₄ Si ₄	198	147.21	-0.76	138.30	-0.73	1.06	1.05
136	Fe ₄ Ge ₄	198	121.17	0.00	147.02	0.01	0.82	0.10
137	Fe ₄ Sb ₄ Pt ₄	198	208.60	-1.72	177.74	-1.63	1.17	1.05
138	Fe ₄ Si ₄	198	75.57	0.12	14.09	0.16	5.36	0.70
139	Na ₁ Fe ₄ Sb ₁₂	204	617.22	-3.18	850.48	-2.78	0.73	1.14
140	S ₈ Co ₄	205	-365.66	2.15	-351.35	2.19	1.04	0.98
141	Co ₄ Se ₈	205	510.92	-1.22	196.23	-1.59	2.60	0.77
142	Se ₈ Ni ₄	205	1.42	-0.08	10.07	0.07	0.14	-1.23
143	Pd ₈ Mo ₁₂ N ₄	213	-3.28	-0.07	146.90	0.14	-0.02	-0.49
144	Mn ₁ Ni ₁ Sb ₁	216	164.64	0.09	164.65	0.09	1.00	1.06
145	Ti ₁ Co ₁ Sn ₁	216	150.77	0.11	149.37	0.18	1.01	0.65
146	Mn ₁ Co ₁ Sb ₁	216	2.36	-0.39	20.23	-0.30	0.12	1.31
147	Mn ₁ Sn ₁ Pt ₁	216	138.68	0.85	-42.11	1.06	-3.29	0.80
148	Mn ₁ Sb ₁ Au ₁	216	397.47	0.45	424.26	0.09	0.94	5.30
149	Mn ₁ Sb ₁ Pt ₁	216	81.37	0.50	143.12	0.39	0.57	1.29
150	V ₁ Co ₁ Sb ₁	216	103.27	0.40	59.07	0.51	1.75	0.77
151	Mn ₁ Sn ₁ Au ₁	216	-58.80	0.18	-50.28	0.60	1.17	0.30
152	Bi ₈ Mn ₁₆ Ni ₄	216	321.82	-1.63	329.89	-1.09	0.98	1.49
153	Al ₄ Cr ₄ Fe ₄ Co ₄	216	-250.90	-0.03	-129.23	0.61	1.94	-0.04
154	Cr ₄ Cu ₁ Se ₈ In ₁	216	36.00	-1.14	57.99	-1.10	0.62	1.03
155	Rh ₄ Mn ₄ Sn ₄	216	49.09	0.81	28.53	0.81	1.72	0.99
156	Mn ₁ Fe ₁ Co ₁ Ge ₁	216	23.56	1.27	21.73	1.18	1.08	1.07
157	Mn ₂ Co ₁ Sb ₁	216	29.20	-0.11	28.58	-0.07	1.02	1.73
158	Mn ₂ Fe ₁ C ₆ N ₆	216	0.00	0.19	0.00	-0.40	0.40	-0.49
159	Zr ₁ In ₁ Ni ₄	216	335.04	-0.02	363.00	-0.27	0.92	0.09
160	Ni ₅ Zr ₁	216	-220.27	1.50	-202.99	1.76	1.09	0.85
161	As ₁₂	220	891.79	1.24	536.22	2.98	1.66	0.42
162	P ₁₂	220	0.00	-1.08	0.00	-1.08	2.69	1.00
163	Al ₁ Ni ₃	221	206.19	-2.74	208.74	-2.15	0.99	1.28
164	Fe ₁ Pt ₃	221	-318.04	-1.83	-318.40	-1.73	1.00	1.06
165	Cr ₁ Pt ₃	221	2060.08	-0.10	2040.21	-0.24	1.01	0.42
166	Cr ₁ Fe ₁	221	-302.83	-1.59	-310.86	-1.62	0.97	0.98
167	Fe ₁ Ni ₃	221	-127.38	0.02	-80.97	-0.01	1.57	-1.17
168	Fe ₁ Rh ₁	221	809.19	-0.13	794.39	-0.12	1.02	1.05
169	Ga ₁ Co ₁	221	-9.13	0.08	-16.84	0.08	0.54	0.95
170	Fe ₁ Pd ₃	221	-201.61	1.56	-217.08	1.61	0.93	0.97
171	Mn ₁ Pt ₃	221	1342.88	-4.06	1471.55	-4.58	0.91	0.89
172	Mn ₁ Zn ₁	221	339.81	-1.64	1059.69	-0.78	0.32	2.10
173	Fe ₄ N ₁	221	631.04	0.45	557.85	-0.60	1.13	-0.75
174	Mn ₁ Ni ₃	221	45.87	0.94	43.37	0.76	1.06	1.23
175	Mn ₄ N ₁	221	119.34	-0.04	884.35	1.93	0.13	-0.02
176	V ₁ Fe ₁	221	61.81	-2.93	59.98	-1.80	1.03	1.62
177	Co ₁ Pt ₃	221	-978.05	-0.50	-933.11	-0.58	1.05	0.87
178	Mn ₃ Ge ₁	221	-130.51	4.78	-57.15	4.93	2.28	0.97
179	C ₁ Mn ₃ In ₁	221	-52.54	-0.98	-157.79	0.63	0.33	-1.57
180	Ni ₃ Pt ₁	221	-2044.52	-7.24	-2051.84	-7.29	1.00	0.99
181	Ti ₁ Co ₃	221	-125.38	-1.46	-139.69	-1.61	0.90	0.90
182	B ₆ Ba ₁	221	-0.80	0.01	51.03	-0.12	-0.02	-0.07
183	C ₁ Al ₁ Mn ₃	221	181.58	-0.48	180.17	-0.50	1.01	0.96
184	Ni ₃ Al ₁ C ₁	221	-4.68	0.02	-3.32	0.04	1.41	0.56
185	Mn ₁ Ni ₂ Ga ₁	225	9.84	0.41	-41.73	0.46	-0.24	0.89
186	Mn ₁ Ni ₂ Sn ₁	225	-83.45	-0.83	-60.95	-0.80	1.37	1.03
187	Ni ₁	225	-2038.91	0.99	-2444.07	0.76	0.83	1.29
188	Mn ₁ Ni ₂ In ₁	225	-50.86	0.20	-60.36	-0.03	0.84	-7.38
189	Mn ₁ Ni ₂ Sb ₁	225	-60.65	0.06	-86.11	0.04	0.70	1.52
190	Mn ₁ Pd ₂ Sn ₁	225	110.43	0.86	122.81	0.89	0.90	0.97
191	Ti ₁ Co ₂ Sn ₁	225	130.36	0.04	134.33	0.03	0.97	1.34

192	Al ₁ Fe ₃	225	216.26	-1.54	218.06	-1.65	0.99	0.93
193	Mn ₁ Co ₂ Sn ₁	225	180.14	-0.00	200.08	-0.00	0.90	0.62
194	Al ₁ Ti ₁ Co ₂	225	112.53	-0.31	77.67	-0.56	1.45	0.56
195	Ga ₁ Fe ₃	225	743.55	-1.71	797.26	-1.65	0.93	1.04
196	Fe ₃ Si ₁	225	341.40	-0.28	331.33	-0.11	1.03	2.48
197	Mn ₁ Rh ₂ Sn ₁	225	293.61	0.46	398.36	0.48	0.74	0.95
198	Mn ₁ Pd ₂ Sb ₁	225	376.96	-0.76	314.12	-0.90	1.20	0.84
199	Mn ₁ Al ₁ Cu ₂	225	185.04	-0.18	168.81	-0.10	1.10	1.79
200	Fe ₁ Co ₂ Si ₁	225	-138.85	-4.85	-509.80	-6.69	0.27	0.72
201	Al ₁ V ₁ Fe ₂	225	8.61	0.06	8.48	0.08	1.02	0.73
202	Fe ₂₃ Y ₆	225	231.13	1.68	272.00	1.03	0.85	1.62
203	In ₂ Au ₁	225	3.80	-0.01	84.77	0.00	0.04	-4.93
204	Mn ₆ Cu ₈ Bi ₈	225	714.73	-0.10	718.54	1.02	0.99	-0.10
205	V ₁ Co ₂ Sn ₁	225	108.60	-1.23	-79.60	-1.42	-1.36	0.86
206	Al ₁ Co ₂ Zr ₁	225	126.80	-0.34	157.87	-0.44	0.80	0.77
207	Zr ₁ Co ₂ Sn ₁	225	75.28	0.01	83.65	0.01	0.90	1.16
208	Al ₁ Mn ₁ Au ₂	225	84.91	-0.16	80.77	-0.53	1.05	0.30
209	Al ₁ Cr ₁ Co ₂	225	815.94	1.17	657.72	1.34	1.24	0.87
210	Fe ₈ Cr ₄ Si ₄	225	720.50	-2.33	892.13	-2.83	0.81	0.82
211	Mn ₄ Sn ₄ Cu ₈	225	198.14	0.40	190.94	0.31	1.04	1.26
212	Ga ₁ Fe ₂ Ni ₁	225	1239.52	-1.49	1487.77	-2.33	0.83	0.64
213	Fe ₄ Ru ₈ Si ₄	225	1044.72	-1.12	1037.94	-1.67	1.01	0.67
214	Co ₂ Sn ₁ Hf ₁	225	43.87	0.58	69.77	0.43	0.63	1.35
215	Mn ₁ Co ₂ Si ₁	225	194.27	-0.50	166.22	-0.55	1.17	0.90
216	Al ₁ Mn ₁ Ni ₂	225	-162.87	0.91	-128.55	0.80	1.27	1.13
217	Mn ₁ Ni ₂ Ge ₁	225	110.38	-1.05	104.19	-1.07	1.06	0.99
218	Mn ₁ Pd ₂ Ge ₁	225	289.20	0.35	294.26	0.45	0.98	0.76
219	Mn ₁ Rh ₂ Pb ₁	225	-119.31	-0.93	-297.19	-1.09	0.40	0.86
220	Ni ₁ Ge ₁ Rh ₂	225	-0.00	0.00	-0.07	0.00	0.01	0.14
221	Ti ₁ Co ₂ Ga ₁	225	146.02	-0.68	149.46	-0.83	0.98	0.81
222	Al ₁ Ti ₁ Fe ₂	225	72.93	-0.28	69.22	-0.24	1.05	1.16
223	Al ₁ V ₁ Mn ₂	225	59.25	-0.47	70.56	-0.40	0.84	1.17
224	Cr ₁ Ga ₁ Co ₂	225	618.69	1.64	654.20	1.81	0.95	0.91
225	Al ₁ Cr ₁ Fe ₂	225	-120.08	-0.88	103.73	0.11	-1.16	-8.21
226	Cr ₁ Fe ₂ Ga ₁	225	-166.65	2.76	-138.68	1.03	1.20	2.67
227	N ₂ Cr ₂	225	-171.32	-1.69	-123.82	-0.71	1.38	2.39
228	Al ₁ Cr ₁ Ni ₂	225	-498.01	-1.06	-512.11	-1.00	0.97	1.06
229	Mn ₁ Cu ₂ In ₁	225	57.88	0.34	41.52	0.49	1.39	0.69
230	Fe ₁ Sn ₁ Ru ₂	225	201.04	-1.22	204.57	-0.99	0.98	1.23
231	Ga ₁ Fe ₂ Co ₁	225	-227.40	2.19	-208.68	3.28	1.09	0.67
232	Al ₁ Co ₂ Hf ₁	225	216.34	-0.24	250.96	-0.17	0.86	1.42
233	Mn ₁ Ga ₂ Co ₁	225	32.25	-1.33	120.81	-0.72	0.27	1.84
234	Mn ₁ Co ₂ Ge ₁	225	307.22	-0.11	306.85	-0.12	1.00	0.93
235	Mn ₁ Co ₂ Sb ₁	225	-7.43	-0.97	-11.80	-0.98	0.63	0.99
236	Al ₁ Mn ₁ Fe ₂	225	743.00	1.74	731.70	1.52	1.02	1.14
237	Mn ₁ Fe ₂ Si ₁	225	118.95	0.68	163.44	0.75	0.73	0.91
238	Al ₁ Co ₂ Nb ₁	225	28.90	0.17	31.29	0.23	0.92	0.74
239	Ni ₁ Rh ₂ Sn ₁	225	20.26	-9.11	105.76	-9.06	0.19	1.01
240	Sc ₁ Co ₂ Sn ₁	225	129.93	-0.41	137.74	-0.38	0.94	1.08
241	Sr ₈ Ru ₄	225	-88.51	1.19	-106.15	1.00	0.83	1.18
242	Al ₁ Co ₂ Ta ₁	225	-76.07	0.75	-72.56	0.70	1.05	1.06
243	Ti ₁ Co ₂ Si ₁	225	151.41	0.58	113.08	0.36	1.34	1.63
244	Al ₁ V ₁ Co ₂	225	151.02	0.15	167.09	0.10	0.90	1.44
245	V ₁ Co ₂ Ga ₁	225	142.59	0.06	140.34	0.03	1.02	2.39
246	Si ₁ V ₁ Co ₂	225	309.01	-1.06	284.71	-1.40	1.09	0.76
247	Si ₁ V ₁ Fe ₂	225	39.61	1.00	35.00	0.78	1.13	1.28
248	V ₁ Fe ₂ Sn ₁	225	330.15	0.34	307.39	1.03	1.07	0.33
249	Mn ₂ V ₁ Ga ₁	225	63.89	1.02	109.90	1.06	0.58	0.96
250	Mn ₂ Sn ₁ W ₁	225	49.45	-4.99	708.77	-2.23	0.07	2.24
251	Zn ₄ Zr ₂	227	-165.25	-0.47	-181.43	-0.33	0.91	1.40
252	Y ₂ Fe ₄	227	4.82	-0.97	41.57	-0.75	0.12	1.29
253	Cr ₄ Se ₈ Cd ₂	227	0.00	-0.83	0.00	-0.79	70.09	1.05
254	S ₈ Cr ₄ Cd ₂	227	-0.83	0.10	-0.63	0.17	1.32	0.59
255	Fe ₄ Zr ₂	227	215.31	0.90	237.03	1.10	0.91	0.82
256	Cr ₄ Cu ₂ Se ₈	227	28.35	-0.41	13.44	-0.46	2.11	0.89
257	S ₈ Cr ₄ Fe ₂	227	-280.51	2.08	-51.36	2.40	5.46	0.87
258	Cr ₄ Se ₈ Hg ₂	227	137.25	-0.91	30.13	-0.76	4.55	1.20
259	Cr ₄ Cu ₂ Te ₈	227	-47.44	-0.35	-145.88	-0.46	0.33	0.75
260	S ₈ Cr ₄ Cu ₂	227	-24.72	-0.98	-40.91	-1.07	0.60	0.91
261	Co ₄ Zr ₂	227	-147.93	1.10	-163.83	1.42	0.90	0.78
262	S ₈ Cr ₄ Fe ₁ Cu ₁	227	-420.86	0.11	-140.60	0.27	2.99	0.39
263	Fe ₄ F ₁₂	227	0.00	0.05	0.03	-0.00	0.00	-20.80

264	Fe ₆ S ₈	227	-353.69	2.47	837.63	-2.56	-0.42	-0.97
265	Y ₂ Co ₄	227	662.69	-1.05	855.03	-1.32	0.78	0.80
266	Fe ₁	229	862.83	-0.69	833.57	-0.92	1.04	0.76

Table B.1.: AHC at T=0K and ANC at T=300K for the two magnetization directions (σ_x, α_x for $\mathbf{M} // \mathbf{x}$ and σ_z, α_z for $\mathbf{M} // \mathbf{z}$) and the anisotropy of each ferromagnetic compound. Values highlighted in blue signify the most interesting cases while the ones in green exhibit the largest anisotropy in either direction.

Bibliography

- [1] NP Armitage, EJ Mele, and Ashvin Vishwanath. “Weyl and Dirac semimetals in three-dimensional solids”. In: *Reviews of Modern Physics* 90.1 (2018), p. 015001.
- [2] NW Ashcroft, ND Mermin, and S Rodriguez. “Solid State Physics, vol. 46”. In: *American Association of Physics Teachers* (1978).
- [3] GB Bachelet, DM Ceperley, and MGB Chiocchetti. “Novel pseudo-Hamiltonian for quantum Monte Carlo simulations”. In: *Physical review letters* 62.18 (1989), p. 2088.
- [4] P Bagno, O Jepsen, and O Gunnarsson. “Ground-state properties of third-row elements with nonlocal density functionals”. In: *Physical Review B* 40.3 (1989), p. 1997.
- [5] Franco Bassani et al. *Highlights of condensed-matter theory*. Vol. 89. North Holland, 1985.
- [6] AD Becke, A Savin, and H Stoll. “Extension of the local-spin-density exchange-correlation approximation to multiplet states”. In: *Theoretica chimica acta* 91.3 (1995), pp. 147–156.
- [7] Axel D Becke. “Density functional calculations of molecular bond energies”. In: *The Journal of Chemical Physics* 84.8 (1986), pp. 4524–4529.
- [8] Axel D Becke. “Density-functional exchange-energy approximation with correct asymptotic behavior”. In: *Physical review A* 38.6 (1988), p. 3098.
- [9] Ilya Belopolski et al. “Discovery of topological Weyl fermion lines and drumhead surface states in a room temperature magnet”. In: *Science* 365.6459 (2019), pp. 1278–1281.
- [10] Wladimir A Benalcazar, B Andrei Bernevig, and Taylor L Hughes. “Quantized electric multipole insulators”. In: *Science* 357.6346 (2017), pp. 61–66.
- [11] Luc Berger. “Side-jump mechanism for the Hall effect of ferromagnets”. In: *Physical Review B* 2.11 (1970), p. 4559.

-
- [12] Michael Victor Berry. “Quantal phase factors accompanying adiabatic changes”. In: *Proceedings of the Royal Society of London. A. Mathematical and Physical Sciences* 392.1802 (1984), pp. 45–57.
- [13] David Boldrin et al. “Anomalous Hall effect in noncollinear antiferromagnetic Mn₃NiN thin films”. In: *Physical Review Materials* 3.9 (2019), p. 094409.
- [14] Sergey Borisenko et al. “Experimental realization of a three-dimensional Dirac semimetal”. In: *Physical review letters* 113.2 (2014), p. 027603.
- [15] Max Born and Vladimir Fock. “Beweis des adiabatsatzes”. In: *Zeitschrift für Physik* 51.3 (1928), pp. 165–180.
- [16] Max Born and Robert Oppenheimer. “Zur quantentheorie der molekeln”. In: *Annalen der physik* 389.20 (1927), pp. 457–484.
- [17] W Borrmann and P Fulde. “On the theory of band gaps in semiconductors”. In: *EPL (Europhysics Letters)* 2.6 (1986), p. 471.
- [18] U Brandt and Ch Mielsch. “Thermodynamics and correlation functions of the Falicov-Kimball model in large dimensions”. In: *Zeitschrift für Physik B Condensed Matter* 75.3 (1989), pp. 365–370.
- [19] DM Broun. “What lies beneath the dome?” In: *Nature Physics* 4.3 (2008), pp. 170–172.
- [20] P Bruno, VK Dugaev, and M Taillefumier. “Topological Hall effect and Berry phase in magnetic nanostructures”. In: *Physical review letters* 93.9 (2004), p. 096806.
- [21] AA Burkov, MD Hook, and Leon Balents. “Topological nodal semimetals”. In: *Physical Review B* 84.23 (2011), p. 235126.
- [22] K Capelle and EKH Gross. “Spin-density functionals from current-density functional theory and vice versa: A road towards new approximations”. In: *Physical review letters* 78.10 (1997), p. 1872.
- [23] AE Carlsson. “Simplified electrostatic model for band-gap underestimates in the local-density approximation”. In: *Physical Review B* 31.8 (1985), p. 5178.
- [24] David M Ceperley and Berni J Alder. “Ground state of the electron gas by a stochastic method”. In: *Physical review letters* 45.7 (1980), p. 566.
- [25] Daniel Champier. “Thermoelectric generators: A review of applications”. In: *Energy Conversion and Management* 140 (2017), pp. 167–181.
- [26] Y-H Chan et al. “Ca₃P₂ and other topological semimetals with line nodes and drumhead surface states”. In: *Physical Review B* 93.20 (2016), p. 205132.

-
-
- [27] Hua Chen, Qian Niu, and Allan H MacDonald. “Anomalous Hall effect arising from noncollinear antiferromagnetism”. In: *Physical review letters* 112.1 (2014), p. 017205.
- [28] Aron J Cohen, Paula Mori-Sánchez, and Weitao Yang. “Challenges for density functional theory”. In: *Chemical reviews* 112.1 (2012), pp. 289–320.
- [29] Lee A Cole and JP Perdew. “Calculated electron affinities of the elements”. In: *Physical Review A* 25.3 (1982), p. 1265.
- [30] Jacques Des Cloizeaux. “Orthogonal orbitals and generalized Wannier functions”. In: *Physical Review* 129.2 (1963), p. 554.
- [31] Reiner M Dreizler and João da Providência. *Density functional methods in physics*. Vol. 123. Springer Science & Business Media, 2013.
- [32] Maxim Dzero et al. “Topological kondo insulators”. In: *Physical review letters* 104.10 (2010), p. 106408.
- [33] E Engel. “Relativistic Electronic Structure Theory, Part 1. Fundamentals”. In: *by R. Schwerdtfeger, Elsevier* (2002).
- [34] H Eschrig, G Seifert, and P Ziesche. “Current density functional theory of quantum electrodynamics”. In: *Solid state communications* 56.9 (1985), pp. 777–780.
- [35] Zhong Fang et al. “The anomalous Hall effect and magnetic monopoles in momentum space”. In: *Science* 302.5642 (2003), pp. 92–95.
- [36] Zexin Feng et al. “Observation of the anomalous Hall effect in a collinear antiferromagnet”. In: *arXiv preprint arXiv:2002.08712* (2020).
- [37] Enrico Fermi. “Un metodo statistico per la determinazione di alcune priorietà dell’atome”. In: *Rend. Accad. Naz. Lincei* 6.602-607 (1927), p. 32.
- [38] Michael Filatov and Walter Thiel. “Exchange-correlation density functional beyond the gradient approximation”. In: *Physical Review A* 57.1 (1998), p. 189.
- [39] Vladimir Fock. “Näherungsmethode zur Lösung des quantenmechanischen Mehrkörperproblems”. In: *Zeitschrift für Physik* 61.1 (1930), pp. 126–148.
- [40] D Fruchart and E F. Bertaut. “Magnetic studies of the metallic perovskite-type compounds of manganese”. In: *Journal of the physical society of Japan* 44.3 (1978), pp. 781–791.
- [41] Liang Fu. “Topological crystalline insulators”. In: *Physical Review Letters* 106.10 (2011), p. 106802.

-
- [42] Liang Fu and Charles L Kane. “Topological insulators with inversion symmetry”. In: *Physical Review B* 76.4 (2007), p. 045302.
- [43] Kevin F Garrity and Kamal Choudhary. “Database of Wannier tight-binding Hamiltonians using high-throughput density functional theory”. In: *Scientific data* 8.1 (2021), pp. 1–10.
- [44] VL Ginzburg and LD Landau. “On the theory of superconductivity”. In: *Zh. Eksp. Teor. Fiz.* 20 (1950), p. 1064.
- [45] H Julian Goldsmid et al. *Introduction to thermoelectricity*. Vol. 121. Springer, 2010.
- [46] HJ Goldsmid. “The electrical conductivity and thermoelectric power of bismuth telluride”. In: *Proceedings of the Physical Society (1958-1967)* 71.4 (1958), p. 633.
- [47] EKV Gross, CA Ullrich, and UJ Gossmann. “In Density Functional Theory; Gross, EKV; Dreizler, RM, Eds”. In: *NATO Advanced Study Institute Series B: Physics*. 1995, pp. 149–171.
- [48] Z Guguchia et al. “Tunable anomalous Hall conductivity through volume-wise magnetic competition in a topological kagome magnet”. In: *Nature communications* 11.1 (2020), pp. 1–9.
- [49] Satya N Guin et al. “Anomalous Nernst effect beyond the magnetization scaling relation in the ferromagnetic Heusler compound Co₂MnGa”. In: *NPG Asia Materials* 11.1 (2019), pp. 1–9.
- [50] O Gunnarsson, BI Lundqvist, and JW Wilkins. “Contribution to the cohesive energy of simple metals: Spin-dependent effect”. In: *Physical Review B* 10.4 (1974), p. 1319.
- [51] Guang-Yu Guo and Tzu-Cheng Wang. “Large anomalous Nernst and spin Nernst effects in the noncollinear antiferromagnets Mn₃X (X= Sn, Ge, Ga)”. In: *Physical Review B* 96.22 (2017), p. 224415.
- [52] Lukai Guo and Qing Lu. “Potentials of piezoelectric and thermoelectric technologies for harvesting energy from pavements”. In: *Renewable and Sustainable Energy Reviews* 72 (2017), pp. 761–773.
- [53] Xin-Ge Guo et al. “Magnetically driven negative thermal expansion in antiperovskite Ga_{1-x}Mn_xNO. 8Mn₃ (0.1 ≤ x ≤ 0.3)”. In: *Applied Physics Letters* 107.20 (2015), p. 202406.
- [54] Gautam Gurung et al. “Anomalous Hall conductivity of noncollinear magnetic antiperovskites”. In: *Physical Review Materials* 3.4 (2019), p. 044409.

-
-
- [55] Philipp Haas, Fabien Tran, and Peter Blaha. “Calculation of the lattice constant of solids with semilocal functionals”. In: *Physical Review B* 79.8 (2009), p. 085104.
- [56] Jürgen Hafner. “Ab-initio simulations of materials using VASP: Density-functional theory and beyond”. In: *Journal of computational chemistry* 29.13 (2008), pp. 2044–2078.
- [57] Gábor B Halász and Leon Balents. “Time-reversal invariant realization of the Weyl semimetal phase”. In: *Physical Review B* 85.3 (2012), p. 035103.
- [58] F Duncan M Haldane. “Model for a quantum Hall effect without Landau levels: Condensed-matter realization of the" parity anomaly"”. In: *Physical review letters* 61.18 (1988), p. 2015.
- [59] FDM Haldane. “Berry curvature on the fermi surface: Anomalous hall effect as a topological fermi-liquid property”. In: *Physical review letters* 93.20 (2004), p. 206602.
- [60] Edwin H Hall et al. “On a new action of the magnet on electric currents”. In: *American Journal of Mathematics* 2.3 (1879), pp. 287–292.
- [61] EH Hall. “On the possibility of transverse currents in ferromagnets”. In: *Philos. Mag* 12 (1881), pp. 157–172.
- [62] Maciej Haras and Thomas Skotnicki. “Thermoelectricity for IoT—A review”. In: *Nano Energy* 54 (2018), pp. 461–476.
- [63] DR Hartree. “Mathematical Proceedings of the Cambridge Philosophical Society”. In: *The Wave Mechanics of an Atom with a Non-Coulomb Central Field. Part II. Some Results and Discussion* 24.01 (1928), p. 111.
- [64] K Hasegawa et al. “Material dependence of anomalous Nernst effect in perpendicularly magnetized ordered-alloy thin films”. In: *Applied Physics Letters* 106.25 (2015), p. 252405.
- [65] Ran He, Gabi Schierning, and Kornelius Nielsch. “Thermoelectric devices: a review of devices, architectures, and contact optimization”. In: *Advanced Materials Technologies* 3.4 (2018), p. 1700256.
- [66] T He et al. “Superconductivity in the non-oxide perovskite MgCNi₃”. In: *Nature* 411.6833 (2001), pp. 54–56.
- [67] Lars Hedin. “New method for calculating the one-particle Green’s function with application to the electron-gas problem”. In: *Physical Review* 139.3A (1965), A796.
- [68] Lars Hedin. “On correlation effects in electron spectroscopies and the GW approximation”. In: *Journal of Physics: Condensed Matter* 11.42 (1999), R489.

-
- [69] Yuji Hirokane et al. “Longitudinal and transverse thermoelectric transport in MnSi”. In: *Physical Review B* 93.1 (2016), p. 014436.
- [70] Pierre Hohenberg and Walter Kohn. “Inhomogeneous electron gas”. In: *Physical review* 136.3B (1964), B864.
- [71] Rongjin Huang et al. “Low-temperature negative thermal expansion of the antiperovskite manganese nitride Mn₃CuN codoped with Ge and Si”. In: *Applied Physics Letters* 93.8 (2008), p. 081902.
- [72] SX Huang and CL Chien. “Extended skyrmion phase in epitaxial FeGe (111) thin films”. In: *Physical review letters* 108.26 (2012), p. 267201.
- [73] Erika Hult et al. “Density functional for van der Waals forces at surfaces”. In: *Physical review letters* 77.10 (1996), p. 2029.
- [74] Vu Thi Ngoc Huyen et al. “Topology analysis for anomalous Hall effect in the noncollinear antiferromagnetic states of Mn₃AN (A= Ni, Cu, Zn, Ga, Ge, Pd, In, Sn, Ir, Pt)”. In: *Physical Review B* 100.9 (2019), p. 094426.
- [75] Mark S Hybertsen and Steven G Louie. “Spin-orbit splitting in semiconductors and insulators from the ab initio pseudopotential”. In: *Physical Review B* 34.4 (1986), p. 2920.
- [76] Muhammad Ikhlas et al. “Large anomalous Nernst effect at room temperature in a chiral antiferromagnet”. In: *Nature Physics* 13.11 (2017), pp. 1085–1090.
- [77] Masatoshi Imada, Atsushi Fujimori, and Yoshinori Tokura. “Metal-insulator transitions”. In: *Reviews of modern physics* 70.4 (1998), p. 1039.
- [78] Kurt A Johnson and NW Ashcroft. “Corrections to density-functional theory band gaps”. In: *Physical Review B* 58.23 (1998), p. 15548.
- [79] Robert O Jones and Olle Gunnarsson. “The density functional formalism, its applications and prospects”. In: *Reviews of Modern Physics* 61.3 (1989), p. 689.
- [80] T Jungwirth, Qian Niu, and AH MacDonald. “Anomalous Hall effect in ferromagnetic semiconductors”. In: *Physical review letters* 88.20 (2002), p. 207208.
- [81] K Kamishima et al. “Giant magnetoresistance in the intermetallic compound Mn₃GaC”. In: *Physical Review B* 63.2 (2000), p. 024426.
- [82] N Kanazawa et al. “Large topological Hall effect in a short-period helimagnet MnGe”. In: *Physical review letters* 106.15 (2011), p. 156603.
- [83] Charles L Kane and Eugene J Mele. “Z₂ topological order and the quantum spin Hall effect”. In: *Physical review letters* 95.14 (2005), p. 146802.

-
- [84] Robert Karplus and JM Luttinger. “Hall effect in ferromagnetics”. In: *Physical Review* 95.5 (1954), p. 1154.
- [85] Kyoo Kim et al. “Large anomalous Hall current induced by topological nodal lines in a ferromagnetic van der Waals semimetal”. In: *Nature materials* 17.9 (2018), pp. 794–799.
- [86] Youngkuk Kim et al. “Dirac line nodes in inversion-symmetric crystals”. In: *Physical review letters* 115.3 (2015), p. 036806.
- [87] Naoki Kiyohara, Takahiro Tomita, and Satoru Nakatsuji. “Giant anomalous Hall effect in the chiral antiferromagnet Mn₃Ge”. In: *Physical Review Applied* 5.6 (2016), p. 064009.
- [88] K v Klitzing, Gerhard Dorda, and Michael Pepper. “New method for high-accuracy determination of the fine-structure constant based on quantized Hall resistance”. In: *Physical review letters* 45.6 (1980), p. 494.
- [89] Wolfram Koch and Max C Holthausen. *A chemist’s guide to density functional theory*. John Wiley & Sons, 2015.
- [90] DD Koelling and BN Harmon. “A technique for relativistic spin-polarised calculations”. In: *Journal of Physics C: Solid State Physics* 10.16 (1977), p. 3107.
- [91] Walter Kohn. “Analytic properties of Bloch waves and Wannier functions”. In: *Physical Review* 115.4 (1959), p. 809.
- [92] Walter Kohn and Lu Jeu Sham. “Self-consistent equations including exchange and correlation effects”. In: *Physical review* 140.4A (1965), A1133.
- [93] Mikito Koshino and Intan Fatimah Hizbullah. “Magnetic susceptibility in three-dimensional nodal semimetals”. In: *Physical Review B* 93.4 (2016), p. 045201.
- [94] John M Kosterlitz and DJ Thouless. “Long range order and metastability in two dimensional solids and superfluids.(Application of dislocation theory)”. In: *Journal of Physics C: Solid State Physics* 5.11 (1972), p. L124.
- [95] John Michael Kosterlitz and David James Thouless. “Ordering, metastability and phase transitions in two-dimensional systems”. In: *Journal of Physics C: Solid State Physics* 6.7 (1973), p. 1181.
- [96] Gabriel Kotliar and Dieter Vollhardt. “Strongly correlated materials: Insights from dynamical mean-field theory”. In: *Physics today* 57.3 (2004), pp. 53–60.
- [97] Georg Kresse and Jürgen Furthmüller. “Efficiency of ab-initio total energy calculations for metals and semiconductors using a plane-wave basis set”. In: *Computational materials science* 6.1 (1996), pp. 15–50.

-
- [98] Georg Kresse and Jürgen Furthmüller. “Efficient iterative schemes for ab initio total-energy calculations using a plane-wave basis set”. In: *Physical review B* 54.16 (1996), p. 11169.
- [99] Georg Kresse and Jürgen Hafner. “Ab initio molecular dynamics for liquid metals”. In: *Physical review B* 47.1 (1993), p. 558.
- [100] Jürgen Kübler and Claudia Felser. “Berry curvature and the anomalous Hall effect in Heusler compounds”. In: *Physical Review B* 85.1 (2012), p. 012405.
- [101] Jürgen Kübler and Claudia Felser. “Non-collinear antiferromagnets and the anomalous Hall effect”. In: *EPL (Europhysics Letters)* 108.6 (2014), p. 67001.
- [102] Stefan Kurth, John P Perdew, and Peter Blaha. “Molecular and solid-state tests of density functional approximations: LSD, GGAs, and meta-GGAs”. In: *International journal of quantum chemistry* 75.4-5 (1999), pp. 889–909.
- [103] Wei-Li Lee et al. “Anomalous Hall Heat Current and Nernst Effect in the $CuCr_2Se_4$ Ferromagnet”. In: *Physical review letters* 93.22 (2004), p. 226601.
- [104] Henri R Leribaux. “Ferromagnetic Hall Effect with Electron-Phonon Interactions”. In: *Physical Review* 150.2 (1966), p. 384.
- [105] Mel Levy. “Electron densities in search of Hamiltonians”. In: *Physical Review A* 26.3 (1982), p. 1200.
- [106] Mel Levy. “Universal variational functionals of electron densities, first-order density matrices, and natural spin-orbitals and solution of the v -representability problem”. In: *Proceedings of the National Academy of Sciences* 76.12 (1979), pp. 6062–6065.
- [107] Xiaokang Li et al. “Anomalous Nernst and Righi-Leduc effects in Mn_3Sn : Berry curvature and entropy flow”. In: *Physical review letters* 119.5 (2017), p. 056601.
- [108] Yufan Li et al. “Robust formation of skyrmions and topological Hall effect anomaly in epitaxial thin films of $MnSi$ ”. In: *Physical review letters* 110.11 (2013), p. 117202.
- [109] Tian Liang et al. “Anomalous Hall effect in $ZrTe_5$ ”. In: *Nature Physics* 14.5 (2018), pp. 451–455.
- [110] Shuai Lin et al. “Good thermoelectric performance in strongly correlated system $SnCo_3$ with antiperovskite structure”. In: *Inorganic chemistry* 53.7 (2014), pp. 3709–3715.
- [111] *Linear response symmetry*. <https://bitbucket.org/zeleznyj/linear-response-symmetry/src/master/>.

-
-
- [112] Enke Liu et al. “Giant anomalous Hall effect in a ferromagnetic kagome-lattice semimetal”. In: *Nature physics* 14.11 (2018), pp. 1125–1131.
- [113] ZK Liu et al. “Discovery of a three-dimensional topological Dirac semimetal, Na₃Bi”. In: *Science* 343.6173 (2014), pp. 864–867.
- [114] F London. “Z phys chem b 1930, 11, 222; eisenschitz, r.; london, f”. In: *Z Phys* 60 (1930), p. 491.
- [115] MG Lopez et al. “Wannier-based calculation of the orbital magnetization in crystals”. In: *Physical Review B* 85.1 (2012), p. 014435.
- [116] Stephan Lowitzer, Diemo Koedderitzsch, and Hubert Ebert. “Coherent description of the intrinsic and extrinsic anomalous Hall effect in disordered alloys on an ab initio level”. In: *Physical review letters* 105.26 (2010), p. 266604.
- [117] BM Ludbrook, BJ Ruck, and S Granville. “Perpendicular magnetic anisotropy in Co₂MnGa and its anomalous Hall effect”. In: *Applied Physics Letters* 110.6 (2017), p. 062408.
- [118] Pavel Lukashev, Renat F Sabirianov, and Kirill Belashchenko. “Theory of the piezomagnetic effect in Mn-based antiperovskites”. In: *Physical Review B* 78.18 (2008), p. 184414.
- [119] Allan Hugh MacDonald and SH Vosko. “A relativistic density functional formalism”. In: *Journal of Physics C: Solid State Physics* 12.15 (1979), p. 2977.
- [120] Y Machida et al. “Unconventional anomalous Hall effect enhanced by a noncoplanar spin texture in the frustrated Kondo lattice Pr₂Ir₂O₇”. In: *Physical review letters* 98.5 (2007), p. 057203.
- [121] Arun Majumdar. “Thermoelectricity in semiconductor nanostructures”. In: *Science* 303.5659 (2004), pp. 777–778.
- [122] Kaustuv Manna et al. “From colossal to zero: controlling the anomalous Hall effect in magnetic Heusler compounds via Berry curvature design”. In: *Physical Review X* 8.4 (2018), p. 041045.
- [123] Anastasios Markou et al. “Hard magnet topological semimetals in XPt₃ compounds with the harmony of Berry curvature”. In: *Communications Physics* 4.1 (2021), pp. 1–7.
- [124] Richard M Martin. *Electronic structure: basic theory and practical methods*. Cambridge university press, 2020.

-
-
- [125] Nicola Marzari and David Vanderbilt. “Maximally localized generalized Wannier functions for composite energy bands”. In: *Physical review B* 56.20 (1997), p. 12847.
- [126] Nicola Marzari et al. “Maximally localized Wannier functions: Theory and applications”. In: *Reviews of Modern Physics* 84.4 (2012), p. 1419.
- [127] Andrew F May and Brian C Sales. “Twisting the thermoelectric potential”. In: *Nature Materials* 20.4 (2021), pp. 451–452.
- [128] Bharat Medasani et al. “Vacancy formation energies in metals: A comparison of MetaGGA with LDA and GGA exchange–correlation functionals”. In: *Computational Materials Science* 101 (2015), pp. 96–107.
- [129] N David Mermin. “Thermal properties of the inhomogeneous electron gas”. In: *Physical Review* 137.5A (1965), A1441.
- [130] T Miyasato et al. “Crossover behavior of the anomalous Hall effect and anomalous Nernst effect in itinerant ferromagnets”. In: *Physical review letters* 99.8 (2007), p. 086602.
- [131] Masaki Mizuguchi and Satoru Nakatsuji. “Energy-harvesting materials based on the anomalous Nernst effect”. In: *Science and technology of advanced materials* 20.1 (2019), pp. 262–275.
- [132] Roger SK Mong, Andrew M Essin, and Joel E Moore. “Antiferromagnetic topological insulators”. In: *Physical Review B* 81.24 (2010), p. 245209.
- [133] Arash A Mostofi et al. “wannier90: A tool for obtaining maximally-localised Wannier functions”. In: *Computer physics communications* 178.9 (2008), pp. 685–699.
- [134] Sebastian Muehlbauer et al. “Skyrmion lattice in a chiral magnet”. In: *Science* 323.5916 (2009), pp. 915–919.
- [135] Shuichi Murakami. “Phase transition between the quantum spin Hall and insulator phases in 3D: emergence of a topological gapless phase”. In: *New Journal of Physics* 9.9 (2007), p. 356.
- [136] Naoto Nagaosa et al. “Anomalous hall effect”. In: *Reviews of modern physics* 82.2 (2010), p. 1539.
- [137] Satoru Nakatsuji, Naoki Kiyohara, and Tomoya Higo. “Large anomalous Hall effect in a non-collinear antiferromagnet at room temperature”. In: *Nature* 527.7577 (2015), pp. 212–215.

-
-
- [138] Ajaya K Nayak et al. “Large anomalous Hall effect driven by a nonvanishing Berry curvature in the noncolinear antiferromagnet Mn₃Ge”. In: *Science advances* 2.4 (2016), e1501870.
- [139] Walther Nernst. “Ueber die electromotorischen Kräfte, welche durch den Magnetismus in von einem Wärmestrome durchflossenen Metallplatten geweckt werden”. In: *Annalen der Physik* 267.8 (1887), pp. 760–789.
- [140] A Neubauer et al. “Topological Hall effect in the A phase of MnSi”. In: *Physical review letters* 102.18 (2009), p. 186602.
- [141] Madhab Neupane et al. “Observation of a topological 3D Dirac semimetal phase in high-mobility Cd₃As₂”. In: *arXiv preprint arXiv:1309.7892* (2013).
- [142] Holger Bech Nielsen and Masao Ninomiya. “Absence of neutrinos on a lattice:(I). Proof by homotopy theory”. In: *Nuclear Physics B* 185.1 (1981), pp. 20–40.
- [143] Holger Bech Nielsen and Masao Ninomiya. “Absence of neutrinos on a lattice:(II). Intuitive topological proof”. In: *Nuclear Physics B* 193.1 (1981), pp. 173–194.
- [144] Holger Bech Nielsen and Masao Ninomiya. “The Adler-Bell-Jackiw anomaly and Weyl fermions in a crystal”. In: *Physics Letters B* 130.6 (1983), pp. 389–396.
- [145] Jonathan Noky et al. “Characterization of topological band structures away from the Fermi level by the anomalous Nernst effect”. In: *Physical Review B* 98.24 (2018), p. 241106.
- [146] Jonathan Noky et al. “Giant anomalous Hall and Nernst effect in magnetic cubic Heusler compounds”. In: *npj Computational Materials* 6.1 (2020), pp. 1–8.
- [147] Jonathan Noky et al. “Large anomalous Hall and Nernst effects from nodal line symmetry breaking in Fe₂MnX (X= P, As, Sb)”. In: *Physical Review B* 99.16 (2019), p. 165117.
- [148] Masaru Onoda and Naoto Nagaosa. “Topological nature of anomalous Hall effect in ferromagnets”. In: *Journal of the Physical Society of Japan* 71.1 (2002), pp. 19–22.
- [149] Mohamed Oudah et al. “Superconductivity in the antiperovskite Dirac-metal oxide Sr₃-xSnO”. In: *Nature communications* 7.1 (2016), pp. 1–6.
- [150] V Ozoliņš and M Körling. “Full-potential calculations using the generalized gradient approximation: Structural properties of transition metals”. In: *Physical Review B* 48.24 (1993), p. 18304.

-
-
- [151] LA Palomino-Rojas et al. “Density functional study of the structural properties of silver halides: LDA vs GGA calculations”. In: *Solid state sciences* 10.9 (2008), pp. 1228–1235.
- [152] Yu Pan et al. “Giant anomalous Nernst signal in the antiferromagnet YbMnBi₂”. In: *Nature materials* 21.2 (2022), pp. 203–209.
- [153] MM Pant and AK Rajagopal. “Theory of inhomogeneous magnetic electron gas”. In: *Solid State Communications* 10.12 (1972), pp. 1157–1160.
- [154] David C Patton and Mark R Pederson. “Application of the generalized-gradient approximation to rare-gas dimers”. In: *Physical Review A* 56.4 (1997), R2495.
- [155] David C Patton, Dirk V Porezag, and Mark R Pederson. “Simplified generalized-gradient approximation and anharmonicity: Benchmark calculations on molecules”. In: *Physical Review B* 55.12 (1997), p. 7454.
- [156] John P Perdew. “Accurate density functional for the energy: Real-space cutoff of the gradient expansion for the exchange hole”. In: *Physical Review Letters* 55.16 (1985), p. 1665.
- [157] John P Perdew, Kieron Burke, and Matthias Ernzerhof. “Generalized gradient approximation made simple”. In: *Physical review letters* 77.18 (1996), p. 3865.
- [158] John P Perdew, Andreas Savin, and Kieron Burke. “Escaping the symmetry dilemma through a pair-density interpretation of spin-density functional theory”. In: *Physical Review A* 51.6 (1995), p. 4531.
- [159] John P Perdew and Yue Wang. “Accurate and simple analytic representation of the electron-gas correlation energy”. In: *Physical review B* 45.23 (1992), p. 13244.
- [160] John P Perdew and Alex Zunger. “Self-interaction correction to density-functional approximations for many-electron systems”. In: *Physical Review B* 23.10 (1981), p. 5048.
- [161] John P Perdew et al. “Atoms, molecules, solids, and surfaces: Applications of the generalized gradient approximation for exchange and correlation”. In: *Physical review B* 46.11 (1992), p. 6671.
- [162] PHT Philipsen and EJ Baerends. “Cohesive energy of 3d transition metals: density functional theory atomic and bulk calculations”. In: *Physical Review B* 54.8 (1996), p. 5326.
- [163] Giovanni Pizzi et al. “Wannier90 as a community code: new features and applications”. In: *Journal of Physics: Condensed Matter* 32.16 (2020), p. 165902. DOI: 10.1088/1361-648x/ab51ff.

-
-
- [164] AK Rajagopal. “Inhomogeneous relativistic electron gas”. In: *Journal of Physics C: Solid State Physics* 11.24 (1978), p. L943.
- [165] AK Rajagopal and J Callaway. “Inhomogeneous electron gas”. In: *Physical Review B* 7.5 (1973), p. 1912.
- [166] R Ramos et al. “Anomalous Nernst effect of Fe₃O₄ single crystal”. In: *Physical Review B* 90.5 (2014), p. 054422.
- [167] Mark Rasolt and G Vignale. “Self-induced effective gauge fields in the copper-oxygen plane of high-T_c perovskites: A lattice and a continuum formulation”. In: *Physical review letters* 65.12 (1990), p. 1498.
- [168] Helena Reichlova et al. “Large anomalous Nernst effect in thin films of the Weyl semimetal Co₂MnGa”. In: *Applied Physics Letters* 113.21 (2018), p. 212405.
- [169] Erich Runge and Eberhard KU Gross. “Density-functional theory for time-dependent systems”. In: *Physical review letters* 52.12 (1984), p. 997.
- [170] Philip Peter Rushton. “Towards a non-local density functiona description of exchange and correlation”. PhD thesis. Durham University, 2002.
- [171] Akito Sakai et al. “Giant anomalous Nernst effect and quantum-critical scaling in a ferromagnetic semimetal”. In: *Nature Physics* 14.11 (2018), pp. 1119–1124.
- [172] Akito Sakai et al. “Iron-based binary ferromagnets for transverse thermoelectric conversion”. In: *Nature* 581.7806 (2020), pp. 53–57.
- [173] Yuya Sakuraba. “Potential of thermoelectric power generation using anomalous Nernst effect in magnetic materials”. In: *Scripta Materialia* 111 (2016), pp. 29–32.
- [174] Yuya Sakuraba et al. “Anomalous Nernst effect in L10-FePt/MnGa thermopiles for new thermoelectric applications”. In: *Applied Physics Express* 6.3 (2013), p. 033003.
- [175] Ilias Samathrakakis and Hongbin Zhang. “Tailoring the anomalous Hall effect in the noncollinear antiperovskite Mn₃GaN”. In: *Physical Review B* 101.21 (2020), p. 214423.
- [176] Ilias Samathrakakis et al. “Enhanced anomalous Nernst effects in ferromagnetic materials driven by Weyl nodes”. In: *Journal of Physics D: Applied Physics* 55.7 (2021), p. 074003.
- [177] Ilias Samathrakakis et al. “Thermodynamical and topological properties of metastable Fe₃Sn”. In: *arXiv preprint arXiv:2203.01172* (2022).
- [178] Ilias Samathrakakis et al. “Tunable anomalous Hall and Nernst effects in MM’X compounds”. In: *arXiv preprint arXiv:2207.03320* (2022).

-
-
- [179] Takafumi Sato et al. “Observation of band crossings protected by nonsymmorphic symmetry in the layered ternary telluride Ta₃SiTe₆”. In: *Physical Review B* 98.12 (2018), p. 121111.
- [180] Marten Seemann et al. “Symmetry-imposed shape of linear response tensors”. In: *Physical Review B* 92.15 (2015), p. 155138.
- [181] Kewen Shi et al. “Baromagnetic effect in antiperovskite Mn₃Ga_{0.95}N_{0.94} by neutron powder diffraction analysis”. In: *Advanced Materials* 28.19 (2016), pp. 3761–3767.
- [182] T Shibayama and K Takenaka. “Giant magnetostriction in antiperovskite Mn₃CuN”. In: *Journal of applied physics* 109.7 (2011), 07A928.
- [183] David Sholl and Janice A Steckel. *Density functional theory: a practical introduction*. John Wiley & Sons, 2011.
- [184] Harish K Singh et al. “Giant anomalous Hall and anomalous Nernst conductivities in antiperovskites and their tunability via magnetic fields”. In: *Physical Review Materials* 6.4 (2022), p. 045402.
- [185] Harish K Singh et al. “High-throughput screening of magnetic antiperovskites”. In: *Chemistry of Materials* 30.20 (2018), pp. 6983–6991.
- [186] Harish K Singh et al. “Multifunctional antiperovskites driven by strong magnetostructural coupling”. In: *npj Computational Materials* 7.1 (2021), pp. 1–9.
- [187] Marlina Slamet and Virah Sahni. “The gradient expansion approximation for exchange: A physical perspective”. In: *International Journal of Quantum Chemistry* 44.S26 (1992), pp. 333–345.
- [188] John Clarke Slater. “The self consistent field and the structure of atoms”. In: *Physical Review* 32.3 (1928), p. 339.
- [189] Libor Šmejkal et al. “Crystal time-reversal symmetry breaking and spontaneous Hall effect in collinear antiferromagnets”. In: *Science advances* 6.23 (2020), eaaz8809.
- [190] Jan Smit. “The spontaneous Hall effect in ferromagnetics II”. In: *Physica* 24.1-5 (1958), pp. 39–51.
- [191] Alexey A Soluyanov et al. “Type-ii weyl semimetals”. In: *Nature* 527.7579 (2015), pp. 495–498.
- [192] Zhida Song, Zhong Fang, and Chen Fang. “(d- 2)-dimensional edge states of rotation symmetry protected topological states”. In: *Physical review letters* 119.24 (2017), p. 246402.

-
-
- [193] Ivo Souza, Nicola Marzari, and David Vanderbilt. “Maximally localized Wannier functions for entangled energy bands”. In: *Physical Review B* 65.3 (2001), p. 035109.
- [194] PA Sterne and JC Inkson. “Exchange-correlation potential in semiconductors and insulators”. In: *Journal of Physics C: Solid State Physics* 17.9 (1984), p. 1497.
- [195] Nakheon H Sung et al. “Magnetic phase dependence of the anomalous Hall effect in Mn₃Sn single crystals”. In: *Applied Physics Letters* 112.13 (2018), p. 132406.
- [196] Christoph Sürgers. “Electrical switching of the anomalous Hall effect”. In: *Nature Electronics* 1.3 (2018), pp. 154–155.
- [197] Christoph Sürgers et al. “Switching of a large anomalous Hall effect between metamagnetic phases of a non-collinear antiferromagnet”. In: *Scientific reports* 7.1 (2017), pp. 1–7.
- [198] M-T Suzuki et al. “Cluster multipole theory for anomalous Hall effect in antiferromagnets”. In: *Physical Review B* 95.9 (2017), p. 094406.
- [199] H Svensmark and P Dimon. “Experimental observation of Berry’s phase of the Lorentz group”. In: *Physical review letters* 73.25 (1994), p. 3387.
- [200] Y Taguchi et al. “Spin chirality, Berry phase, and anomalous Hall effect in a frustrated ferromagnet”. In: *Science* 291.5513 (2001), pp. 2573–2576.
- [201] T Takeda. “The scalar relativistic approximation”. In: *Zeitschrift für Physik B Condensed Matter* 32.1 (1978), pp. 43–48.
- [202] K Takenaka and H Takagi. “Giant negative thermal expansion in Ge-doped antiperovskite manganese nitrides”. In: *Applied Physics Letters* 87.26 (2005), p. 261902.
- [203] Gerhard Theurich and Nicola A Hill. “Self-consistent treatment of spin-orbit coupling in solids using relativistic fully separable ab initio pseudopotentials”. In: *Physical Review B* 64.7 (2001), p. 073106.
- [204] Llewellyn H Thomas. “The calculation of atomic fields”. In: *Mathematical proceedings of the Cambridge philosophical society*. Vol. 23. 5. Cambridge University Press. 1927, pp. 542–548.
- [205] David J Thouless et al. “Quantized Hall conductance in a two-dimensional periodic potential”. In: *Physical review letters* 49.6 (1982), p. 405.
- [206] Peng Tong, Bo-Sen Wang, and Yu-Ping Sun. “Mn-based antiperovskite functional materials: Review of research”. In: *Chinese Physics B* 22.6 (2013), p. 067501.

-
-
- [207] Stepan S Tsirkin. “High performance Wannier interpolation of Berry curvature and related quantities with WannierBerri code”. In: *npj Computational Materials* 7.1 (2021), pp. 1–9.
- [208] Daniel C Tsui, Horst L Stormer, and Arthur C Gossard. “Two-dimensional magnetotransport in the extreme quantum limit”. In: *Physical Review Letters* 48.22 (1982), p. 1559.
- [209] Sennoga Twaha et al. “A comprehensive review of thermoelectric technology: Materials, applications, modelling and performance improvement”. In: *Renewable and sustainable energy reviews* 65 (2016), pp. 698–726.
- [210] Ken-ichi Uchida, Weinan Zhou, and Yuya Sakuraba. “Transverse thermoelectric generation using magnetic materials”. In: *Applied Physics Letters* 118.14 (2021), p. 140504.
- [211] Masafumi Udagawa and Roderich Moessner. “Anomalous Hall effect from frustration-tuned scalar chirality distribution in $\text{Pr}_2\text{Ir}_2\text{O}_7$ ”. In: *Physical review letters* 111.3 (2013), p. 036602.
- [212] G Vignale and Mark Rasolt. “Current-and spin-density-functional theory for inhomogeneous electronic systems in strong magnetic fields”. In: *Physical Review B* 37.18 (1988), p. 10685.
- [213] G Vignale and Mark Rasolt. “Density-functional theory in strong magnetic fields”. In: *Physical review letters* 59.20 (1987), p. 2360.
- [214] G Vignale, Mark Rasolt, and DJW Geldart. “Magnetic fields and density functional theory”. In: *Advances in quantum chemistry*. Vol. 21. Elsevier, 1990, pp. 235–253.
- [215] Valerio Vitale et al. “Automated high-throughput Wannierisation”. In: *npj Computational Materials* 6.1 (2020), pp. 1–18.
- [216] Ulf Von Barth and Lars Hedin. “A local exchange-correlation potential for the spin polarized case. i”. In: *Journal of Physics C: Solid State Physics* 5.13 (1972), p. 1629.
- [217] Seymour H Vosko, Leslie Wilk, and Marwan Nusair. “Accurate spin-dependent electron liquid correlation energies for local spin density calculations: a critical analysis”. In: *Canadian Journal of physics* 58.8 (1980), pp. 1200–1211.
- [218] Xiangang Wan et al. “Topological semimetal and Fermi-arc surface states in the electronic structure of pyrochlore iridates”. In: *Physical Review B* 83.20 (2011), p. 205101.

-
-
- [219] Xinjie Wang et al. “Ab initio calculation of the anomalous Hall conductivity by Wannier interpolation”. In: *Physical Review B* 74.19 (2006), p. 195118.
- [220] Xinjie Wang et al. “Fermi-surface calculation of the anomalous Hall conductivity”. In: *Physical Review B* 76.19 (2007), p. 195109.
- [221] Zhijun Wang et al. “Dirac semimetal and topological phase transitions in A₃Bi (A = Na, K, Rb)”. In: *Physical Review B* 85.19 (2012), p. 195320.
- [222] Zhijun Wang et al. “Three-dimensional Dirac semimetal and quantum transport in Cd₃As₂”. In: *Physical Review B* 88.12 (2013), p. 125427.
- [223] Gregory H Wannier. “The structure of electronic excitation levels in insulating crystals”. In: *Physical Review* 52.3 (1937), p. 191.
- [224] Jürgen Weischenberg et al. “Scattering-independent anomalous Nernst effect in ferromagnets”. In: *Physical Review B* 87.6 (2013), p. 060406.
- [225] B Wiendlocha et al. “Electronic structure, superconductivity and magnetism study of Cr₃GaN and Cr₃RhN”. In: *Journal of alloys and compounds* 442.1-2 (2007), pp. 289–291.
- [226] QuanSheng Wu et al. “WannierTools: An open-source software package for novel topological materials”. In: *Computer Physics Communications* 224 (2018), pp. 405–416.
- [227] Di Xiao, Ming-Che Chang, and Qian Niu. “Berry phase effects on electronic properties”. In: *Reviews of modern physics* 82.3 (2010), p. 1959.
- [228] Di Xiao et al. “Berry-phase effect in anomalous thermoelectric transport”. In: *Physical review letters* 97.2 (2006), p. 026603.
- [229] Lilia S Xie et al. “A new form of Ca₃P₂ with a ring of Dirac nodes”. In: *Apl Materials* 3.8 (2015), p. 083602.
- [230] Yuanfeng Xu et al. “High-throughput calculations of magnetic topological materials”. In: *Nature* 586.7831 (2020), pp. 702–707.
- [231] Ai Yamakage et al. “Line-node Dirac semimetal and topological insulating phase in noncentrosymmetric pnictides CaAgX (X = P, As)”. In: *Journal of the Physical Society of Japan* 85.1 (2016), p. 013708.
- [232] Shuai Yang et al. “Unconventional temperature dependence of the anomalous Hall effect in HgCr₂Se₄”. In: *Physical Review Letters* 123.9 (2019), p. 096601.
- [233] Shuo-Ying Yang et al. “Giant, unconventional anomalous Hall effect in the metallic frustrated magnet candidate, KV₃Sb₅”. In: *Science advances* 6.31 (2020), eabb6003.

-
-
- [234] Zihao Yang et al. “Scalable Nernst thermoelectric power using a coiled galphenol wire”. In: *AIP Advances* 7.9 (2017), p. 095017.
- [235] Yugui Yao et al. “First principles calculation of anomalous Hall conductivity in ferromagnetic bcc Fe”. In: *Physical review letters* 92.3 (2004), p. 037204.
- [236] Rui Yu et al. “Topological node-line semimetal and Dirac semimetal state in antiperovskite Cu₃PdN”. In: *Physical review letters* 115.3 (2015), p. 036807.
- [237] XZ Yu et al. “Near room-temperature formation of a skyrmion crystal in thin-films of the helimagnet FeGe”. In: *Nature materials* 10.2 (2011), pp. 106–109.
- [238] Jakub Železný et al. “High-throughput study of the anomalous Hall effect”. In: *arXiv preprint arXiv:2205.14907* (2022).
- [239] J Zemen, Z Gercsi, and KG Sandeman. “Piezomagnetism as a counterpart of the magnetovolume effect in magnetically frustrated Mn-based antiperovskite nitrides”. In: *Physical Review B* 96.2 (2017), p. 024451.
- [240] J Zemen et al. “Frustrated magnetism and caloric effects in Mn-based antiperovskite nitrides: Ab initio theory”. In: *Physical Review B* 95.18 (2017), p. 184438.
- [241] Ding Zhang, Yuanhao Wang, and Ya Yang. “Design, performance, and application of thermoelectric nanogenerators”. In: *Small* 15.32 (2019), p. 1805241.
- [242] Yang Zhang et al. “Strong anisotropic anomalous Hall effect and spin Hall effect in the chiral antiferromagnetic compounds Mn₃X (X= Ge, Sn, Ga, Ir, Rh, and Pt)”. In: *Physical Review B* 95.7 (2017), p. 075128.
- [243] Yingkai Zhang, Wei Pan, and Weitao Yang. “Describing van der Waals Interaction in diatomic molecules with generalized gradient approximations: The role of the exchange functional”. In: *The Journal of chemical physics* 107.19 (1997), pp. 7921–7925.
- [244] Zeying Zhang et al. “High-throughput screening and automated processing toward novel topological insulators”. In: *The journal of physical chemistry letters* 9.21 (2018), pp. 6224–6231.
- [245] Yusheng Zhao and Luke L Daemen. “Superionic conductivity in lithium-rich anti-perovskites”. In: *Journal of the American Chemical Society* 134.36 (2012), pp. 15042–15047.
- [246] Weinan Zhou and Yuya Sakuraba. “Heat flux sensing by anomalous Nernst effect in Fe–Al thin films on a flexible substrate”. In: *Applied Physics Express* 13.4 (2020), p. 043001.

-
-
- [247] Weinan Zhou et al. “Seebeck-driven transverse thermoelectric generation”. In: *Nature Materials* 20.4 (2021), pp. 463–467.
- [248] Xiaodong Zhou et al. “Giant anomalous Nernst effect in noncollinear antiferromagnetic Mn-based antiperovskite nitrides”. In: *Physical review materials* 4.2 (2020), p. 024408.
- [249] Xiaodong Zhou et al. “Spin-order dependent anomalous Hall effect and magneto-optical effect in the noncollinear antiferromagnets Mn_3XN with $x = Ga, Zn, Ag,$ or Ni ”. In: *Physical Review B* 99.10 (2019), p. 104428.
- [250] Paul Ziesche, Stefan Kurth, and John P Perdew. “Density functionals from LDA to GGA”. In: *Computational materials science* 11.2 (1998), pp. 122–127.
- [251] AA Zyuzin, Si Wu, and AA Burkov. “Weyl semimetal with broken time reversal and inversion symmetries”. In: *Physical Review B* 85.16 (2012), p. 165110.